Reconfigurable Kirigami Optics and Chiral Phonons

by

Wonjin Choi

A dissertation submitted in partial fulfillment
of the requirements for the degree of
Doctor of Philosophy
(Materials Science and Engineering)
in the University of Michigan
2021

Doctoral Committee:

Professor Nicholas A. Kotov, Chair
Professor Jay Guo
Professor Jinsang Kim
Professor Joerg Lahann

Wonjin Choi

wonjchoi@umich.edu

ORCID iD: 0000-0001-6303-8899

Dedication

To my family

Acknowledgements

I would like to express my sincere appreciations to my advisor, Professor Nicholas A. Kotov. I can still remember the first moment when I decided to enroll the University of Michigan for PhD. Since I knew how advisor is important for one's PhD, research career and entire life, I deeply pondered where to go and decided to enroll in University of Michigan in the end because there is a Prof. Kotov. Thankfully, after about six years of journey with him, I can say that I was right. He always inspires and encourages students to find something different posing important questions such as "How your discovery or research could make world different in a good way". He is a true scientist having an eye for beauty of nature understanding the multifaced roles of hierarchical structures and complex systems. I was honored to work with him and be able to learn his way of thinking. Every research that I worked with him was unique and extraordinary. Other than just research, he is a good life teacher who is thoughtful and willing to level with me.

I would also like to extend thanks to my committee, Prof. Jinsang Kim, Prof. Joerg Lahann, and Prof. Jay Guo. I have been fortunate to learn from each of my committee members, whether this was through research collaborations, discussions or direct comments on my dissertation. Thank you for broadening my horizons. Special thanks to Prof. Kim, whenever I had a hard time, he was always willing to help me with thoughtful comments. Although I couldn't have many opportunities to have a conversation but the fact that he is very close to where I am and I could ask help whenever I want gave me relief and strength.

Thank you for Kotov lab members. I would be proud once I was the member of this prestigious research group. To Yoonseob Kim, Joonghwan Bahng, Jihyeon Yeom, Ji-young Kim, Terry Shyu, Yichun Wang, Lizhi Xu, Zhibei Qu, Keiichi Yano, Jun Lu, Douglas Montjoy, Minjeong Cha, Prashant Kumar, Naomi Ramesar, Ahmet Emre, Sumeyra Emre, Drew Vecchio, Prashant Kumar, Anastasiia Visheratina, Drew Vecchio, Connor Mcglothin, Elizabeth Wilson, Yuan Cao, Mische Hubbard, Sang Hyun Lee, Yuan Cao, Chug-Man Lim, Ming Lei, Yu-Huan Luan and Ryan Branch, thank you, lab members. I learned a lot from you and really appreciate for making everything so smooth and good environment to do research helping each other.

I was blessed to have a great team of creative collaborators working with me. Thank you to Prof. Theodore Norris, your comments always made complex problems simpler and clearer, it was always great help for solving the scientific problems. To Gong Chen, Zhengyu Huang, Yifan Shen, John Soukar, I really appreciate it for your advices and comments on kirigami work, THz spectroscopy, FTIR experiments, simulations and bacteria work. I really appreciate my collaborators in Brazil, Prof. A. F. Moura and Dr. Colombari. Without your help I could not have done analysis of molecular vibrations. Special thanks to Prof. John Kruger in Michigan State University for allowing me to have amazing experience by providing real clinical samples.

The friendships I developed outside the lab made my life all the worthwhile. To Jihang Lee, Eongyu Yi, Eunseong Moon, Seungwoo Lee, Dowon Ahn, Deokwon Seo, Min Sang Kwon, Jongho Kim, Do Hyun Kang, Joonkoo Kang, Taesu Kim, Insung Han, Sunghoon Hur, Ben Derby, Dandan Wang, Ruiming Lu, Kelsey Mengle, Max Powers, Suk Hyun Sung, Michael Deininger, Ben Derby, Kuan-Hung Chen, Juwon Lim, Sieun Chae, Sung Hyun Nam, Youngwoo Woo, Daseul Yang, Junsoo Kim, John Kim and Chris Kim, thank you for being my friend and having my back. I will always want to have a cup of coffee with you.

The families I met here in Ann Arbor made my life more fruitful, meaningful and happy. To Junghoon Kim, Minhwa Kim (Jang), Sunmin Jang, Seunghyun Kim, Changwon Choi, Hyeyeong Cha, Chang Hyun Yoon, Hyesue Jang, Jason Lee, Seungmi Moon, Jeongsup Lee, Geumju Song, Jaehyun Jung, Miri Kim, Woongky Son, Soonyoung Lee, Youngchan Jang, Hyonjung Kim, Jiseok Gim, Anna Son, Seung Hwan Lee, Hyunjung Lee, Inwoong Hwang, Seungyeon Son, Dukkyun Yoon, Hanna Seol, Shinhyun Choi, Hae Ryung Park, Sung Yoon Jung, Suhui Yang, Hanpyo Lee, Minhwa Kim, Jongeun You, Hyun-hee Cho, Jiwon Lim, Jihye Ju, Seong-Eun Kwak, Eunju Lee, it was glad to have delicious food and be happy moments together. I realized that the time we spent together helping and sharing each other is the pure gold of our life. Special thanks to Irene Park and her family and Diane Kim and her family for being a friend of my daughters and next-door neighbor of us.

Finally, I would like to express my deepest gratitude to my beloved family. I specially thank to my parents, Seonghak Choi and Yesuk Yoon for supporting and encouraging me to grow as a scientist and father showing what is unlimited and unconditional love. After becoming a parent, I realized a little bit more about how you are loving and caring me. Thank my wife, Hanjin Lim. Without her love I could have not gotten through this winding journey. I thank my two daughters, Yoona Choi and Yoonseo Choi for their great joy that they have brought to our family since they were born.

I realized that every aspect of life is important. Thank you for taking care of each important part of my life. I really appreciate that because each part of life can also be seen as the whole. I am a truly happy person to have you all.

Table of Contents

List of Tables

List of Figures

Abstract

All atoms and chemical bonds vibrate at natural frequencies associated with their physical properties. Scientists therefore use resonance-based spectroscopy to investigate the structural characteristics and dynamics of molecules in several research areas. However, it has been arduous to observe and identify complex vibrational modes of biomolecules and tissues with excitations in the terahertz (THz) range (*1*). In this work, we report on the development of THz circular dichroism spectroscopy enabled by kirigami polarization modulator and their applications for probing mesoscale chiral architectures and vibrations from the (bio) materials (*1*). Also, we show that hyperspectral THz chiroptical spectroscopy enables registration and attribution of chiral phonons in microcrystals of numerous amino acids and dipeptides (*2*).

Terahertz circular dichroism (TCD) offers multifaceted spectroscopic capabilities for understanding of biomaterials, biomolecules, and pharmaceuticals because the energy of THz photons enables probing the 'soft' oscillatory vibrations of biomolecules with distinct chirality (*1*). However, the lack of dynamic polarization modulators is impeding the proliferation of TCD spectroscopy (*1*). In the Chapter 3 of this dissertation, we show that tunable optical elements fabricated from patterned plasmonic sheets with periodic kirigami cuts make possible polarization modulation of THz radiation under application of mechanical strain (*1*). A herringbone pattern of microscale metal stripes enables dynamic range of polarization modulation exceeding 80 degree

repeatable over thousands of cycles (*1*). Upon out-of-plane buckling, the plasmonic stripes function as reconfigurable semi-helices of variable pitch aligned along the THz propagation direction (*1*). Several biomaterials, exemplified by elytra of *Chrysina gloriosa* beetles, revealed distinct TCD fingerprints associated with the helical substructure in the bio-composites (*1*).

Chiral phonons, complex lattice vibrations modes with mirror asymmetry, have been known only for a small number of low-dimensional inorganic nanostructures (*2*). Abundant chiral phonon modes can also be expected for crystals of many biomolecules but experimental and theoretical toolbox on their observation and identification is unknown (*2*). Besides much larger variety of vibrational modes, chiral phonons in biological crystals can also be medically relevant (*2*). In the Chapter 4 of the dissertation, we show that terahertz absorption (TA), circular dichroism (TCD), and optical rotation dispersion (TORD) provide effective tools for the registration and identification of chiral phonons in micro-crystals of 20 proteinogenic *L*- and *D*-amino acids (AAs) (*2*). Theoretical predictions and molecular dynamics simulations of chiral phonon in AA crystals provided direct evidence for the molecular origins of TCD and TORD spectra, which are dominated by collective motions of AA molecules (*2*). Generality of these findings can be highlighted by the observation of chiral phonons in crystals of dipeptides cystine and carnosine, which also demonstrates direct relevance of chiral phonons for medical and pharmaceutical applications (*2*).

Chapter 1. Introduction

"If you want to find the secrets of the universe, think in terms of energy, frequency and vibration."

-Nikola Tesla

1.1 Motivation: Vibrations

Every object in our universe from electrons, atoms to planets are persistently in motion, they are vibrating (*3*). Even objects that seem to be still are in fact vibrating, rotating, oscillating and resonating at various frequencies (*3*). According to the book of brief history of mathematics (*4*), people became interested in this vibrational phenomena when they created and played the musical instruments (*5*). The Greek philosopher and mathematician Pythagoras (582 - 507 B.C.) is considered to be the first inventor to investigate and engineer acoustic wave on a scientific basis (**Figure 1-1**) (*4, 5*). Since then people including musicians, scientists and philosophers have discovered and developed the laws and mathematical equations of wave and passed them on from generation to generation (*5*). Now, we can find this vibrational phenomena in many branches of other science and even in very different scales. We know that light, the electromagnetic wave consists of oscillating electric and magnetic field as it propagates. Also, when we think about the space, there are a lot of oscillating moving parts to the Universe. Another very complex but vibrating in different scale of the system is vibrations at the quantum mechanical level. Electron

clouds are oscillating by electromagnetic field and molecules in the free space are vibrating mainly due to the thermal excitations. These systems are particularly important, especially for physics, chemistry and materials science because vibrational states of electrons, atoms, molecules are strongly related to the physical and chemical properties of matter.

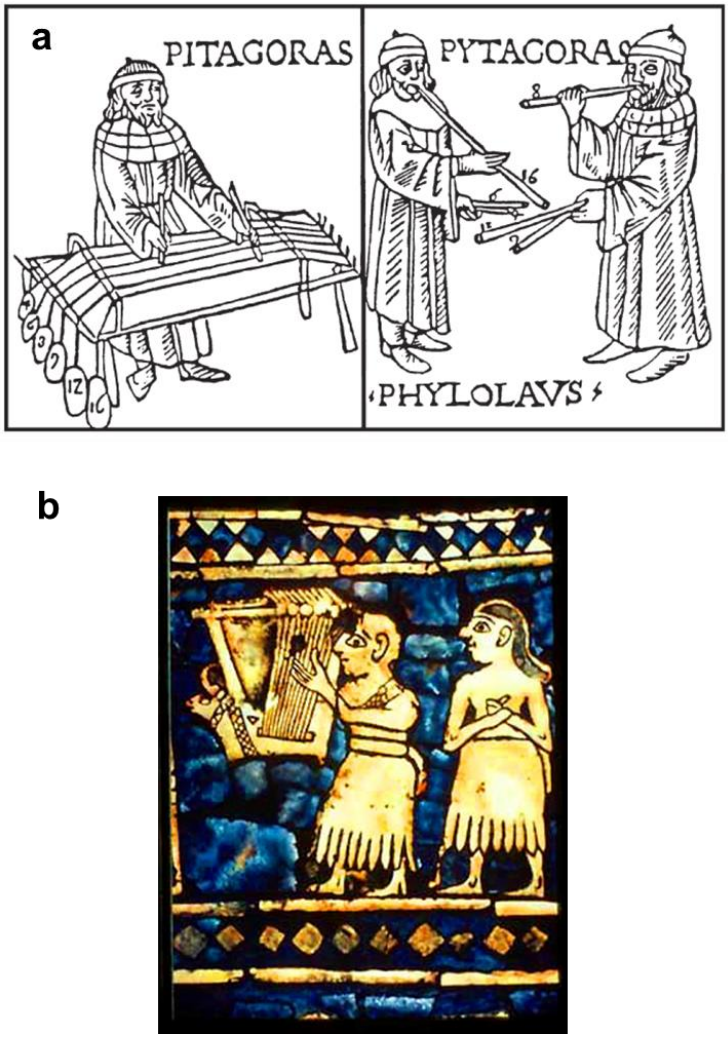

Figure 1-1. (a) Pythagoras as a musician. Reproduced from ref.(*6*). (b) Detail of the "Peace" panel of the Standard of Ur showing lyrist, excavated from the same site as the Lyres of Ur, the second oldest string instrument. Reproduced from ref. (*7*).

1.2 Motivation: Resonance

Where there are vibrations, there are resonance. The resonance is the universal phenomenon describing of increased magnitude that occurs when the frequency of an applied energy is close to a natural frequency of the system on which it acts (**Figure 1-2**) (*8*). Here, natural frequency, also known as eigenfrequency, is the frequency at which a system tends to oscillate in the absence of any external forces (*9*).

By utilizing the resonance, we could measure the position of natural frequency and amplitude of the vibration. To describe and understand underlying principles of various vibrational phenomena, scientists often adopt simplified harmonic oscillation model which consists of mass, spring and damper. Many analogical analyses have been made; for example, Lorentz oscillation model assumes an electron as a mass and electrostatic coulombic force as a spring since they behave similarly according to Hooke's law. Equations of harmonic oscillation could also be applied to resonant circuits. In RLC (resistor, inductor and capacitor) circuit model, each electrical components can be compared to mass, spring and damper. Not only for those, in quantum mechanics, the spring model is used to calculate parabolic potential energy curve where it gives a quantized energy level.

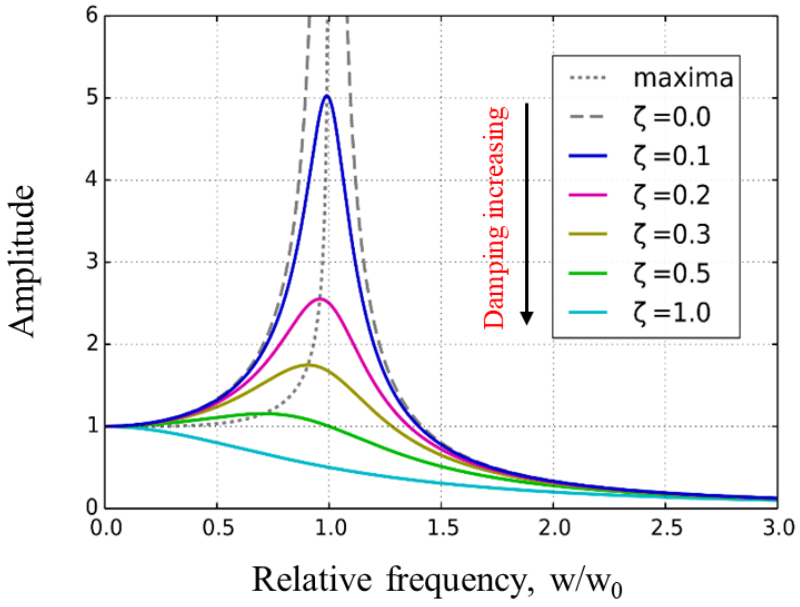

Figure 1-2. Steady-state variation of amplitude with relative frequency and damping of a driven simple harmonic oscillator. Reproduced from ref. (*8*).

1.3 Infrared Spectroscopy – Brief history

One of the greatest inventions exploiting this resonance phenomena is the infrared (IR) spectroscopy which I believe a most powerful tool for the investigation of the structure of molecules. Historically, infrared rays are considered to be found by Wilhelm Herschel who performed the study of spectra using a bulb of a sensitive thermometer in 1800 (*10*). In his paper, he found that maximum of heat in the distribution curves is located beyond the red end of the spectrum (**Figure 1-3a**) (*10*). After figuring out these invisible infrared, or "heat," rays, he studied the transmissions of various materials and found that some materials are opaque to visible light and at the same time transparent to the infrared rays (*10*). Many great scientists including Young,

Wollaston, Fraunhofer, Brewster, J. F. W. Herschel, the son of the Wilhelm, Talbot, and Kirchhoff have thoroughly studied to interpretate the so-called Fraunhofer lines, and found the possibility of identifying chemical structures by registering the spectrum (*10*). They are considered as the founder of spectroscopy. Picture of the sun's spectrum produced by J. F. W. Herschel in 1840 using the soot coated paper clearly shows the most intense heating are occurred in the infrared region (**Figure 1-3b**) (*10*). Using the fact that the alcohol evaporated fastest where the energy of radiation was high and absorbed by the soot, leaving the fingerprinting spots, he found that the absorption of the radiation by atmosphere was attributed to these Fraunhofer lines (*10*).

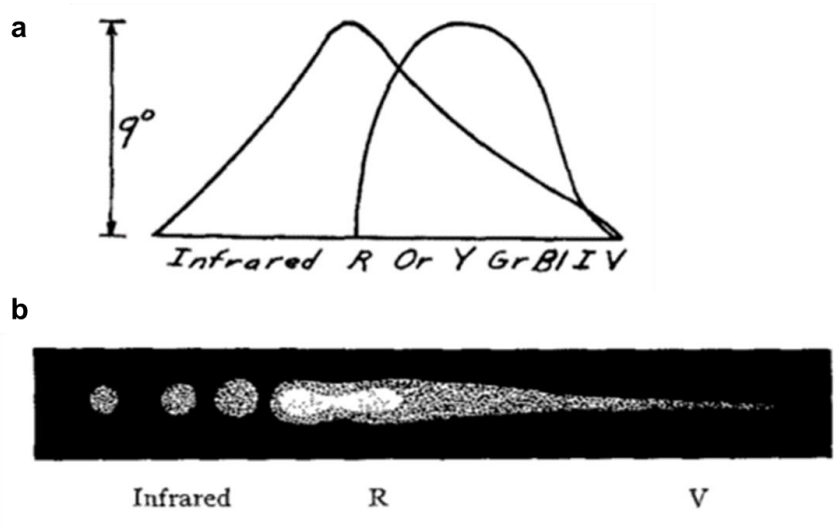

Figure 1-3. (a) Herschel Wilhelm's comparison of the distribution of light and heat in the sun's spectrum. The vertical scale of the latter curve is chosen to make the two maximums the same height. (b) J. F. W. Herschel's picture of the sun's spectrum, produced by the differential evaporation of alcohol from a soot layer. Reproduced from ref. (*10*) with the permission of the American Association of Physics Teachers.

1.4 Infrared Spectroscopy – Light-Matter Interaction

To understand how infrared rays are absorbed by atmosphere, chemicals or matter, we should comprehend the concept of light-matter interaction. When electromagnetic radiation including infrared rays strikes on an object, absorption, reflection, emission, and transmission occurs. When a photon, a quantized light particle, hits the atom, the energy is absorbed. If the energy of photon is larger than the energy differences between high and low energy states of the atom, then the atom could be excited and various phenomena such as absorption, fluorescence and phosphorescence occur (*11*). Different ways of photon and electron interactions are explained by the Jablonski diagram **Figure 1-4** (*11*). Among the three relaxation processes, the vibrational relaxation occurs between vibrational states and it happens usually in a few picoseconds. IR spectroscopy is a prevalent method for studying molecular vibrations and dipole moment. Since the resonance frequency is strongly depend on the chemical structure of the sample, molecules can be detected in the IR spectrum typically between the range of 12,800 and 200 cm^{-1}(*11*). Active vibrational and rotational eigen modes can be calculated theoretically **Figure 1-5** (*11*).

Fourier transform infrared spectroscopy (FTIR) has been widely used in the analytical chemistry field. Based on the interferometers, FTIR have two principal advantages; high energy through-put and multiplexing (*12*). Representative Michelson interferometer normally consists of two mirrors; one fixed and the other one movable and a beam splitters (**Figure 1-6**). In general, the energy throughput of FTIR is greater than for a dispersion instrument (*12*). FTIR holds many applications including identification of samples, quality control and quantitative infrared analysis. An overview of the utility is summarized in **Figure 1-7** (*12*).

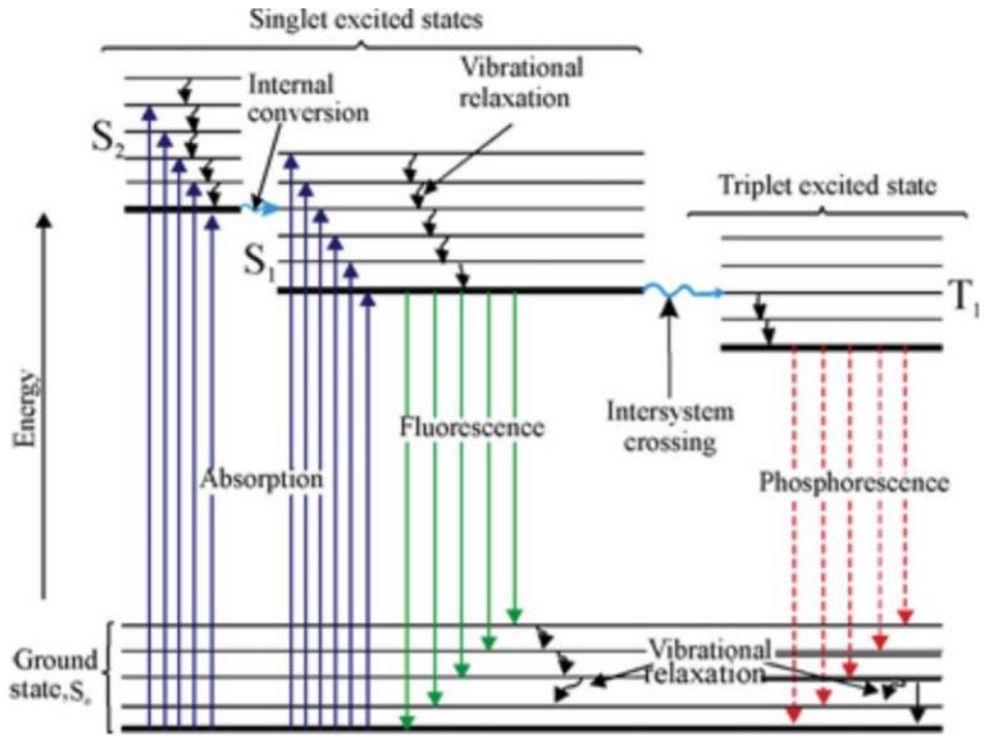

Figure 1-4. Jablonski diagram. Reproduced from (*11*).

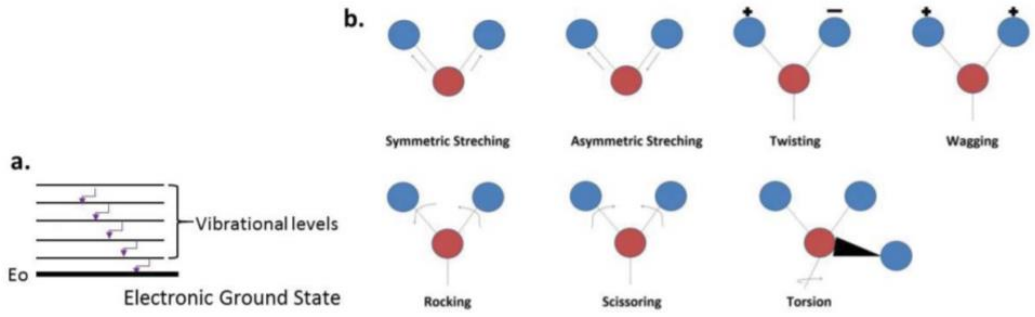

Figure 1-5. (a) IR Spectroscopy transitions on the Jablonski diagram. (b) Vibrational modes. Reproduced from (*11*).

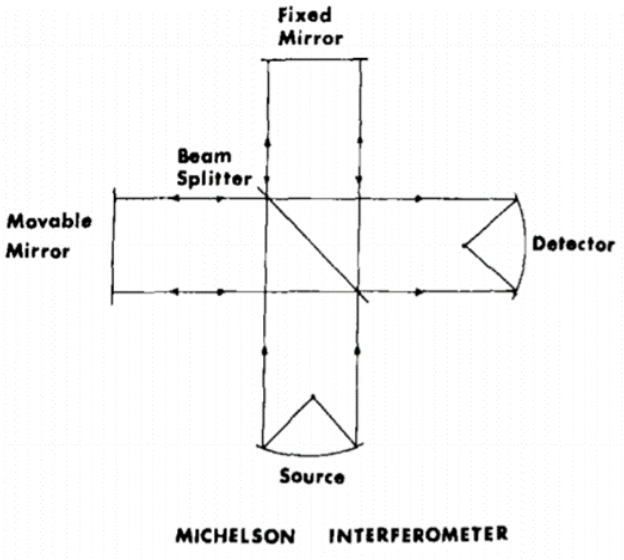

Figure 1-6. Diagram of Michelson interferometer. Reproduced from (*12*).

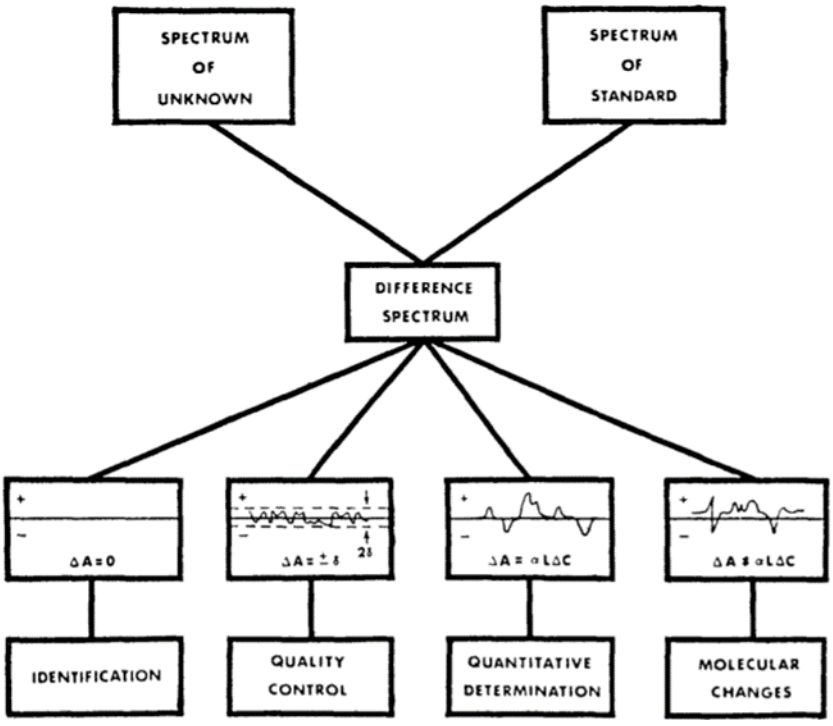

Figure 1-7 Applications of FTIR spectroscopy. Reproduced from (*12*).

Figure 1-8 is an example of IR spectrum from polyethylene films showing several absorbance bands (*12*). We can assign those bands to the exact vibrational modes because we can theoretically calculate vibrational energies corresponding to each mode **Table 1-1**. These absorptions occur at resonant frequencies which are the absorbed radiation matches the vibrational energies. Various modes of vibrations can be calculated and explained; asymmetric stretching, symmetric, rocking and wagging and so on.

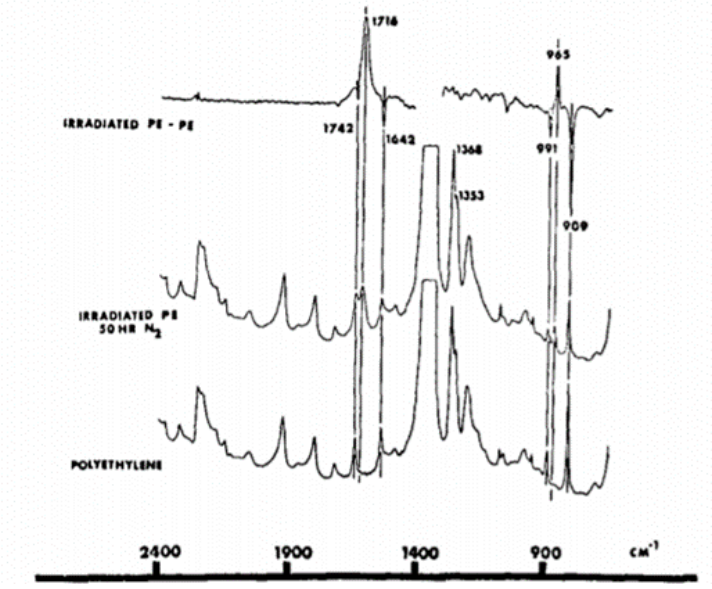

Figure 1-8. Infrared absorbance spectra for polyethylene film irradiated in nitrogen. Bottom, unirradiated polyethylene; middle, polyethylene irradiated for 50 h in nitrogen; top, difference spectrum (irradiated polyethylene-polyethylene). Reproduced from (*12*).

Table 1-1. Observed changes in infrared spectra of irradiated polyethylene films. Reproduced from (*12*).

Frequency (cm^{-1})	Assignments	Intensity change upon irradiation[a]
1742	R—C(=O)—H ν(C=O)	−
1716	R—C(=O)—R′ ν(C=O)	+
1642	R—CH=CH_2 ν(C=C)	−
1410	R—CH_2—C(=O)—CH_2—R′ $\delta(CH_2)$	+
1378	R—CH_3 $\delta_s(CH_3)$	+
1368	$\gamma_w(CH_2)$—amorphous phase	−
1353	$\gamma_w(CH_2)$—amorphous phase	−
1308	$\gamma_w(CH_2)$—amorphous phase	−
1261	$\gamma_w(CH_2)$—amorphous phase	−
1131	ν(C—O)	+
1068	ν(C—O)	+
991	R—CH=CH_2	−
965	*trans*-R—CH=CH—R′	+
909	R—CH=CH_2	−
800	Amorphous phase	−

[a] The symbols + and − represent an increase and decrease in band intensity upon irradiation, respectively.

1.5 Organization of the Thesis

Fourier transformed infrared spectroscopy is very common tool these days for chemical analysis. However, not many people know that this is not the full spectrum of vibrational modes that can be found in this IR range. We have been all blinded the largest portion of the IR spectrum. Conventionally, the IR region could be subdivided into three parts- near-IR, mid-IR and far-IR. Among them, what we can measure using prevalent FTIR instrument is from near IR to mid IR, mostly 200 to 12,800 cm^{-1}. There are enormous molecular vibrations in far-IR or terahertz (THz) range, 1 to 200 cm^{-1}, and they have been not much studied.

In this thesis, we experimentally demonstrate THz time-domain spectroscopy, THz time-domain polarimetry (THz-TDP) and find the molecular vibrations from biological samples. We are specifically interested in the understanding of chiral phonons of the (bio) materials.

This thesis is organized as follows:

Chapter 1. Introduction. In this chapter, we have discussed the universal phenomena of vibration and resonance, brief history of discovery of infrared rays and infrared spectroscopy and how light and matter interact.

Chapter 2. Terahertz Spectroscopy. In this chapter, the THz time-domain spectroscopy used in this work are described, including characterization, applications and a discussion on THz metamaterials.

Chapter 3. Terahertz circular dichroism spectroscopy of biomaterials enabled by kirigami polarization modulators. In this chapter, we describe that tunable optical elements fabricated from patterned plasmonic sheets with periodic kirigami cuts make possible realization of the modulation of terahertz beams under application of mechanical force.

Chapter 4. Chiral Photons in Biocrystals. In this chapter, we show that terahertz chiroptical spectroscopy enables registration and identification of chiral phonons in biocrystals of amino acids and medically relevant materials.

Chapter 5. Summary and Future Directions. In this chapter, we summarize the findings in this thesis, and how they inform future designs of kirigami optics. We also discuss the terahertz vibrations and their applications.

Chapter 2. Terahertz Spectroscopy

2.1 Introduction of THz radiation

The far-infrared, or terahertz (THz) occupies a middle ground between microwaves and mid-IR with frequencies in the range of 0.1 ~ 10 THz (*13*). This region of the electromagnetic spectrum is the emerging area which have huge potential for probing complex interactions between radiation and matter in various physical, chemical and biological systems. Since the photon energies is in the few meV range, THz photons interact with materials having characteristic lifetimes in the picosecond range and thus many vibrational relaxation energy states (*14*). Numerous practical applications have been introduced ranging from medical diagnostics, telecommunications, to chemical analysis (*14*).

2.2 Brief History of THz Spectroscopy

The very first report on THz radiation was in 1960. This paper described the generation of the first astronomical image using THz radiations (*15*). On the other hand, terahertz time-domain spectroscopy (THz-TDS) was firstly described by Grischkowsky et al. in 1989 (*16*). They use the optical excitation of photoconductive dipole antennas for generating THz rays and study the absorption of the water vapors. The technological advancement of THz-TDS is closely related to the development of ultrafast laser technology such as Ti:sapphire femtosecond laser . At the same

time, since THz radiation is in the middle between microwaves and infrared, it is linked to microwave technology as well as FTIR spectroscopy.

2.3 Generation and Detection of THz radiation

The THz radiation can be generated in a photoconductive switch on a semiconductor substrate excited by a femtosecond laser pulse. And vise versa, this photoconductive switch can also be used for a field-resolved detection of the THz field. The ultrafast current impulses generated by irradiating an ultrafast laser pulse onto a biased semiconductor make the many electron and hole pairs. These electrons which are excited are then recombined by the free charges accelerated by the applied bias field (*14*). The ultrashort THz pulses can be generated by this recombination with the characteristic time of the material (*14*). The schematics of generation of THz pulses by photoconductive switch is shown in **Figure 2-1** (*14*).

Interestingly, simple model of THz transient using the polarization field could predict many aspect of the THz generation. The calculated shape of the generated THz transient can be described as (*14*):

$$E_{THz}(t) \propto \frac{dj(t)}{dt}. \quad (1)$$

Figure 2-2 shows simulated THz radiation by altering the amplitude spectra for the two excitation intensities. Temporal dynamics of local electric field plays a pivotal role for the shape of the generated THz pulse. The main difference between two cases is attributed to the screening by the polarization field (*14*).

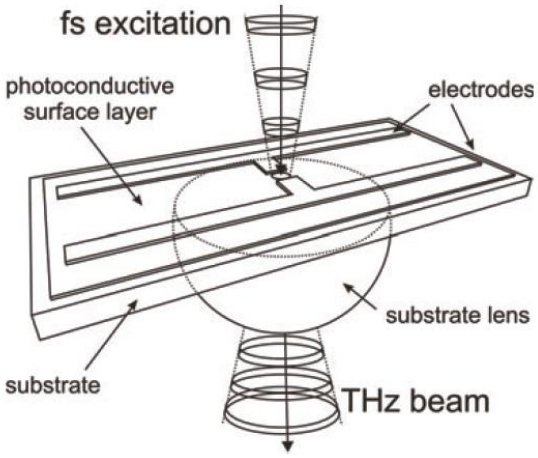

Figure 2-1 Photoconductive switch for generation of ultrashort THz transients that are collimated into a free-space beam. Reproduced from ref. (*14*).

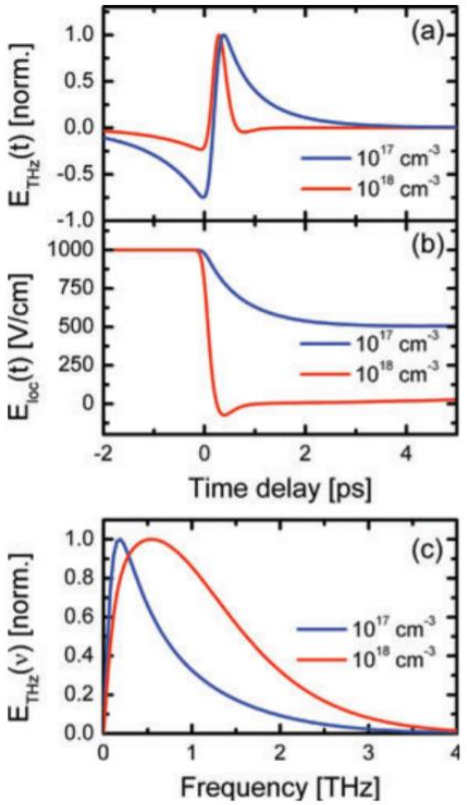

Figure 2-2 (a) Simulated THz pulse shapes, (b) dynamics of the local electric field, and (c) frequency spectra of the pulses at excitation levels 10^{17} cm^{-3} (blue) and 10^{18} cm^{-3} (red). Reproduced from ref. (*14*).

2.4 THz Optical Components

Most of the THz optical components that we can find is made of high-density polyethylene (HDPE), polytetrafluoroethylene (PTFE), polymethylpentene (TPX), quartz and high-resistance floating silicon (*17*). A conventional optical components such as lens normally made by continuously varying the thickness of the material and thus phase delays. Typical THz optical components are bulky, heavy and expensive due to the longer wavelength as shown in **Figure 2-3**(*17*).

To reduce the bulkiness of the THz components, diffractive optical elements (DOEs) have been thoroughly studied in this range. Most THz DORs are diffractive grating, Fresnel zone plates (FZP), and diffractive lenses (*17*). **Figure 2-4**a and **Figure 2-4**b show a THz diffraction grating and Fresnel lens, respectively. The big advantages of DOEs are they are light, thin and can be designed but suffering from the diffraction errors (*17*).

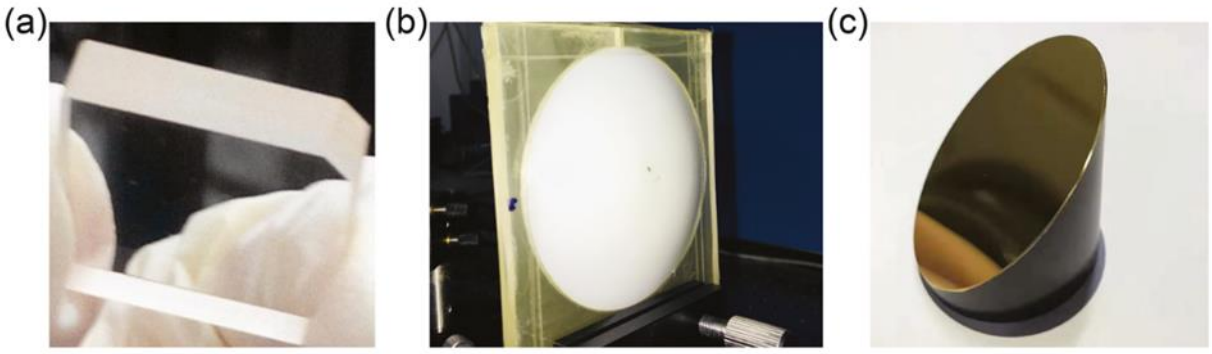

Figure 2-3 Common THz devices for wavefront modulation. (a) Quartz waveplate, (b) PTFE lens and (C) metallic paraboloidal mirror. Reproduced from ref. (*17*).

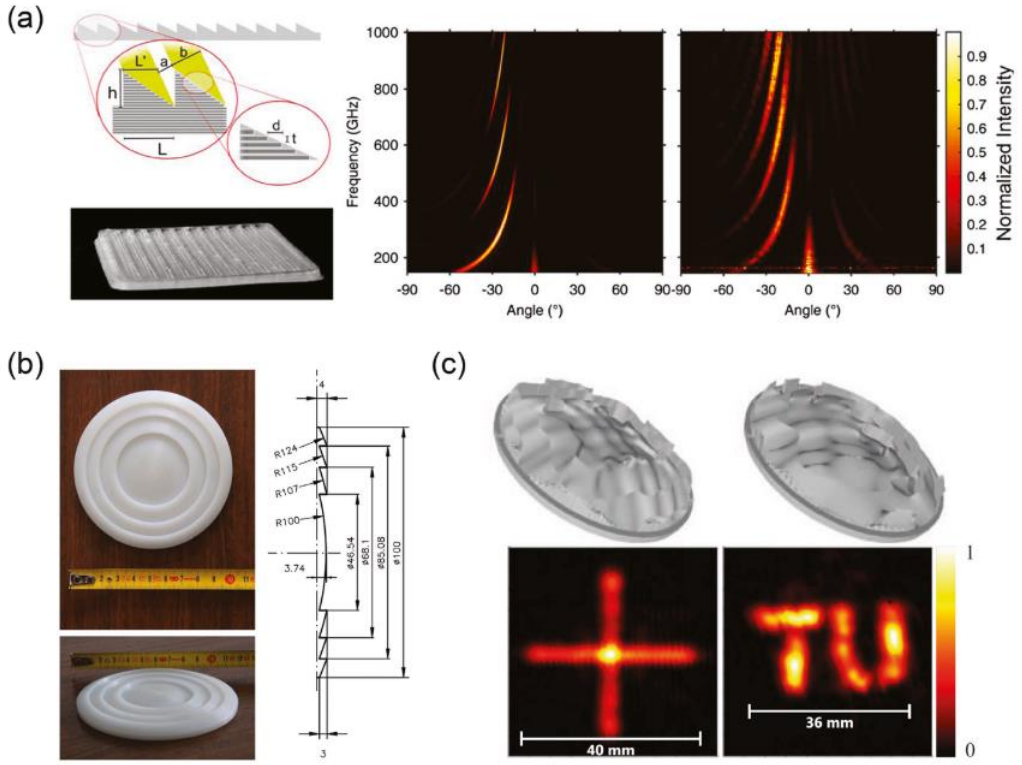

Figure 2-4 THz DOEs for wavefront modulation. (a) Photograph of a blazed transmission grating and the deflection of the THz wave caused by the grating, (b) Photographs and cross-section of a Fresnel lens working at 0.5 THz, and (c) computer models of the printed phase plates and images obtained in the experiment. Reproduced from ref. (*17*).

2.5 THz Metamaterials

Many optical components for THz radiations are not yet fully investigated. Scientists are working on developing THz lens, polarization modulators and absorbers. Metamaterials, which are artificial materials that could be engineered to produce desired properties, have been drawn much attention in THz range because many periodic arrays can be relatively easily fabricated using conventional photolithography method.

To replace the traditional wavefront modulators, researchers have begun to develop metamaterials. Optical meta-atoms can control the characteristic of the scattered wave by interacting with the incident wave (*17*). An exemplary case is the generation of the THz vortex beams with the topological numbers. **Figure 2-5**a shows the microscopic images of the designed metasurfaces for the vortex beams with different topological numbers (*18*). Not only for that, Airy and Lorentz beams can also be almost perfectly generated using the designed subwavelength antennas, as shown in **Figure 2-5**b,c (*19, 20*).

Although the flexibility of the metasurface design allows unprecedented functions and various designs are proposed, the single layer of periodic arrays of the meta-atoms suffer from low modulating efficiency (*17*). Many efforts have been made by employing multilayer metasurfaces. Typically the Fabry-Perot (FP) resonance is accompanied and it improves the polarization conversion efficiency (*17*). One of the best example of achieving high efficiency using multi-stacking metasurfaces is a double-layer structure consisting of a gold ground plane and a gold wire arrays (**Figure 2-6**) (*17, 21*). Anomalously, the refraction angel, 24°, of the cross-polarized wave is reported in **Figure 2-6**c.

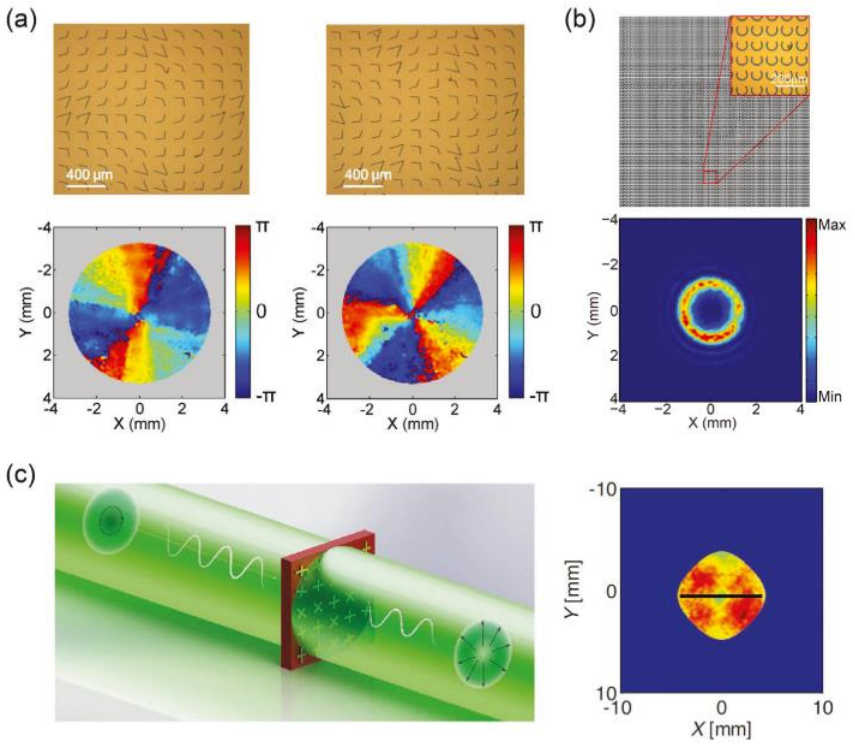

Figure 2-5 THz metasurfaces for special beams generation. (a) Designed metasurfaces for generating vortex beams with the topological numbers. (b) layout of the designed metasurface for ring-Airy beam generating and the measured intensity distribution of the beam on the initial plane. and (c) scheme of the metasurface for generating the THz radially polarized Lorentz beam and the measured radially polarized Lorenz beam at 0.75 THz. Reproduced from ref. (*17*).

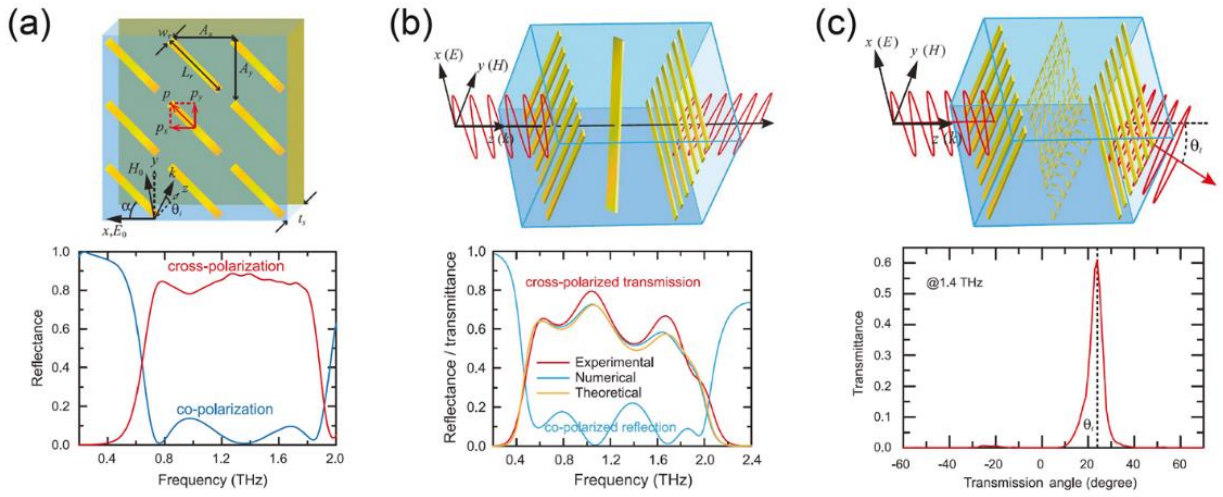

Figure 2-6 Multilayer metasurfaces with high efficiency in the THz waveband (*21*). (a) Top: Schematic of the unit cell of the reflective metasurface for broadband polarization conversion. Bottom: Measured reflectance of the electromagnetic wave with co- and cross-polarization. (b) Top: Schematic of the unit cell of the transmissive metasurface for polarization conversion. Bottom: Simulated reflectance of the electromagnetic wave with co-polarization, and the transmission spectrum of the electromagnetic wave with cross-polarization obtained through experimental measurements, numerical simulations, and theoretical calculations. (c) Top:Schematic of the transmissive metasurface for anomalous refraction. Bottom: Angle-dependent transmittance of the electromagnetic wave with cross-polarization at 1.4 THz. Reproduced from ref. (*17*).

2.6 Collective Vibrational Modes in THz range

It should be noted that when it comes to energy level of the radiation (**Table 1.1**), the corresponding type of bond for THz vibrations is the secondary bond while mid-infrared is the covalent bond (*22*). Secondary bond has the nature of the collective vibrational mode. This is because the bond strengths are very weak, thus they are subjected to neighbor's motion which means motion of adjacent molecules, bonds and their vibrations affect the behavior. As shown in this schematics, while mid-infrared is corresponding to 'localized' inter- atomic vibrations, terahertz vibrational mode is the concerted motion of the total molecular inter- and intra- vibrations (*22*).

	THz radiation	Mid- infrared
Energy level	1 - 50 meV	150 - 400 meV
Corresponding Type of bond	Secondary bond	Covalent bond
Vibration mode	'Global' Inter- and intra-molecular mode (Collective behavior)	'Localized' Inter-atomic mode (Stretching, wagging, Rocking)

Table 2-1 Comparison between THz radiation and mid-infrared light.

2.7 THz vibrations in biomolecules

We can find many examples that this concerted motion plays an important role in biomolecular complexes; such as amino acids, DNA, and proteins, which shows short- to long range organization of non-covalent bonds. Therefore, probing THz vibrations in these biomolecular complexes would be the key for comprehension of many biochemical reactions, synthesis and understanding from protein folding to tertiary or quaternary structures.

Although many promising applications have been expected, however, not much study have been done on these collective vibrations or phonon modes exist in this THz range. Just a few absorption spectra from a limited number of molecules have been reported with unknown vibrational origin. **Figure 2-7** shows an example of saccharides; *D*-glucose, fructose, sucrose and cellulose (*23*). It should be noted that these molecules are all consists of carbon, oxygen and hydrogen and they have ring structures and shows some similarity in chemical structure but their THz absorption spectra is distinctly different. More dramatic differences can be found in isomer case for the glucose for example. In isomer case, as you can see here, alpha and beta have exactly same chemical formula but subtly different arrangement of one hydroxyl side chain and it gives distinct THz spectra. Likewise, THz is very sensitive to impurities, ions and hydration states (*24*). The lower spectra in each figure in **Figure 2-8** is anhydrous form and upper spectra is hydrated. THz absorption spectra can clearly be distinguishable each hydration states of the molecules.

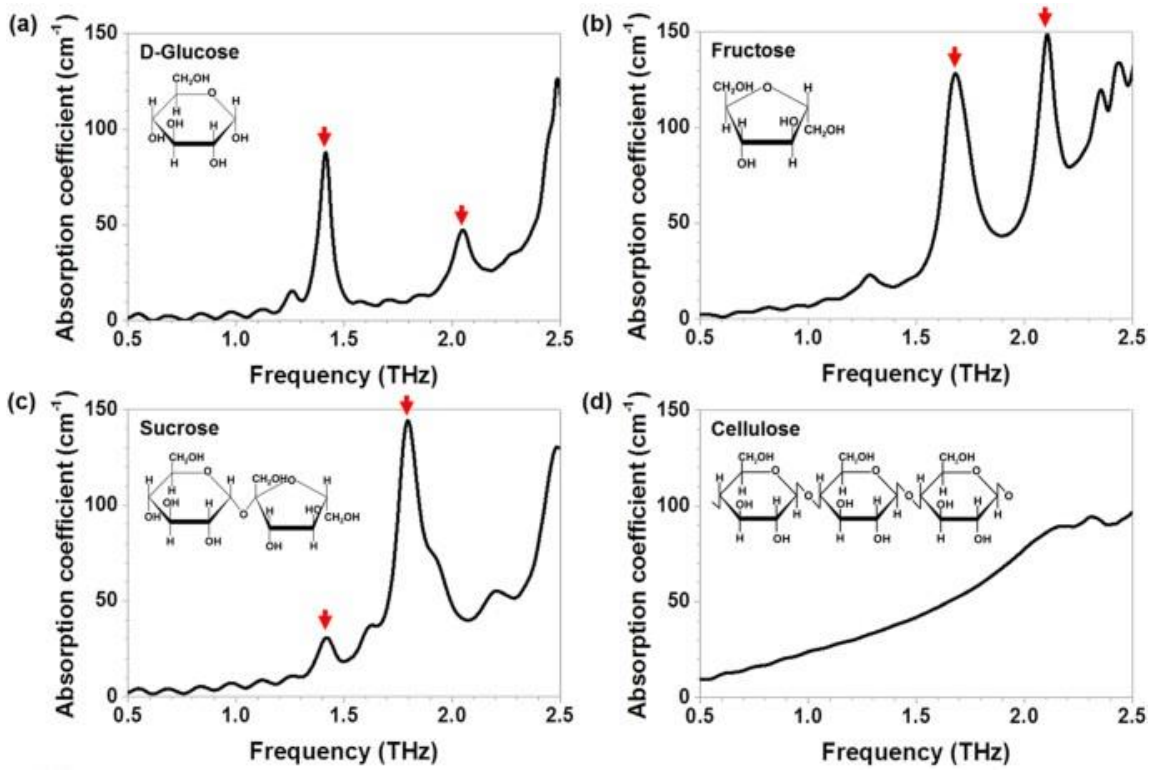

Figure 2-7 Absorption coefficients for various sugars and sweeteners extracted from THz transmittance measurement. Absorption coefficients at THz frequencies for (a) D-glucose ($C_6H_{12}O_6$), (b) fructose ($C_6H_{12}O_6$), (c) sucrose ($C_{12}H_{22}O_{11}$) and (d) cellulose ($(C_6H_{10}O_5)_n$) pellets. The insets in (a–d) show the structural formulas of each saccharide. Reproduced from ref. (*23*).

.

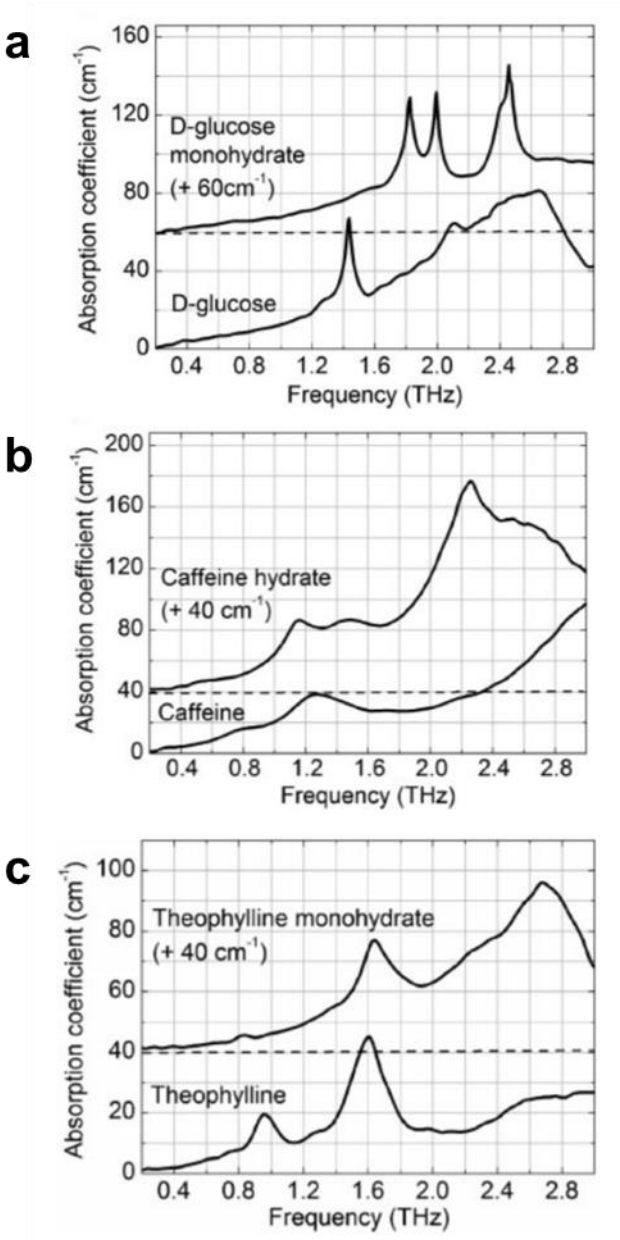

Figure 2-8 (a) THz absorption spectra of anhydrous D-glucose and D-glucose monohydrate (both have a 50% w/w in polyethylene) (b) THz absorption spectra of anhydrous caffeine and caffeine hydrate (both are pure samples) (c) THz absorption spectra of anhydrous theophylline and theophylline monohydrate (both have a 33% w/w in polyethylene). Reproduced from ref.(*24*).

2.8 Challenges

THz phonon mode is very important because it has information of molecular vibrations that are very specific to molecular structures, phases, impurities and hydration states. However, by just using THz absorption spectra, we could not analyze it further except obtaining peak positions of resonance frequencies. We need more sophisticated spectroscopic capability to assign the vibrational motion and understand the phonons. Several problems have prevented the observation and identification of THz phonons. First, computational predictions with complex unit cells are proven to be difficult because the diversity of non-covalent interactions, non-harmonicity and multiplicity of the coupled modes possible for biological crystals require a large number of atoms with multiple degree of freedom. Thus, it is almost impossible to investigate further without experimentally validated results. Experimental point of view on the other hand, the biggest problem is that the methods of chiroptical spectroscopies in THz range are far from being trivial. As you may already noticed here, as shown in this figure, abundant chiral vibrational modes can be expected for these intrinsically chiral biocrystals. Chirality is important concept here because not only describes the left- or right-handed behavior but holds the signatures of the complex topological network of non-covalent bonds. However, thus far, experimental and theoretical any toolbox for their observation and identification is unknown.

Chapter 3. Terahertz Circular Dichroism Spectroscopy of Biomaterials Enabled by Kirigami Polarization Modulators[1]

3.1 Introduction

Scientific and technological advances related to chirality of liquid crystals, biomolecules, and synthetic drugs were enabled by the prior development of chiroptical spectroscopies, notably electronic circular dichroism (ECD) and vibrational circular dichroism (VCD), which enable identification and quantification of mirror asymmetry at molecular and nanometer scales. ECD and VCD are based on the modulation of circularly polarized light with photon energies in the ranges of 1.5-7 eV and 0.07-0.5 eV, respectively, which limit the physical dimensions and the resonant energies of the chiral structures that can be probed. Of particular interest is the far infrared (IR) or terahertz (THz) region of the electromagnetic spectrum corresponding to wavelengths in the range 0.1-1 mm and photon energies from ~0.001 eV to ~0.01 eV (*21*, *25–28*). Besides being informative for many areas of THz studies from astronomy and solid-state physics

[1] From Won Jin Choi, Gong Cheng, Zhengyu Huang, Shuai Zhang, Theodore B. Norris and Nicholas A. Kotov "Terahertz Circular Dichroism Spectroscopy of Biomaterials Enabled by Kirigami Polarization Modulators" *Nature Materials* **18**, 820-826 (2019) (*1*).

Contributions: W.J.C., G.C., T.B.N. and N.A.K. contributed to the design, data analysis and preparation of the manuscript. N.A.K. originated the concept. W.J.C. designed and fabricated the kirigami modulators and measured the mechanical responses. W.J.C. and G.C. performed the optical experiments and W.J.C., G.C. and Z.H. performed the simulations. S.Z. provided technical support for reconstruction of the 3D kirigami model. W.J.C., G.C., T.B.N. and N.A.K. planned and supervised the project.

to telecommunication, THz circular dichroism (TCD) is essential for understanding of biomaterials, biomolecules, and pharmaceuticals because the energy of THz photons enables probing the 'soft' oscillatory motions of biomolecules (*29–33*). The practical realization of TCD, however, has proven to be an elusive goal due to the difficulties with polarization modulation of THz radiation. The key problem is the lack of optical components for modulation of circular polarization in the THz regime, which is easily accomplished at shorter wavelengths using photoelastic modulators (PEM), half- and quarter waveplates, and lately with chiral metamaterials and metasurfaces (*25*, *34–37*). Although the modulation of linearly and circularly polarized THz beams has been demonstrated with fairly complicated and bulky optical systems based on THz metamaterials, e.g. with pneumatic control of scattering elements (*38*), sufficiently strong and dynamic polarization rotation of THz radiation remains a significant challenge (*25*, *34–37*).

3.2 Circular Dichroism Spectroscopy

To understand chiral phonon mode, what we need is chiroptical spectroscopy. In general, one of the most effective tools for observing chiroptical response from sample is circular dichroism spectroscopy or in short CD spectroscopy. It is a form of light absorption tool that measures the difference in absorbance of right- and left-circularly polarized light (*39*). The CD spectroscopy consists of three major optical components; light source, detector and a quarter waveplate modulator. Quarter waveplate modulator is exploited by birefringent materials that can convert linearly polarized light into circularly polarized light (*40*). The CD spectra were obtained by subtracting the absorbance of right circularly polarized light from that of left. We have THz source and detector and, we have THz lens, optical fibers and so on, but we still don't have quarter waveplate modulators which are the key components of generating circularly polarized THz beam.

3.3 Quarter Waveplate Modulator

Waveplates are constructed out of a birefringent material, for which the refractive index is different with respect to the perpendicular crystal axes (*40*). Quartz and calcite are perfect waveplates for UV to visible range, whereas zinc selenide crystals can make circularly polarized light for mid-infrared but there is no materials have been reported for THz range, at least using the crystals that can be found in nature (**Table 3-1**).

Range (Wavelength)	Materials
250 nm ~ 1550 nm	Quartz ,Calcite
3 μm ~ 7 μm	MgF_2
8 μm ~ 9 μm	Cadmium Thiogallate
10 μm ~ 15 μm	Zinc Selenide

Table 3-1 Materials for optical waveplates (UV to IR modulators) (*41*, *42*).

3.4 Kirigami Modulator

Kirigami, the oriental art of paper cutting, presents a powerful tool to create complex and tunable three-dimensional (3D) geometries from simple (2D) two-dimensional cut patterns, which can be scaled across many orders of magnitude to yield macro to nanoscale structures (*43–48*). The ability to achieve out-of-plane deformations and designed 3D shapes, the robustness of the patterns under cyclic reconfiguration and the manufacturing simplicity of kirigami structures together promise untapped possibilities for the efficient modulation of THz optical beams. Here we show that kirigami optics affords real-time modulation of THz beams with polarization rotation and ellipticity angles as large as 80° and 40° over thousands of cycles, respectively. The unusually large amplitudes of polarization rotation and ellipticity angles were enabled by double-scale patterns comprised of microscale metallic stripes together with wavelength-scale kirigami cuts.

3.4.1 Fabrication of Kirigami modulator

Poly(methyl methacrylate) (PMMA 950 C4, Microchem) is spin-coated (3000 rpm) on a 4 in. silicon wafer as a sacrificial layer and baked subsequently on a 180° hot plate to dry. Parylene C (SCS Inc.) is deposited on the PMMA-coated silicon wafer by a chemical vapour deposition system (PDS 2035CR, SCS Inc.). The thickness of Parylene C is set to ~6 μm and confirmed by surface profiler (Dektak XT, Bruker) after deposition. Herringbone patterned thin layers of chromium (~5 nm) and gold (~45 nm) are deposited on the Parylene C using electron beam evaporator (Enerjet evaporator) after a standard photolithography processes (MA/BA6 Mask/Bond aligner, Suss Microtec). Kirigami patterns are generated by additional photolithography on top of herringbone patterned substrate and followed by deposition of aluminum (~70 nm) as a masking

layer for the reactive ion etching process. The corresponding patterns are formed by reactive ion etching (LAM 9400, Lam Research) of Parylene C. Lastly, the whole patterned wafer is soaked in aluminum etchant solution (Aluminum etch Type A, Transene) to remove the aluminum masking layer and in acetone to dissolve the PMMA sacrificial layer. The released kirigami sheet is rinsed carefully with isopropyl alcohol and distilled water and dried. The schematic is shown in **Figure 3-1** to clarify each step.

3.4.2 Dimension of kirigami pattern and definition of slant angle (φ)

Figure 3-2A shows a top view of the kirigami cut pattern without Au strips to exhibit the dimensions of the cut pattern. The length (L_{cut}) and height (H_{cut}) of each cut is 500 μm and 5 μm, respectively. The horizontal and vertical spacings between cuts are set to 100 μm resulting in a horizontal period of 600 μm and a vertical period of 105 μm. A detailed view of a single unit of slanted Au strips is shown in **Figure 3-2B**. The width of each Au strip is set to 5 μm. The width and height of the total domain are 300 and 80 μm, respectively. Here, the slant angle (φ) is defined as the angle between the cut direction and the longer axial direction of the Au strips, as shown in **Figure 3-2B**. In this work, we tested kirigami samples with four different angles φ: 15°, 30°, 37.5° and 45°. **Figure 3-2C** shows a top view of the double pattern kirigami, that is, the kirigami cut pattern together with the Au herringbone pattern. The red box indicates the unit cell of the extended modulator structure. The width (W_{unit}) and height (H_{unit}) of unit cell are 600 and 210 μm, respectively.

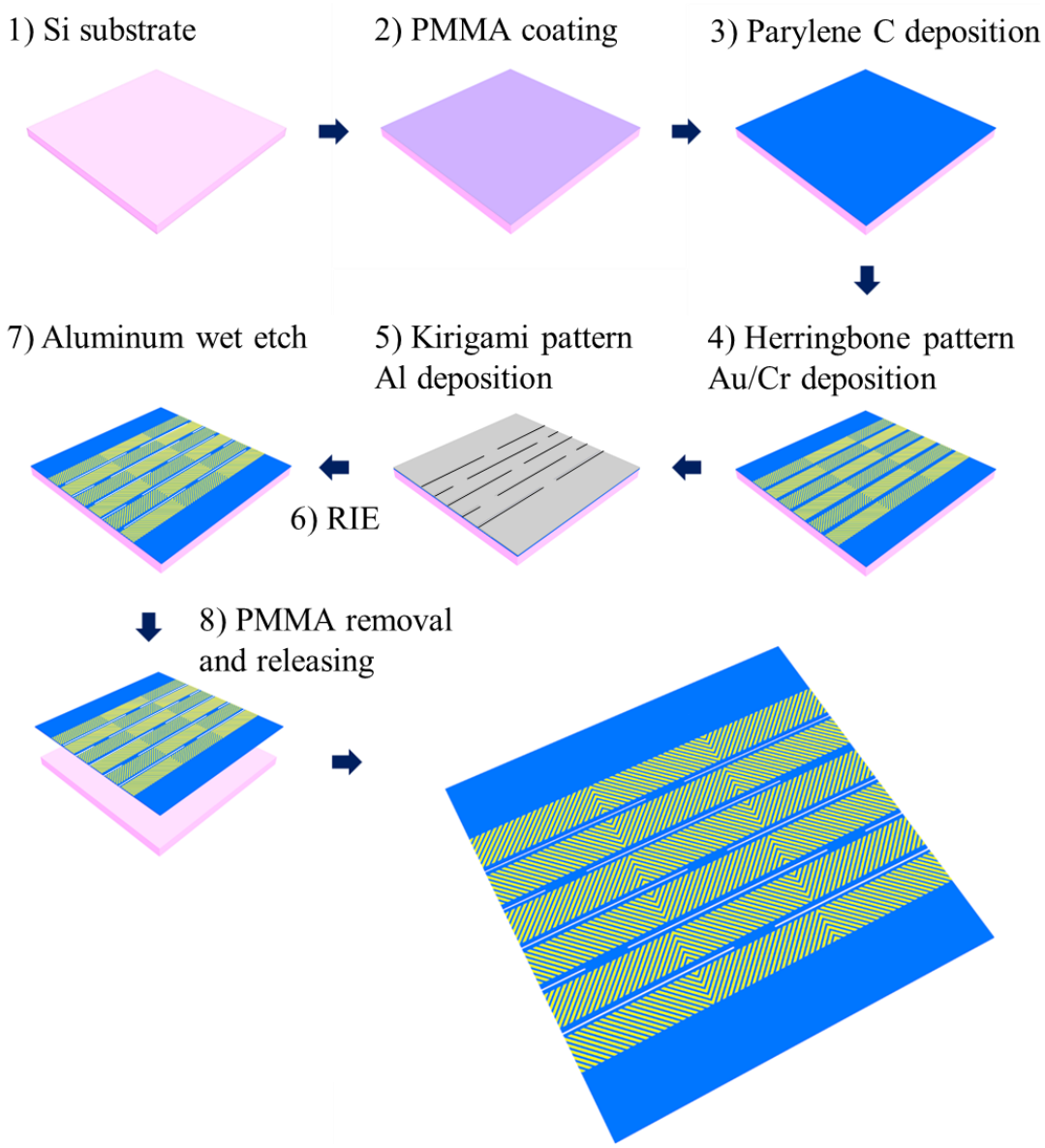

Figure 3-1 Fabrication of kirigami modulator. Schematic illustration of the steps in fabrication processing. PMMA is applied as a sacrificial layer and subsequently ~6 μm thick Parylene C is deposited. Patterned Cr/Au layer is deposited by photolithography and electron beam evaporator. To introduce kirigami cut to Parylene C, additional Al layer is deposited for masking reactive ion etching (RIE). After RIE, the wafer is soaked in aluminum etchant solution and in acetone to release. Reproduced from ref.(*1*).

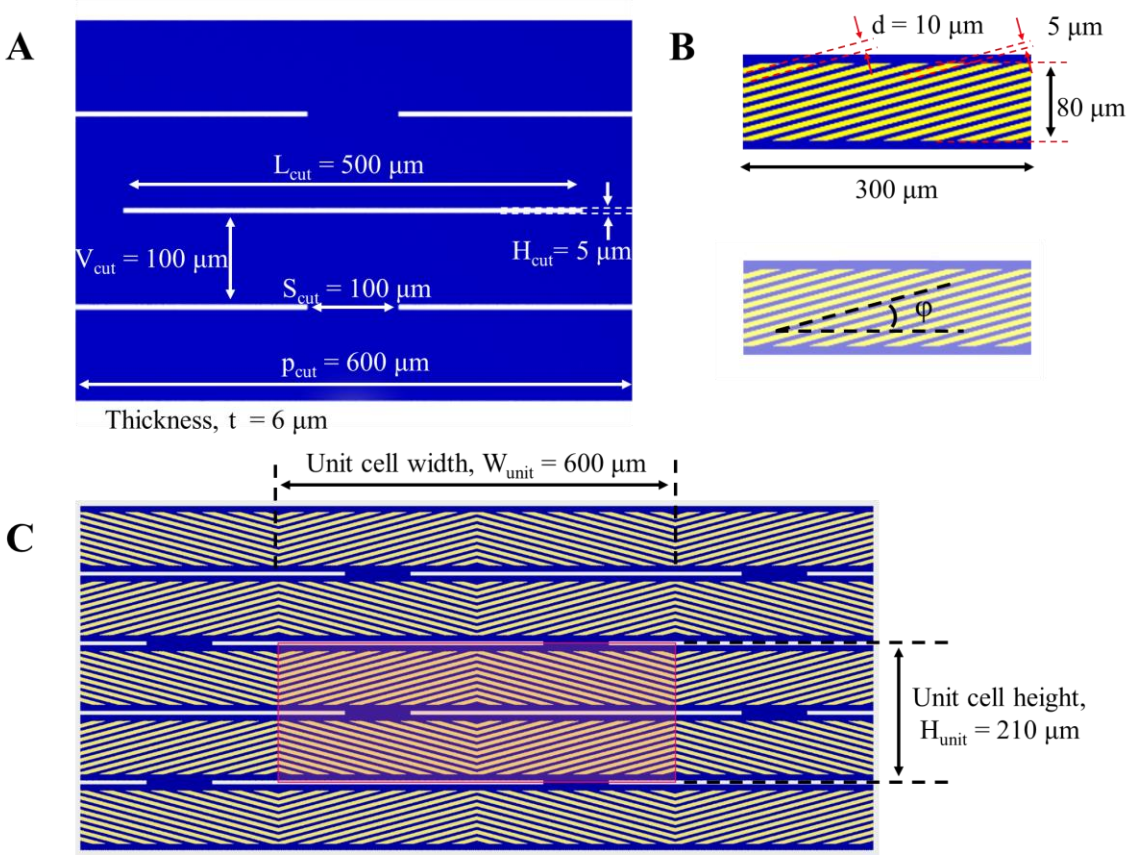

Figure 3-2 Detailed dimensions and definition of slant angle in chiral kirigami pattern. (A) Top view of kirigami cut pattern. The length (L_{cut}) and the height (H_{cut}) of each individual cut are 500 μm and 5 μm, respectively. The horizontal (S_{cut}) and vertical (V_{cut}) spacing between cuts are set to 100 μm. (B) Detailed view of single unit of slanted Au strips. Width of each Au strip is set to 5 μm. Width and height of total domain of Au strips are 300 and 80 μm, respectively. Here, the slant angle (φ) is defined as angle between longitudinal direction of cut and Au strip. (C) Top view image of aligned kirigami cut pattern and Au herringbone pattern. Red box indicates the unit cell of this double pattern. Width (W_{unit}) and height (H_{unit}) of unit cell are 600 and 210 μm, respectively. Reproduced from ref.(*1*).

3.4.3 Stress concentrators to control handedness of kirigami sheets

In this study, we achieved strict control over the handedness of kirigami sheets over thousands of deformation cycles by adding stress concentrators at the end of the kirigami patterns, as shown in **Figure 3-3**. These stress concentrators are made of thin gold films and this area is more likely to acquire a convex shape under stress due to residual stress in the film. Without the stress concentrators, *L*- and *R*-domains are mixed, which reduces the polarization rotation.

3.4.4 Integration kirigami sheets with piezo-controller

Fabrication of the chiral kirigami modulators is completed by integrating the kirigami sheet with a piezo-controller for the application of controlled strain (ε). We used a U-521 PI Line (PI instrument) linear position stage with 3D printed sample holder. For the stacked configuration used in terahertz circular dichroism (TCD) measurements, we used two U-521 piezo-controllers and manipulated them individually. This piezo-controller can be programmed with very high spatial precision of 0.1 μm (ε = 0.001%). The applied strain values of 2.3, 4.5, 9.0, 13.5, 18, 22.5 % in the measurements presented in the main text and supporting materials is calculated from stretching distances of 0.2, 0.4, 0.8, 1.2, 1.6, 2.0 mm, respectively.

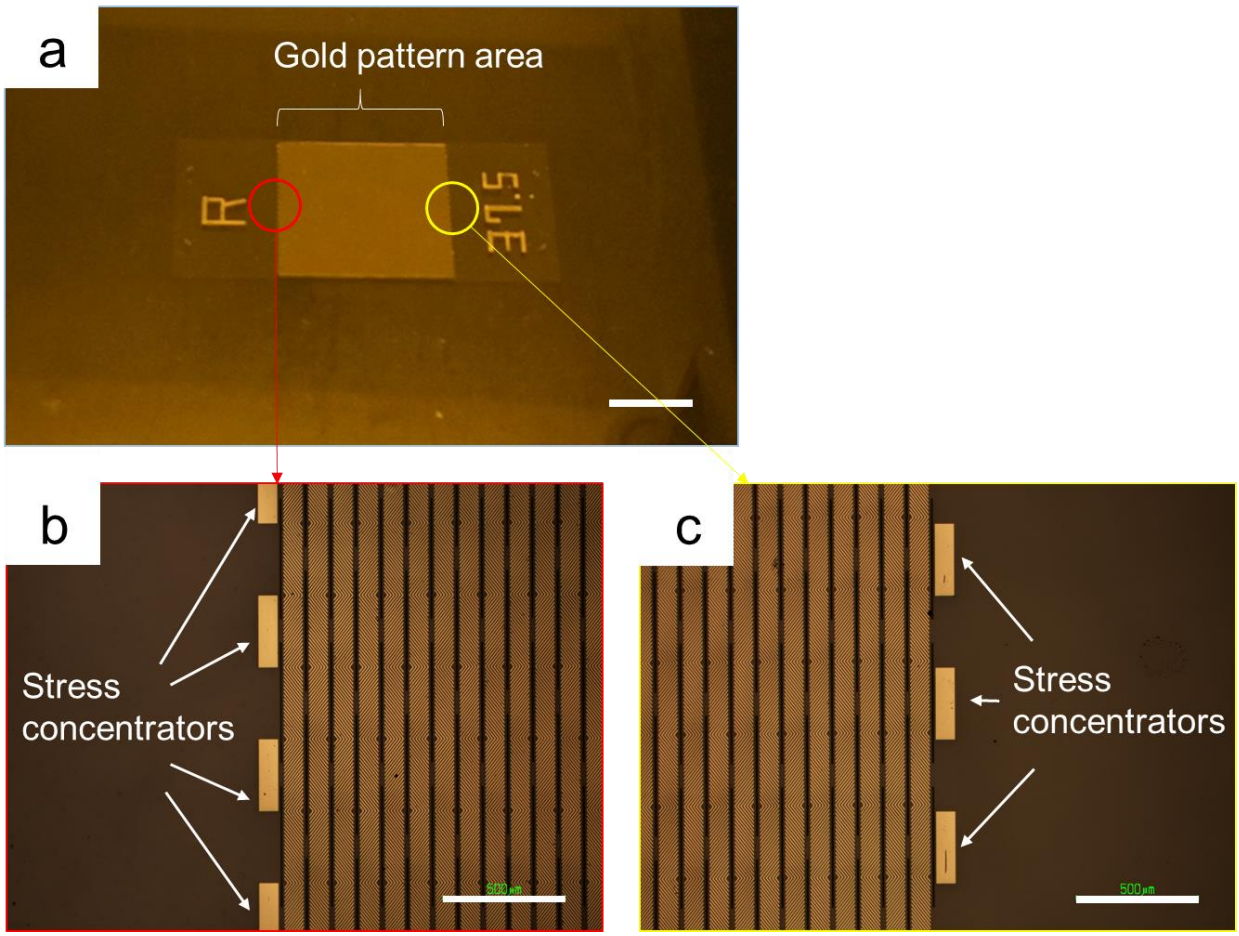

Figure 3-3 Stress concentrators to control handedness of kirigami sheets (a) Photo image of kirigami substrate. Scale bar is 1 cm. (b) and (c) show the optical microscope images of the end of the pattern. (b) and (c) show red and yellow circled area, respectively. White arrows indicate the asymmetric set of stress concentrators. Scale bars in (b) and (c) are 500 μm. Reproduced from ref.(*1*).

3.4.5 Function-defining structural feature of kirigami modulators

The kirigami modulators in this study are made from parylene - a stiff polymer (Young's modulus E = 2.8 GPa) with high transparency across the THz spectrum (*49*). Parylene sheets were patterned with straight cuts in a face centered rectangular lattice with a periodicity of p_{cut} = 600 μm (**Figure 3-1** and **Figure 3-2**). This 2D pattern transforms upon stretching into an array of alternating convex and concave out-of-plane surfaces due to buckling (**Figure 3-4**).

The function-defining structural feature was a gold herringbone pattern with D_n symmetry (chiral dihedral point group) (*50*) deposited on parylene sheets in registry with kirigami cuts. When buckled, the patterned surface is transformed into a homeomorph of a three-dimensional helix (**Figure 3-4**). Its pitch varies under mechanical strain while its long axis remains aligned with the surface normal (z-axis) and with propagating THz beam. Unlike rigid 3D structures discussed in the prior studies, including micro-fabricated metallic helices (*51*), micro-electro-mechanical systems (MEMS) (*34*, *38*) and origami/kirigami based chiral metamaterials (*45*, *52*, *53*), 'soft' double-patterned kirigami structures enable strong and tunable polarization rotation with real time modulation capability. Their confocal microscopy images (**Figure 3-6** and **Figure 3-7**) obtained for strains ε from 0 % to 22.5 % demonstrated that buckling and tilting of each out-of-plane segment occurred simultaneously for the entire sheet, which is essential for uniform polarization front of a beam. The reconstructed contour maps of left-handed (*L*-) and right-handed (*R*-) kirigami structures (**Figure 3-6** and **Figure 3-8b**) at ε = 22.5% strain indicate that the edges of the buckled elements extended to 68 μm symmetrically along the positive and negative z-axis. Tuning the radius and pitch of the clockwise and counter clockwise half-helices (*46*, *51*) are the two key factors for controlling electrodynamic interactions of these structures with left- and right circularly

polarized photons. The experimental deformations matched the predictions from finite-element modeling exactly (**Figure 3-6c** and **Figure 3-6d**).

3.4.6 Mechanical and cycling characterization of kirigami sheets

The high elasticity and tunability of kirigami sheets are significant advantages of kirigami chiroptical modulators. This is because a network of notches made in a rigid substrate greatly increases the ultimate strain that can be applied to the sheets and prevents unpredictable local failure (*54*). Uniaxial tensile tests were performed by means of a TA.XT *plus* Texture Analyzer (Texture Technologies) and the *Exponent* (Texture Technologies) software package for tensile and cycling tests with a 0.5 N load cell at a constant strain rate of 0.2% per second. The engineering stress-strain data were obtained and each curve was averaged over 5 samples. Our kirigami modulators were found to reach strains as high as 150% without failure (**Figure 3-5**). Before cutting, the pristine parylene sheets shows a strain of 3.8%. In contrast, a kirigami cut significantly modifies the deformation behavior of a sheet, resulting in a lower stiffness and higher elongation than a pristine sheet, as seen in **Figure 3-5**. In the stress-strain curves, the kirigami sheet's initial state at < 4% strain is elastic in-plane deformation (**Figure 3-5B**, blue section). As the applied stress exceeds a critical strain, the domains of the kirigami structure start to deform elastically in out-of-plane directions. Within this region (**Figure 3-5B**, pink section), buckling occurs as the domains rotate to align with the direction of tensile stress as shown in **Figure 3-6** and **Figure 3-7**. After that, plastic deformation occurs and finally failure begins when one of the cuts begins to tear and crease (**Figure 3-5B,** white section) (*54*). Since we only apply strains up to 22.5% to achieve out-of-plane deformations with convex and concave domains, the deformation is completely

within the elastic region. **Figure 3-5C** shows the stress-strain curve after 10,000th cycle of stretching and releasing and surprisingly it is nearly identical to its initial curve.

3.4.7 Finite-element modeling for mechanical characterization

Commercial finite-element software (COMSOL Multiphysics 5.2a, COMSOL Inc.) was used to explore the strain distribution in kirigami sheets, which yields insight into the basic mechanisms governing deformation behavior. An approximate global mesh size of 2.5 μm was used. We set the following boundary condition on each side of the kirigami sheet in the axial direction: 1) at one end we fix it and no displacement is allowed to this boundary; 2) at the opposite end we enforce a load in the axial direction. Since, in real systems, there is always an asymmetrical force, we apply a very small bias force (approximately 10^{-4} times smaller than the load) on top edge of each cut and then pull in the axial direction (*54*). The finite-element modeling shows that high elasticity is due to the even distribution of stress over the kirigami sheet rather than concentrating on singularities (**Figure 3-6D** and **Figure 3-6E**) (*54*).

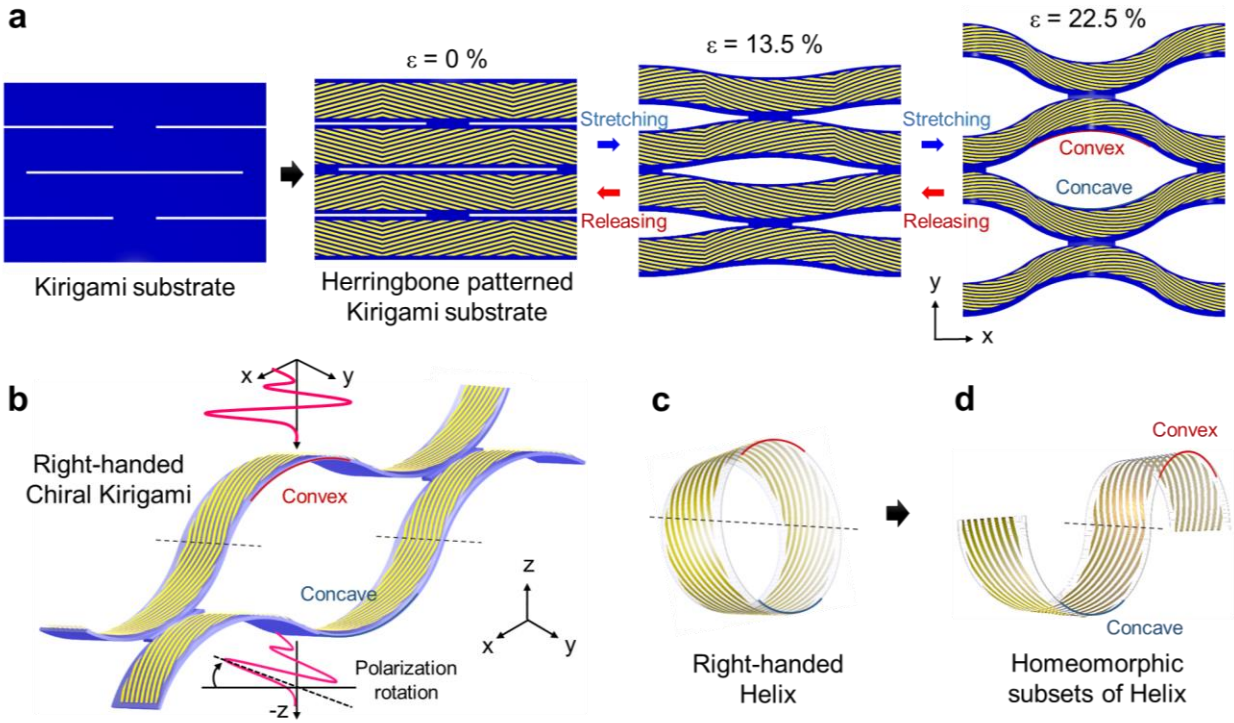

Figure 3-4 Schematic of chiral kirigami topology. a, Herringbone structured Au strips are deposited on the kirigami substrate. This chiral kirigami topology can tune the polarization rotation angle and ellipticity by mechanical force. **b,** Stretched chiral kirigami metamaterial that is topologically equivalent helix structure. **c,** Standard right-handed helix structure whose outside is covered with slanted striations. **d,** Geometric structure displaying homeomorphic subsets of right-handed helix. Reproduced from ref.(*1*).

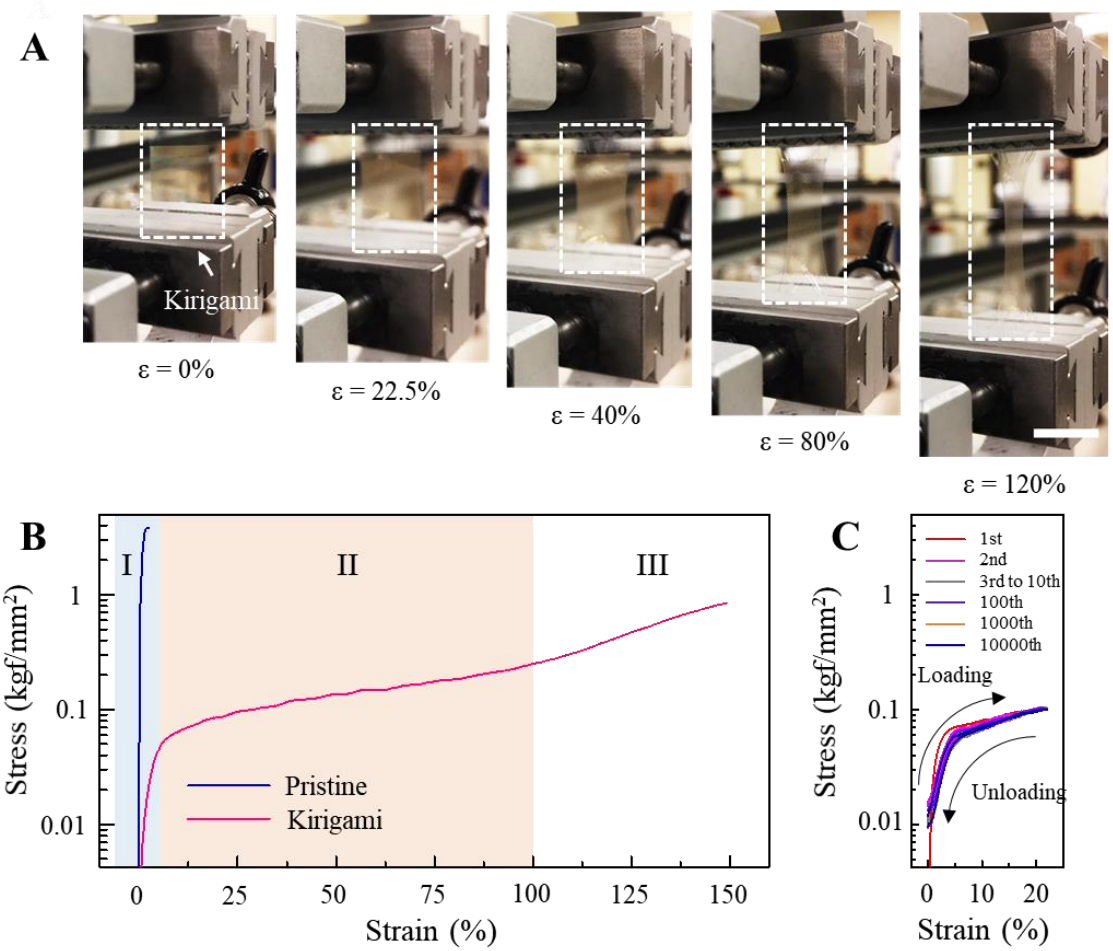

Figure 3-5 Stretching and cycling properties of kirigami modulator (A) Photo images of the kirigami at strain values of 0%, 22.5%, 40%, 80% and 120% (from left to right). (B) and (C) Stress-strain curves and their cycling properties of chiral kirigami modulator. Sections I (blue), II (pink) and III (white) indicate the regions of in-plane elastic deformation, out-of-plane elastic deformation and plastic deformation with pattern collapse, respectively. Scale bar in (A) is 2 cm. Reproduced from ref.(*1*).

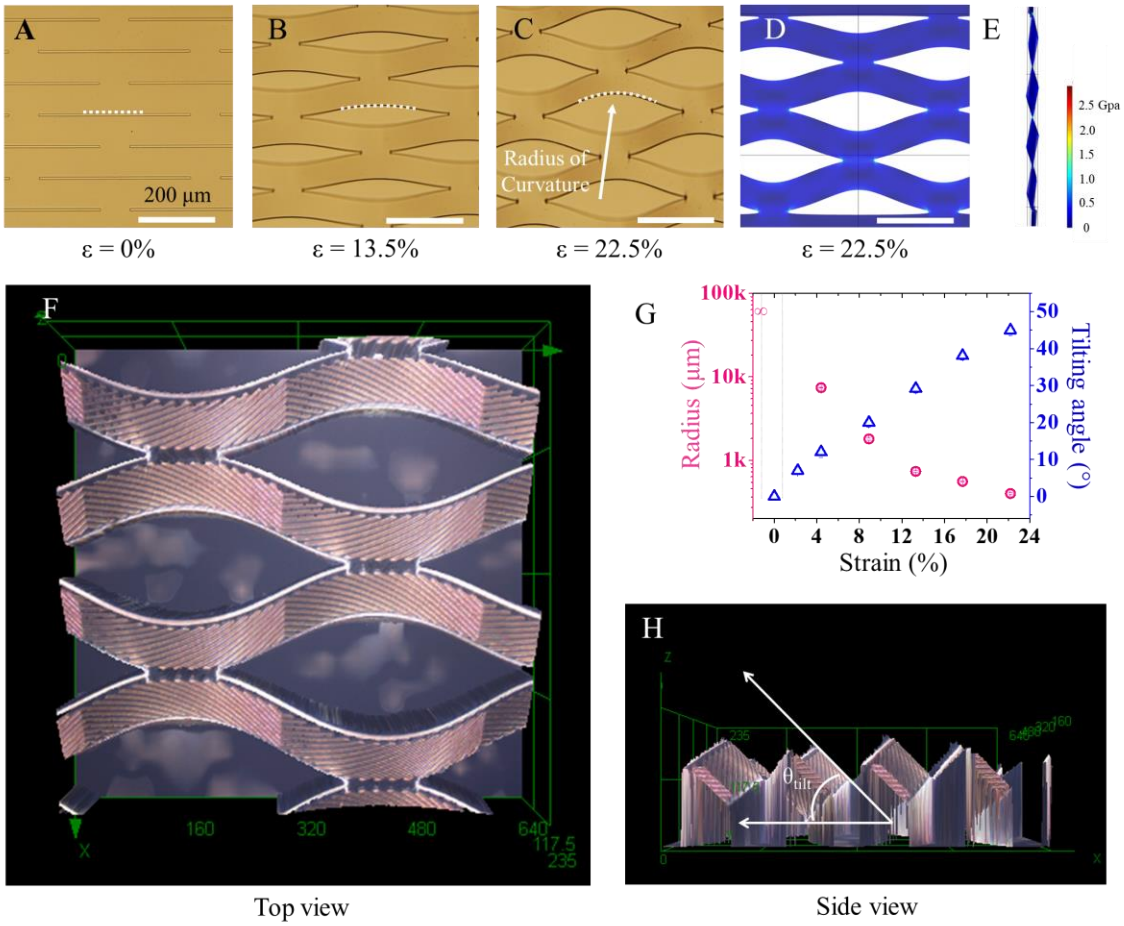

Figure 3-6 Structural evolution of kirigami modulator under tensile stress. (A) to (C) show the optical microscope images of kirigami cut parylene at strain values of 0%, 13.5% and 22.5%, respectively. (D) and (E) show the top view and side view of stress distribution visualization in FEM, respectively. (F) and (H) show the top and side view kirigami at ε = 22.5% strain captured by laser confocal microscopy, respectively. Here, the tilting angle (θ_{tilt}) is defined as the angle between x axis and the line parallel to the surface of the kirigami sheet as shown in (H). (G) shows the radius of the cut and tilting angle of the kirigami domain with respect to the strain (%). The radius of the cut edge was varied from almost infinity, i.e. flat line, to ~400 μm round while tilting angle changed from 0° to 45°. Reproduced from ref.(*1*).

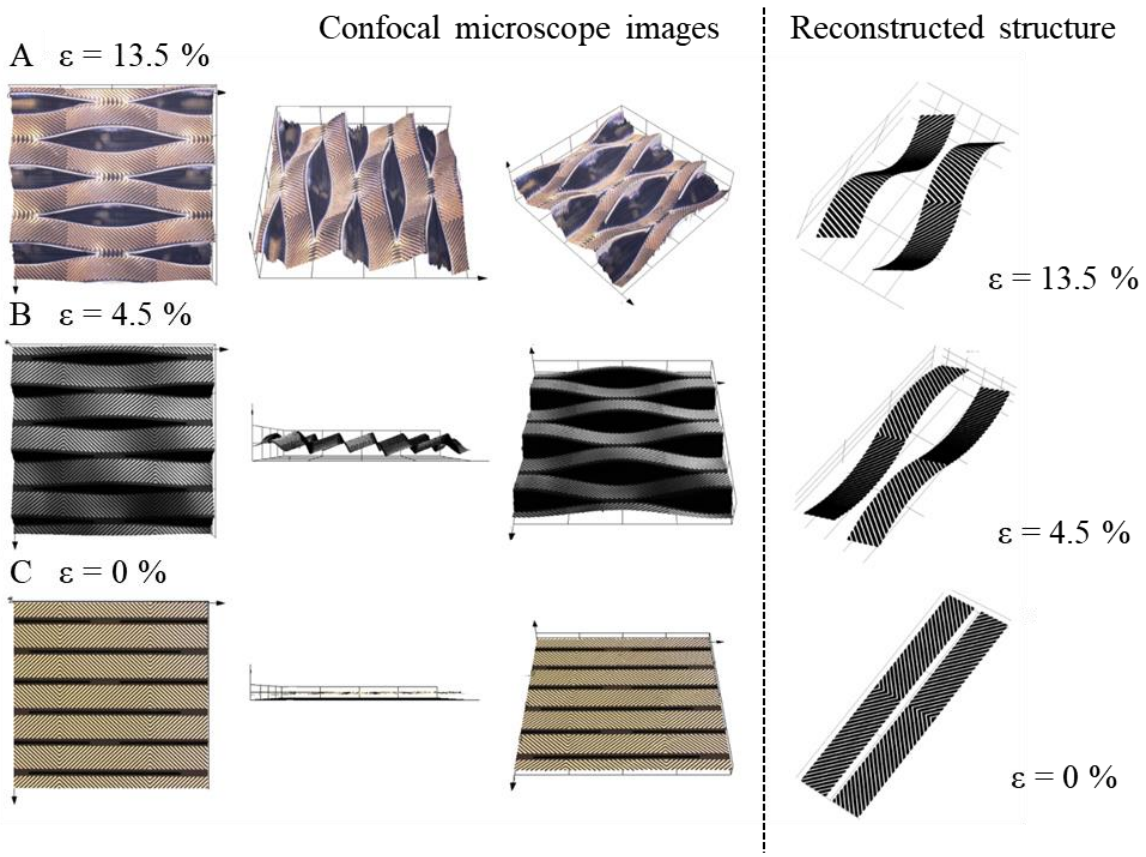

Figure 3-7 Confocal microscopy images and reconstructed 3D models of kirigami modulator under three different strains. The three rows correspond to the same right-handed sample with a 45° wire slant angle under (A) 13.5%, (B) 4.5% and (C) 0% strains, respectively. The first three columns are the images of three different viewpoints from the confocal microscopy under a 20x objective. The last column are the reconstructed 3D models corresponding to each strain. Reproduced from ref.(*1*).

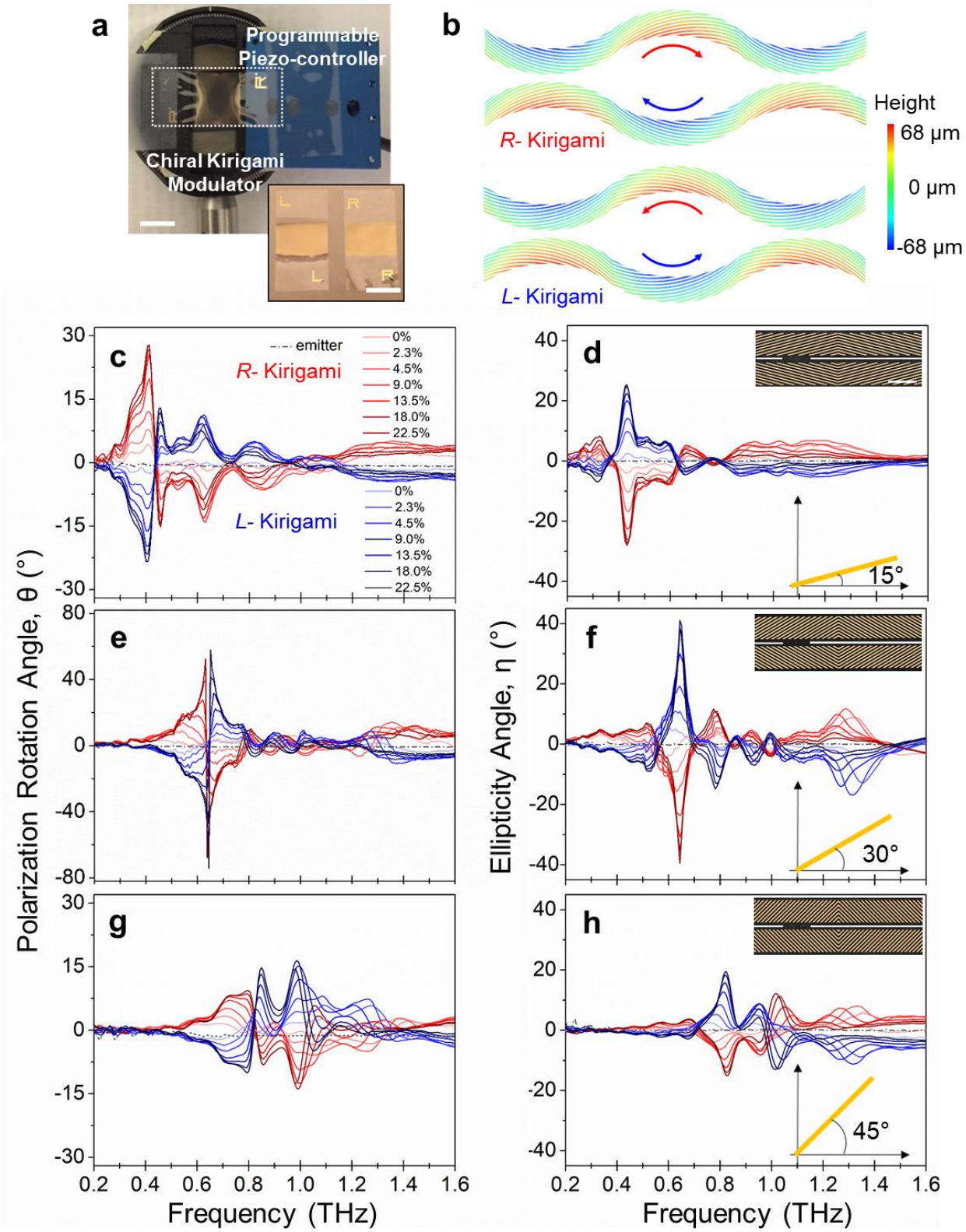
a
Programmable
Piezo-controller
Chiral Kirigami
Modulator
b
R- Kirigami
L- Kirigami
Height
68 μm
0 μm
-68 μm
c
emitter
R- Kirigami
L- Kirigami
0%
2.3%
4.5%
9.0%
13.5%
18.0%
22.5%
d
15°
e
f
30°
g
h
45°
Polarization Rotation Angle, θ (°)
Ellipticity Angle, η (°)
Frequency (THz)
Frequency (THz)

Figure 3-8 THz-TDS measurement of chiral kirigami modulator. a, kirigami mounted on the 3D printed rotatable optical holder with piezoelectric controller. Subset figure shows photo image of left and right handed chiral kirigami substrate. Yellow shiny region is the herringbone patterned Au zone. Both of scale bars are 1 cm. **b,** Contour map of kirigami modulator reconstructed from laser confocal microscope images. **c, e and g,** Results of polarization rotation angle of kirigami having slanted Au angles (φ) of 15, 30, 45 degree with respect to strain (%), respectively. **d, f and h,** Results of consequent ellipticity angle of kirigami having slanted Au angles (φ) of 15, 30, 45 degree with respect to various strain, respectively. Note that the y-axis range for polarization rotation angle for the kirigami with φ=30° (**e**) is larger than others (**c** and **g**). One can notice that there is an approximately 0.2 THz increment per 15° change of φ. As can be expected by the Kramers-Kronig relation (*38*), the ellipticity exhibited a dispersive curve and crossed zero at slightly off-resonance frequencies, where the polarization rotation showed maximum. Inset shows optical microscope images of each kirigami samples. Scale bar in **d** is 100 μm. Reproduced from ref.(*1*).

3.5 Terahertz Measurements of Kirigami Modulators

THz time-domain spectroscopy (THz-TDS) over the range 0.2-2 THz was used to characterize chiroptical performance of the kirigami modulators. Throughout this chapter, we used two complementary methods. In the first, to determine the polarization rotation angle, θ, and ellipticity angle, η, and the TCD activity of the THz beam after passing through kirigami sheets, we used calculations of Stokes parameters from a sequence of linear polarization measurements; the second method was based on direct transmission measurements employing the kirigami modulators for TCD spectroscopy of biomaterials.

3.5.1 THz-TDS Measurements Set-up

Terahertz time-domain spectroscopy (THz-TDS) was used to measure the optical responses of the chiral kirigami modulators. A Ti:Sapphire regenerative amplifier (RegA 9050, Coherent) with a center wavelength of 800 nm, a pulse duration of ~80 fs and a repetition rate of 250 kHz excites a THz photoconductive (PC) emitter (Tera-SED10, Laser Quantum) and the generated THz rays are collimated by an off-axis parabolic mirror onto the kirigami structures at normal incidence. The spot size of the THz beam is controlled by an iris diaphragm to a diameter of ~2 cm to ensure we measure only THz waves passing through the kirigami modulator. The transmitted beam is focused by another set of parabolic mirrors and detected by a 1 mm thick (110)-oriented ZnTe crystal with the method of electro-optic (EO) sampling (*55*).

The following method utilizing two linear polarizers was used to determine the orientation and ellipticity of arbitrarily polarized THz waves (*38*). Two THz wire grid polarizers (G50 × 20-

L, Microtech Instruments, Inc.) with an extinction ratio of 10^3-10^4 in the spectral range 0.1-3 THz were used in the configuration shown in **Figure 3-9A**. The THz fields generated by the PC emitter were measured to have a high degree of linear polarization with an ellipticity angle below 0.3° (shown as the dash-dot lines in **Figure 3-11** to **Figure 3-13**), which is negligible compared to the ellipticity induced by the chiral kirigami modulator; we confirmed that use of a linear polarizer immediately after the emitter made no further improvement in linearity. The emitter was fixed at an orientation such that the generated THz polarization was horizontal to the optical table (defined here as the *x* axis). The first polarizer (P1) was placed in front of the ZnTe crystal and its transmission direction (perpendicular to the wire grid orientation) was fixed vertical to the optical table (defined as the *y* axis). The ZnTe crystal and the sampling pulses were also oriented to give the maximum electro-optic sensitivity along *y* direction. The second polarizer (P2) was placed between the sample and the first polarizer and was rotated to different orientations to determine the complete polarization state of the transmitted field.

When the P2 transmission axis is along the *y* direction (defined as 0°), it is aligned with P1 and the y-component of the transmitted waves through sample $E_y(t)$ is measured. The x-component $E_x(t)$ is measured by rotating the orientation of P2 to +45° and -45° and calculated by the subtraction of the two. Since any arbitrary electric field can be decomposed into two perpendicular components, polarization states such as ellipticity and polarization rotation angle can be fully determined with three measurements. The electric field from the PC emitter without samples was also measured using the same method for calculating the reference transmission coefficients and labeled as "emitter" in **Figure 3-11** to **Figure 3-13**.

3.5.2 Definition of sample mounting orientations and abbreviations for sample configurations

Since our kirigami pattern does not have C4 symmetry, measurements must be performed for two perpendicular polarizations, i.e. horizontally and vertically polarized THz waves, incident on the kirigami to fully characterize the kirigami sheet's in-plane optical properties, especially for circular dichroism. This was accomplished by rotating the kirigami sheet by 90° instead of rotating the THz emitter, which would have required elaborate rotations of two polarizers as well as the ZnTe crystal and the sampling beam. The kirigami modulator was attached to a rotation mount (RSP1, Thorlabs), so the transmitted waves can be measured in both horizontal and vertical orientations (simple rotation by 90°). Here, the horizontal and vertical mounting orientations are defined as follows: (1) horizontal - stretching direction is along with x direction as indicated in **Figure 3-9B**, (2) vertical - stretching direction is along with y direction in **Figure 3-9C**.

There are four possible configurations for the measurements: the kirigami modulator may be designed for either right- or left-handedness, and the modulators may be mounted horizontally or vertically relative to the input linear polarization. The abbreviation used in this chapter is as follows: "HL" for horizontally mounted left-handed kirigami modulator, "HR" for horizontally right-handed, "VL" for vertically left-handed, and "VR" for vertically right-handed.

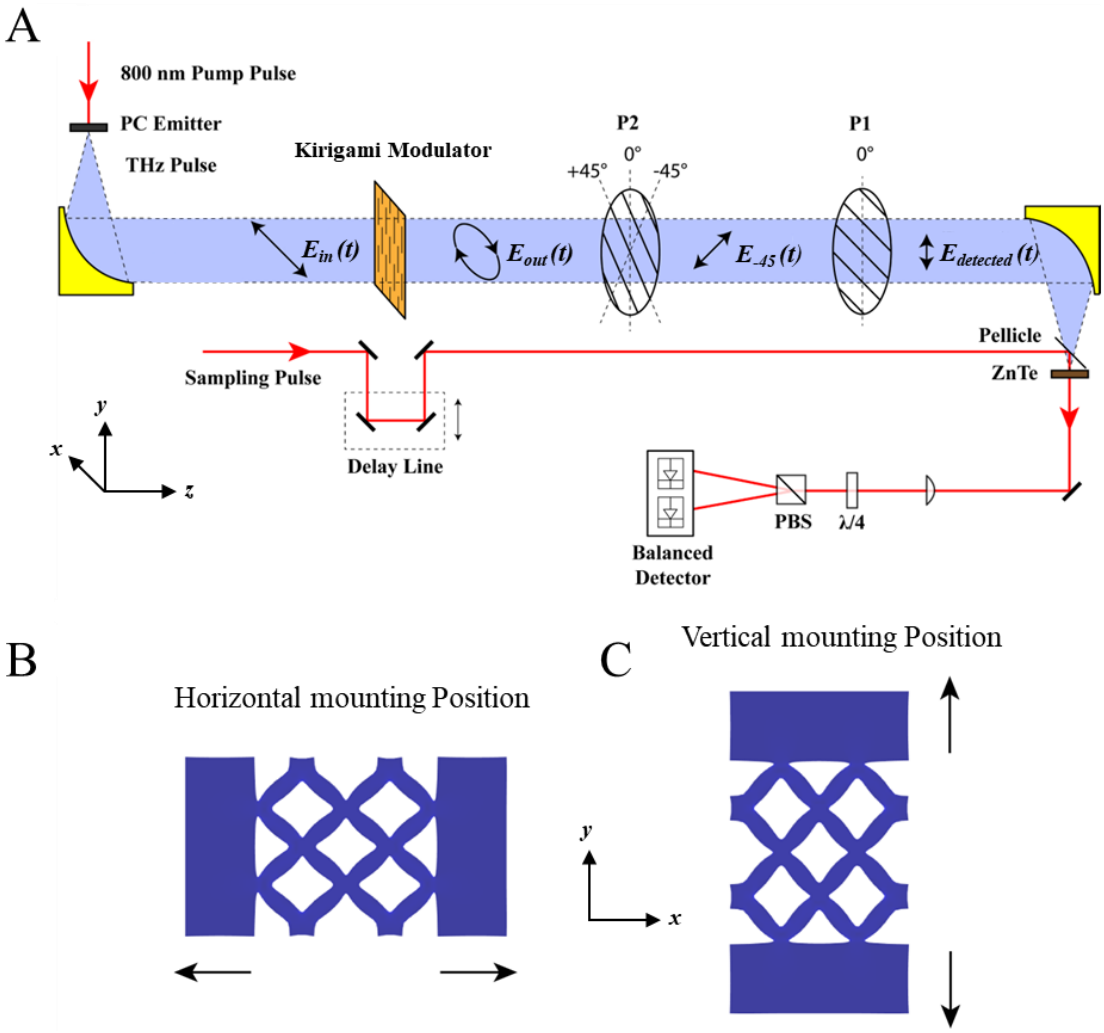

Figure 3-9 Schematics of the experimental setup and sample mounting positions for THz-TDS polarimetry measurement. (A) Schematic of THz-TDS polarimetry measurement setup. The orientation of THz polarizer P1 is fixed at 0° to allow vertically polarized waves to transmit. The orientation of polarizer P2 is rotated to +45°, -45° or 0° for three polarization-selective measurements. This figure presents the orientation of P2 at -45° for example. (B) and (C) show the definitions of horizontal (H) and vertical (V) mounting positions. The thick black arrows indicate the stretching directions actuated by the piezo-controller horizontally for (B) and vertically for (C). Reproduced from ref.(*1*).

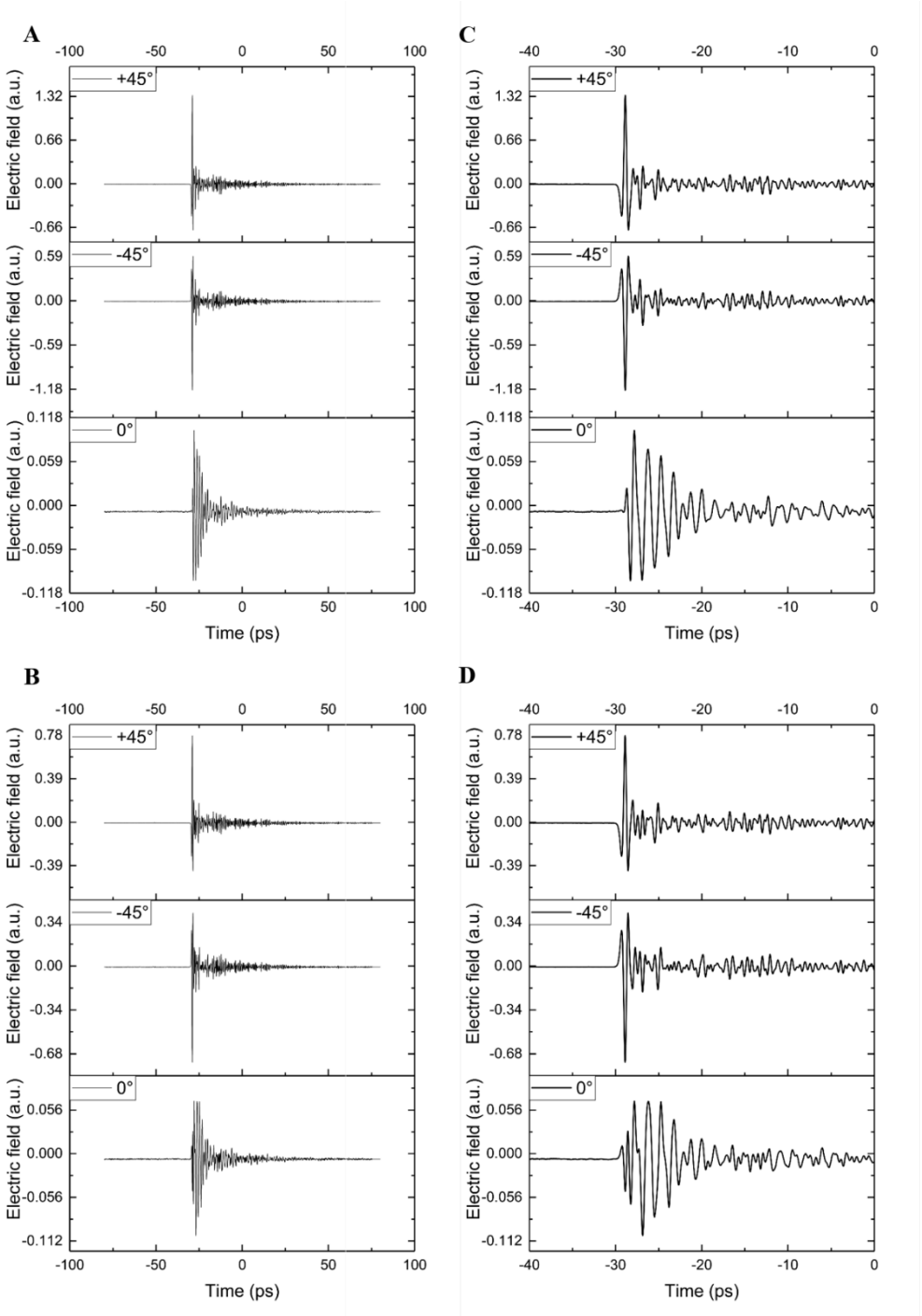

Figure 3-10 An example of raw THz-TDS data for three polarization measurements of a left-handed (L-) kirigami sample with 30° slant angle (φ = 30°) and stretched with ε = 22.5%. (A) Transmitted electric fields of horizontally and (B) vertically mounted sample over the whole scan range. (C) and (D) are zoomed views on the main peaks (near zero time delay) of (A) and (B), respectively. Reproduced from ref.(*1*).

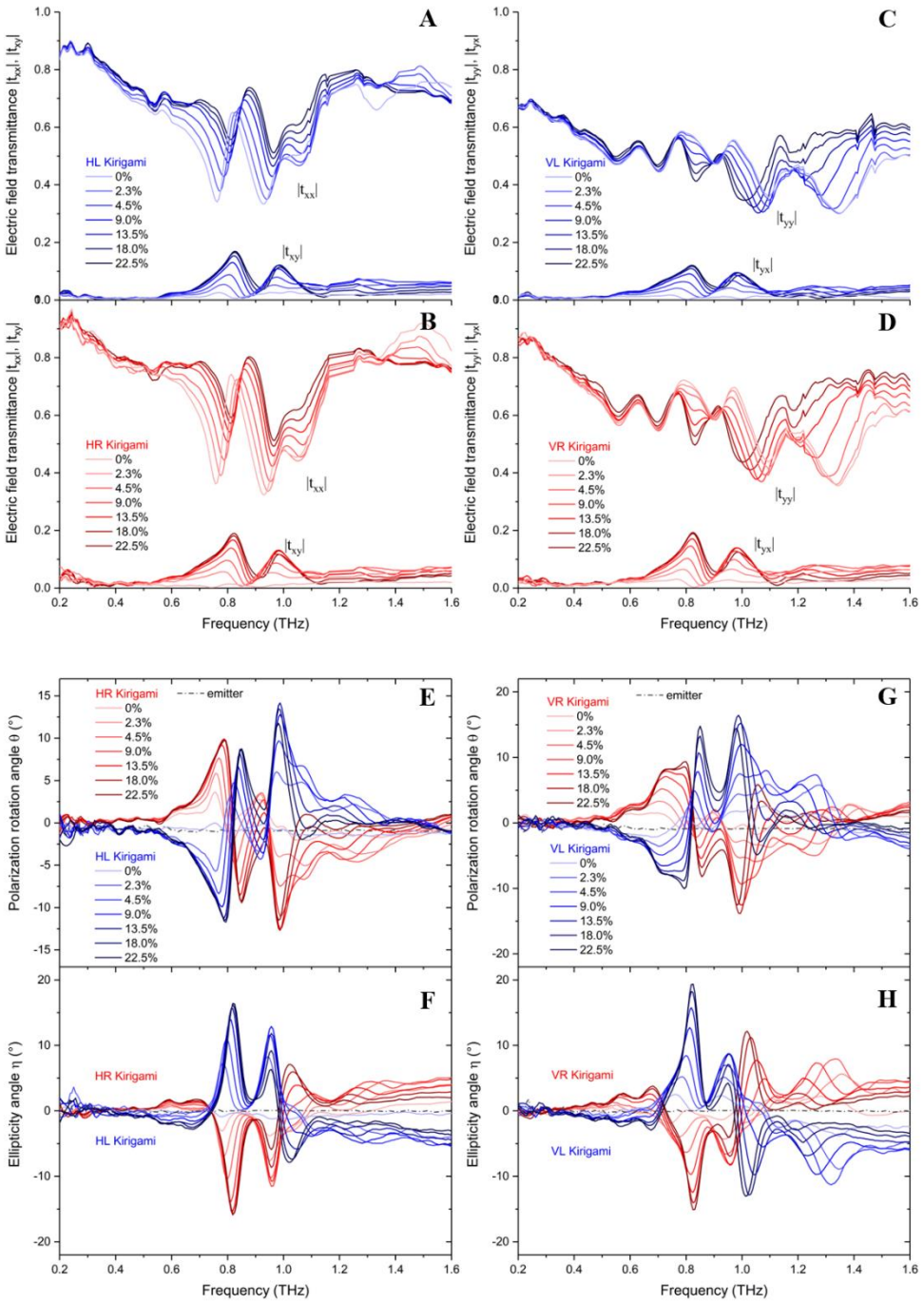

Figure 3-11 Experimental data for kirigami samples with wire slant angle of 45°. (A) – (D) the magnitudes of four transmittance coefficients. (E) polarization rotation angle and (F) ellipticity angle induced by the samples mounted horizontally (H). (G) polarization rotation angle and (H) ellipticity angle induced by the samples mounted vertically (V). Blue and red curves are for left-handed (L) and right-handed (R) samples respectively. The strains applied are given in the legends and the same for all the subfigures. Reproduced from ref.(*1*).

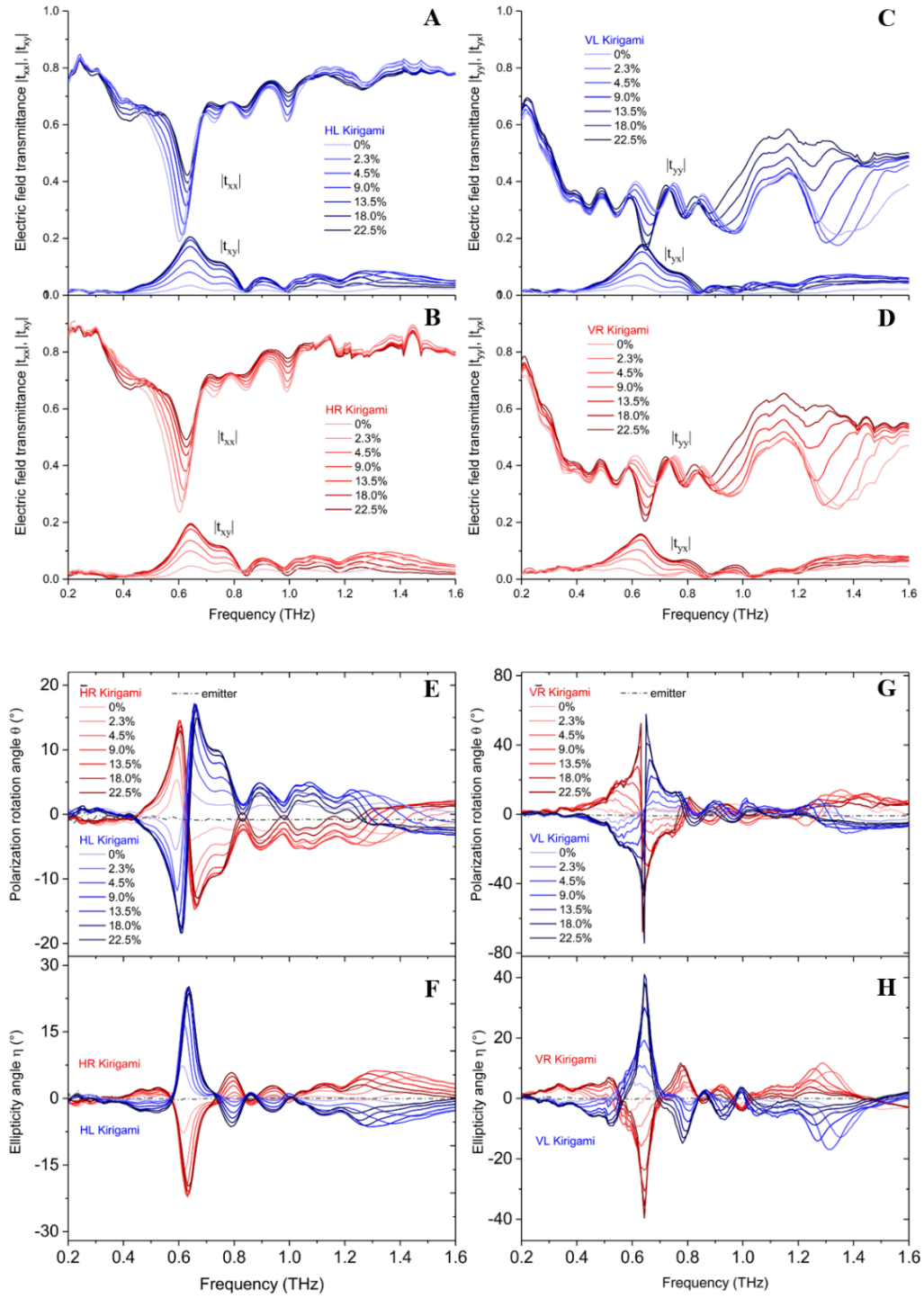

Figure 3-12 Experimental data for kirigami samples with wire slant angle of 30°. (A) – (D) the magnitudes of four transmittance coefficients. (E) polarization rotation angle and (F) ellipticity angle induced by the samples mounted horizontally (H). (G) polarization rotation angle and (H) ellipticity angle induced by the samples mounted vertically (V). Blue and red curves are for left-handed (L) and right-handed (R) samples respectively. The strains applied are given in the legends and the same for all the subfigures. Reproduced from ref.(*1*).

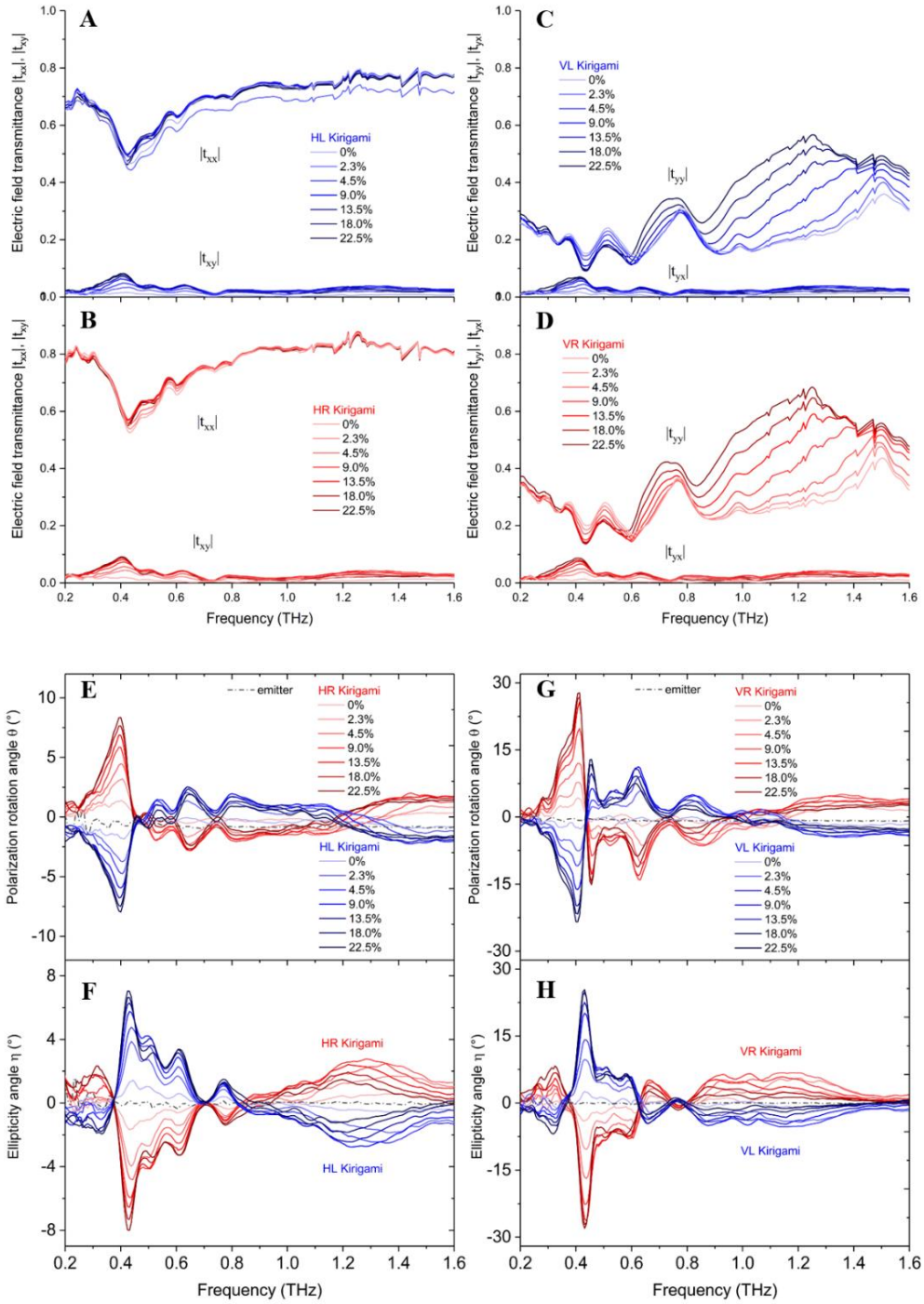

Figure 3-13 Experimental data for kirigami samples with wire slanted angle of 15°. (A) – (D) the magnitudes of four transmittance coefficients. (E) polarization rotation angle and (F) ellipticity angle induced by the samples mounted horizontally (H). (G) polarization rotation angle and (H) ellipticity angle induced by the samples mounted vertically (V). Blue and red curves are for left-handed (L) and right-handed (R) samples respectively. The strains applied are given in the legends and the same for all the subfigures. Reproduced from ref.(*1*).

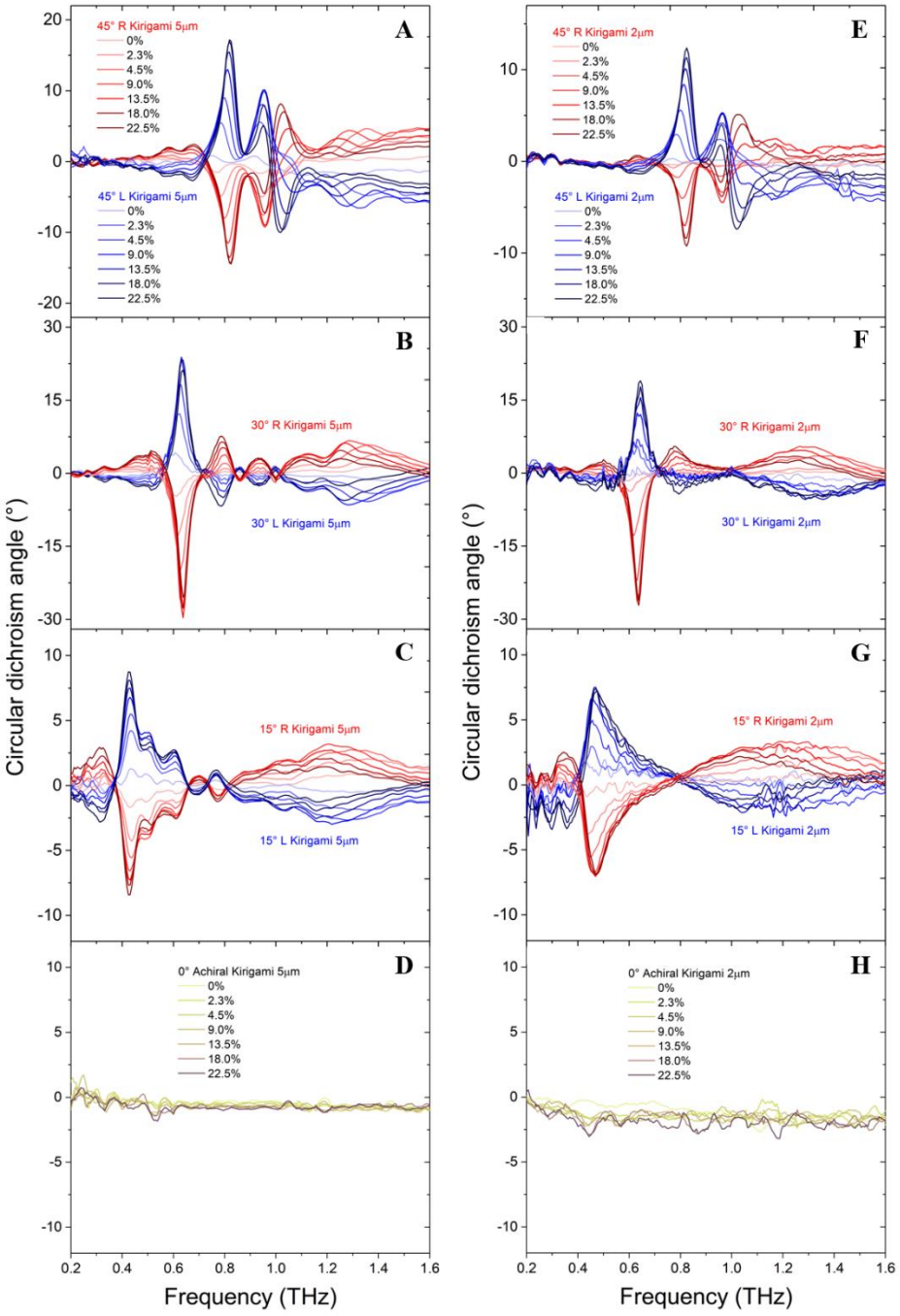

Figure 3-14 Comparison of circular dichroism spectra of kirigami samples with different gold wire widths and spacings. The left (right) column corresponds to samples of 5 μm (2 μm) wire width and 5 μm (2 μm) spacing. The four rows correspond to samples with wire slant angles of 45° (A, E), 30° (B, F), 15° (C, G) and 0° (D, H), respectively. Blue and red curves are for left-handed (L) and right-handed (R) samples respectively and yellow curves are for achiral samples. Reproduced from ref.(*1*).

3.5.3 Calculations of Transmittance, Polarization state and TCD

As mentioned above, the *x*-component of the electric field can be calculated by

$$E_x(t) = E_{+45^\circ}(t) - E_{-45^\circ}(t) \tag{1}$$

where $E_{+45^\circ}(t)$ and $E_{-45^\circ}(t)$ are the time-domain electric field measurements when the transmission orientation of polarizer P2 are at +45° and -45° relative to that of the polarizer P1, respectively.

The electric field signals are measured in the time domain and the complex frequency-domain electric field spectra are obtained using fast Fourier transform (FFT)

$$\begin{aligned} \tilde{E}_x &= \tilde{E}_x(\omega) = FFT\{E_x(t)\} \\ \tilde{E}_y &= \tilde{E}_y(\omega) = FFT\{E_y(t)\} \end{aligned} \tag{2}$$

The Jones transfer matrix of a sample can be defined as

$$T = \begin{pmatrix} t_{xx} & t_{yx} \\ t_{xy} & t_{yy} \end{pmatrix} \tag{3}$$

where the first subscript letter indicates the incident polarization direction and the second subscript indicates the output direction for detection; the electric field vector of the transmitted THz wave through the sample $\tilde{E}_s$ is related to the incident electric field $\tilde{E}_{in}$ by

$$\tilde{E}_s = T\tilde{E}_{in} \tag{4}$$

The electric field $\tilde{E}_{in}$ incident on the sample is the reference electric field generated by the PC emitter measured without a sample $\tilde{E}_{ref}$ and in our measurement, it is always along the *x* direction. When the sample is mounted horizontally, electric field and transmission coefficients have relation as follow:

$$\begin{pmatrix} \tilde{E}_{sx}^h \\ \tilde{E}_{sy}^h \end{pmatrix} = \begin{pmatrix} t_{xx} & t_{yx} \\ t_{xy} & t_{yy} \end{pmatrix} \begin{pmatrix} \tilde{E}_{ref} \\ 0 \end{pmatrix} \tag{5}$$

Here, superscripts indicate the abbreviation of mounting orientation. Also, the two transmission coefficients of the sample at horizontal position can be calculated by

$$t_{xx} = \tilde{E}_{sx}^{h} \,/\, \tilde{E}_{ref}$$
$$t_{xy} = \tilde{E}_{sy}^{h} \,/\, \tilde{E}_{ref} \tag{6}$$

After rotating the sample by 90° which is defined as vertical orientation, the measured transmitted signals are related to the reference signal as

$$\tilde{E}_{s}^{v} = R(90°)TR(-90°)\tilde{E}_{ref} \tag{7}$$

where $R(\theta)$ is the rotation matrix with rotation angle θ

$$R(\theta) = \begin{pmatrix} cos(\theta) & -sin(\theta) \\ sin(\theta) & cos(\theta) \end{pmatrix} \tag{8}$$

Therefore, the measured transmitted signals of the sample for vertical orientation are

$$\begin{pmatrix} \tilde{E}_{sx}^{v} \\ \tilde{E}_{sy}^{v} \end{pmatrix} = \begin{pmatrix} 0 & -1 \\ 1 & 0 \end{pmatrix} \begin{pmatrix} t_{xx} & t_{yx} \\ t_{xy} & t_{yy} \end{pmatrix} \begin{pmatrix} 0 & 1 \\ -1 & 0 \end{pmatrix} \begin{pmatrix} \tilde{E}_{ref} \\ 0 \end{pmatrix}$$
$$= \begin{pmatrix} t_{yy} & -t_{xy} \\ -t_{yx} & t_{xx} \end{pmatrix} \begin{pmatrix} \tilde{E}_{ref} \\ 0 \end{pmatrix} \tag{9}$$

and the two transmission coefficients of the sample at vertical orientation can be calculated by

$$t_{yy} = \tilde{E}_{sx}^{v} \,/\, \tilde{E}_{ref}$$
$$t_{yx} = -\,\tilde{E}_{sy}^{v} \,/\, \tilde{E}_{ref} \tag{10}$$

Since the polarization of the incident THz beam is linear and horizontal, the sample-induced polarization rotation angle, θ, and ellipticity angle, η (*56*), can be calculated directly by the measured THz spectra of $\tilde{E}_s = \begin{pmatrix} \tilde{E}_x \\ \tilde{E}_y \end{pmatrix}$ using Stokes parameters (*56*), and the same equations can be applied for both the horizontal and vertical orientations of mounting. The four Stokes parameters are defined as

$$S_0 = \tilde{E}_x \tilde{E}_x^* + \tilde{E}_y \tilde{E}_y^*$$
$$S_1 = \tilde{E}_x \tilde{E}_x^* - \tilde{E}_y \tilde{E}_y^*$$
$$S_2 = \tilde{E}_x \tilde{E}_y^* + \tilde{E}_y \tilde{E}_x^*$$
$$S_3 = i(\tilde{E}_x \tilde{E}_y^* - \tilde{E}_y \tilde{E}_x^*) \tag{11}$$

Since THz-TDS measures the electric field directly, three measurements (one for $\tilde{E}_y$and two for $\tilde{E}_x$) determine the four Stokes parameters and thus the polarization state.

The polarization rotation angle θ relative to the horizontal direction and the ellipticity η can be calculated using Stokes parameters as follow:

$$\theta = \frac{1}{2} tan^{-1}\left(\frac{S_2}{S_1}\right), \qquad -\frac{\pi}{2} \le \theta \le \frac{\pi}{2}$$
$$\eta = \frac{1}{2} sin^{-1}\left(\frac{S_3}{S_0}\right), \qquad -\frac{\pi}{4} \le \eta \le \frac{\pi}{4} \tag{12}$$

Additional care should be taken for the rotation angle, θ, because mathematically the range of the inverse tangent function $tan^{-1}(x)$ is $\left[-\frac{\pi}{2}, \frac{\pi}{2}\right]$ and correspondingly the range of θ would be $\left[-\frac{\pi}{4}, \frac{\pi}{4}\right]$. In optics, however, the rotation angle θ is within the range of $\left[-\frac{\pi}{2}, \frac{\pi}{2}\right]$. This can be easily illustrated via the Poincaré sphere in which 2θ covers a whole circle, *i.e.* from $-\pi$ to π. The three perpendicular axes on the Poincaré sphere can be represented by the three Stokes parameters S_1, S_2 and S_3, so the following conditions are used to convert the mathematical inverse tangent function given by the numerical computing software (MATLAB for this chapter) to the actual optical rotation angle θ

$$\text{if } S_1 \ge 0: \quad \theta = \frac{1}{2} tan^{-1}\left(\frac{S_2}{S_1}\right), \qquad -\frac{\pi}{4} \le \theta \le \frac{\pi}{4}$$
$$if\ S_1 < 0 \text{ and } S_2 \ge 0: \theta = \frac{1}{2} tan^{-1}\left(\frac{S_2}{S_1}\right) + \frac{\pi}{2}, \qquad \frac{\pi}{4} < \theta \le \frac{\pi}{2}$$
$$if\ S_1 < 0\ and\ S_2 < 0: \theta = \frac{1}{2} tan^{-1}\left(\frac{S_2}{S_1}\right) - \frac{\pi}{2}, \qquad -\frac{\pi}{2} \le \theta < -\frac{\pi}{4} \tag{13}$$

Alternatively, it can be directly calculated by using the four-quadrant inverse tangent function, especially for MATLAB.

$$\theta = \frac{1}{2} atan2(S_2, S_1), \qquad -\frac{\pi}{2} \le \theta \le \frac{\pi}{2} \tag{14}$$

The transmitted electric field through a kirigami sample for a circularly polarized incident beam can be inferred using the Jones matrix elements measured from linearly polarized incident fields. For a normalized right circularly polarized (RCP) incident beam (*57*)

$$\tilde{E}_{RCP}^{in} = \frac{1}{\sqrt{2}}\begin{pmatrix}1\\ i\end{pmatrix} \tag{15}$$

the electric field of the transmitted wave is

$$\tilde{E}_{RCP}^{out} = \begin{pmatrix}t_{xx} & t_{yx}\\ t_{xy} & t_{yy}\end{pmatrix}\frac{1}{\sqrt{2}}\begin{pmatrix}1\\ i\end{pmatrix} = \frac{1}{\sqrt{2}}\begin{pmatrix}t_{xx}+it_{yx}\\ t_{xy}+it_{yy}\end{pmatrix} \tag{16}$$

and the magnitude of this complex electric field vector is

$$E_R = \frac{1}{\sqrt{2}}\sqrt{\left|t_{xx}+it_{yx}\right|^2+\left|t_{xy}+it_{yy}\right|^2} \tag{17}$$

where $|\ |$ is the absolute value of a complex number.

Similarly, for a normalized left circularly polarized (LCP) incident beam (*57*)

$$\tilde{E}_{LCP}^{in} = \frac{1}{\sqrt{2}}\begin{pmatrix}1\\ -i\end{pmatrix} \tag{18}$$

the electric field of the corresponding transmitted wave is

$$\tilde{E}_{LCP}^{out} = \begin{pmatrix}t_{xx} & t_{yx}\\ t_{xy} & t_{yy}\end{pmatrix}\frac{1}{\sqrt{2}}\begin{pmatrix}1\\ -i\end{pmatrix} = \frac{1}{\sqrt{2}}\begin{pmatrix}t_{xx}-it_{yx}\\ t_{xy}-it_{yy}\end{pmatrix} \tag{19}$$

and the magnitude of this complex electric field vector is

$$E_L = \frac{1}{\sqrt{2}}\sqrt{\left|t_{xx}-it_{yx}\right|^2+\left|t_{xy}-it_{yy}\right|^2} \tag{20}$$

The terahertz circular dichroism (TCD) is a commonly used quantity for characterizing the optical activity of chiral materials (*58*). It is related to the relative transmission (or absorption) difference between RCP and LCP incident waves, and can be defined and quantified by (*58*)

$$TCD\ = tan^{-1}\left(\frac{E_R-E_L}{E_R+E_L}\right) \tag{21}$$

where E_R and E_L are the magnitudes of the transmitted waves of RCP and LCP incident beams given by Eq. (17) and Eq. (20), respectively.

3.5.4 An example of raw THz-TDS data for Kirigami sheets

As an example of the raw data measured directly from THz-TDS with the two-linear polarization setup, **Figure 3-10** shows the three time-domain THz electric fields (i.e. with the polarizer P2 rotated to +45°, -45° or 0° position) of a horizontally mounted left-handed (*HL*) kirigami sample with gold herringbone pattern at φ = 30° and stretched with ε = 22.5%. **Figure 3-10B** are the electric fields for the same sample under the same measurement conditions but rotated to vertical (*VL*). **Figure 3-10C** and **Figure 3-10D** show zoomed views near zero time delay, and the signals of the 0° component and the appearance of multi-cycle waves compared to single-cycle input pulse (especially for the 0° component) are clear evidences of polarization rotation and THz resonances of chiral kirigami structures. These raw data were then processed using the equations presented in the previous section to calculate the electric field transmittances, polarization angles and circular dichroism.

3.5.5 Experimental data of Transmittance, Polarization state and TCD of single Kirigami modulator

The detailed data for kirigami modulator with three different slant angles φ are presented in **Figure 3-11** to **Figure 3-14**. These include the spectra of the magnitudes of the transmission coefficients (t_{xx}, t_{xy}, t_{yx}, t_{yy}), the polarization rotation (θ) and ellipticity angles (η) for the different slant angles (φ) for both horizontal and vertical mounts, and the spectra of the resulting circular dichroism angles. In addition, kirigami structures with narrower gold wire widths and spacings (2 μm wire width and 2 μm spacing) but otherwise the same design parameters are also measured to

explore the origin of resonance. Unless stated otherwise, all other data were measured with samples with gold strips with 5 μm wire width and 5 μm spacing.

The largest strain applied in these measurements was $\varepsilon = 22.5\%$. This value was chosen for the optimum performance as well as maintaining the function as modulators for the kirigami samples. It was measured that beyond this strain the polarization rotation and ellipticity saturated. With a much larger strain, the signal actually decreased because the Au strip surfaces became parallel to the THz beam propagation direction and the effective interaction area became smaller. In addition, a very large strain would deform the sample out of the elastic range and deteriorate the function of these samples as modulators.

3.5.6 Measurements and Modeling of Kirigami 3D geometries

The 3D topography of the kirigami sheets under various strains were measured using a laser confocal microscope (OLS 4000 LEXT, Olympus). The kirigami geometries were reconstructed using 3D graphic software packages (Rhino 5, Robert McNeel & Associates and 3D Max 2017, Autodesk) based on the experimentally acquired images from the confocal microscopy. Three projected images captured at different view angles were used to clearly define and reconstruct the radius, angles, shapes and boundaries. Two 3D structures of right-handed (*R*) kirigami sheets with 45° slanted Au strips were made as shown in **Figure 3-7A** and **Figure 3-7B**. Kirigami sheets were flipped to make reversed handedness, left-handed (*L*) structures. In addition, an achiral structure with a 0° wire slanted angle was also modeled using the same procedure as shown in **Figure 3-7C**.

3.5.7 Polarization Rotation, Ellipticity and TCD Results of Kirigami Modulator

The kirigami sheets were mounted on an optical holder and finely controllable stress was applied with a programmable piezoactuator with a precision of 100 nm (ε = 0.001%) (**Figure 3-8a**). The handedness of each kirigami sheet is pre-determined by stress concentrators to ensure homogeneous chirality over the structure (**Figure 3-3**). As expected θ and η increased with strain and kirigami structures with left-handed and right-handed herringbone patterns exhibit THz responses that are nearly identical but with opposite signs (**Figure 3-8c-h**). The inclination angle (φ) of the herringbone patterns (insets of **Figure 3-8d, f, h**) determined the position of the main resonance peaks, which were observed at 0.41 THz for φ = 15°, 0.62 THz for φ = 30° and 0.81 THz for φ = 45°. The maximum values of θ and η reached as high as 80° and 40°, respectively, were obtained for herringbone patterns with φ of 30°. This maximum ellipticity value is almost close to that of quarter-waveplate. Note that the magnitudes of θ and η can be different depending on the in-plane rotation angles due to birefringence, which was taken into account in the TCD spectra (**Figure 3-11 to Figure 3-14**). As a control, an achiral pattern with horizontally aligned (φ = 0°) Au strips was tested, and showed near-zero values of θ and η regardless of the strain, confirming the critical role of the double-pattern design for the strong optical activity **(Figure 3-14**). Polarization modulations with nearly identical values of θ and η were obtained for 1000 cycles with ε between 0 % and 22.5 % (**Figure 3-15**).

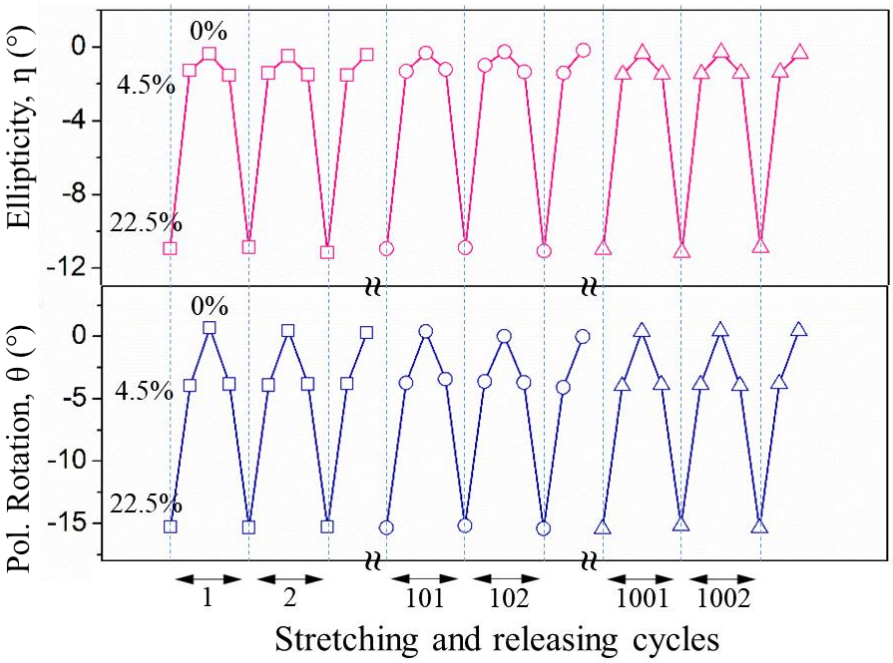

Figure 3-15 Results of polarization rotation and ellipticity angle of stretching and releasing cycles. Cycling properties of polarization rotation and ellipticity angle. Both of θ and η values are taken at 0.84 THz using kirigami modulator having φ of 45°. Not only for mechanically but optically it maintains its values of polarization rotation and ellipticity angle even over 1000 cycles. Reproduced from ref.(*1*).

3.6 Understanding Physical Meaning of Resonance Frequency

The effect of the microscale cut pattern on the optical performance of the kirigami polarization modulators was tested for variable size of the unit cell for a constant inclination φ = 30°. As L_{cut} becomes larger, the main TCD peak shifts to the red (**Figure 3-16a**,**b**), indicating that its spectral position is determined by the longitudinal plasmonic resonances of the Au strips. Confirming this conclusion, TCD spectra of kirigami modulators with Au strips having same length and φ but narrower width display the same position of resonance peak and similar overall shape (**Figure 3-14**). The resonance wavelength of the kirigami sheets with herringbone patterns can be heuristically assessed as an *LC* circuit with the resonance frequency of $f_r = (2\pi\sqrt{L_{Au}C_{Au}})^{-1}$(*59*). The inductance L_{Au} and capacitance C_{Au} of Au strips scale linearly with its length, l (**Figure 3-16**), and therefore f_r becomes inversely proportional to l (**Figure 3-16d**). Alternatively, the metal strips can also be approximated as Hertzian dipoles bent and tilted in 3D space, $l \sim \lambda_r/4 = c/4f_r$, where c and λ_r are the speed of light and resonance wavelength. This equation can be used to provide an approximate guide of the design of herringbone patterns for different applications.

3.6.1 Circuit model for calculating resonance frequency

The inductance of *n* parallel conductors with identical dimensions can be calculated as

$$L = \sum_{i=1}^{n} L_i + \sum_{i=1}^{n} \sum_{j=1, j\neq i}^{n} M_{i,j} \quad (22)$$

where L_i is the self-inductance and $M_{i,j}$ is the mutual inductance (*60*). Here we assume that each conductor carries the same current and the current is uniformly distributed over the entire cross

section. To obtain a simple expression, we convert *n* identical parallel conductors into one large single equivalent current sheet having total width of $\rho = nw + (n-1)s$, where *s*, *w*, *l* are edge-to-edge spacing, width and length of the strips, respectively as described in reference (*60*). The result of sheet approximation is

$$L \approx \frac{\mu_0 n^2 l}{2\pi}\left[\ln\left(\frac{2}{\rho}\right) + 0.5 + \frac{\rho}{3} - \frac{\rho^2}{24}\right] \quad (23)$$

where μ_0 is the permeability of free space and variable ρ is the ratio of the width of the equivalent current sheet to its length. In addition, the self-capacitance of the Au strips is a combination of the capacitance between the gap capacitance in air and substrate. The total capacitance of the parallel conductors is given below:

$$C = l(n-1)\left(\frac{\varepsilon_0}{2}\frac{K(k')}{K(k)} + 2\varepsilon_0\varepsilon_r\frac{t}{s}\right) \quad and \quad k' = \sqrt{1-k^2} \quad (24)$$

where ε_0 is the permittivity of free space and ε_r is the relative permittivity. *K(k)* represents the elliptical integral of first order to calculate the effect of the fringing field. The modulus *k* defined as $k = cos\left(\frac{\pi}{2}\frac{w}{s+2}\right)$ is determined by the periodic geometry (*61*). The scaling of the optical response of parallel metal strips can be obtained by modeling the structure as an *LC* circuit with the resonance frequency of $f_r = (2\pi\sqrt{LC})^{-1}$(*59*). Roughly, inductance *L* and capacitance *C* scale linearly with the length of Au strips, *l*, and therefore f_r become inversely proportional to *l* as shown in **Figure 3-16d** in the main text.

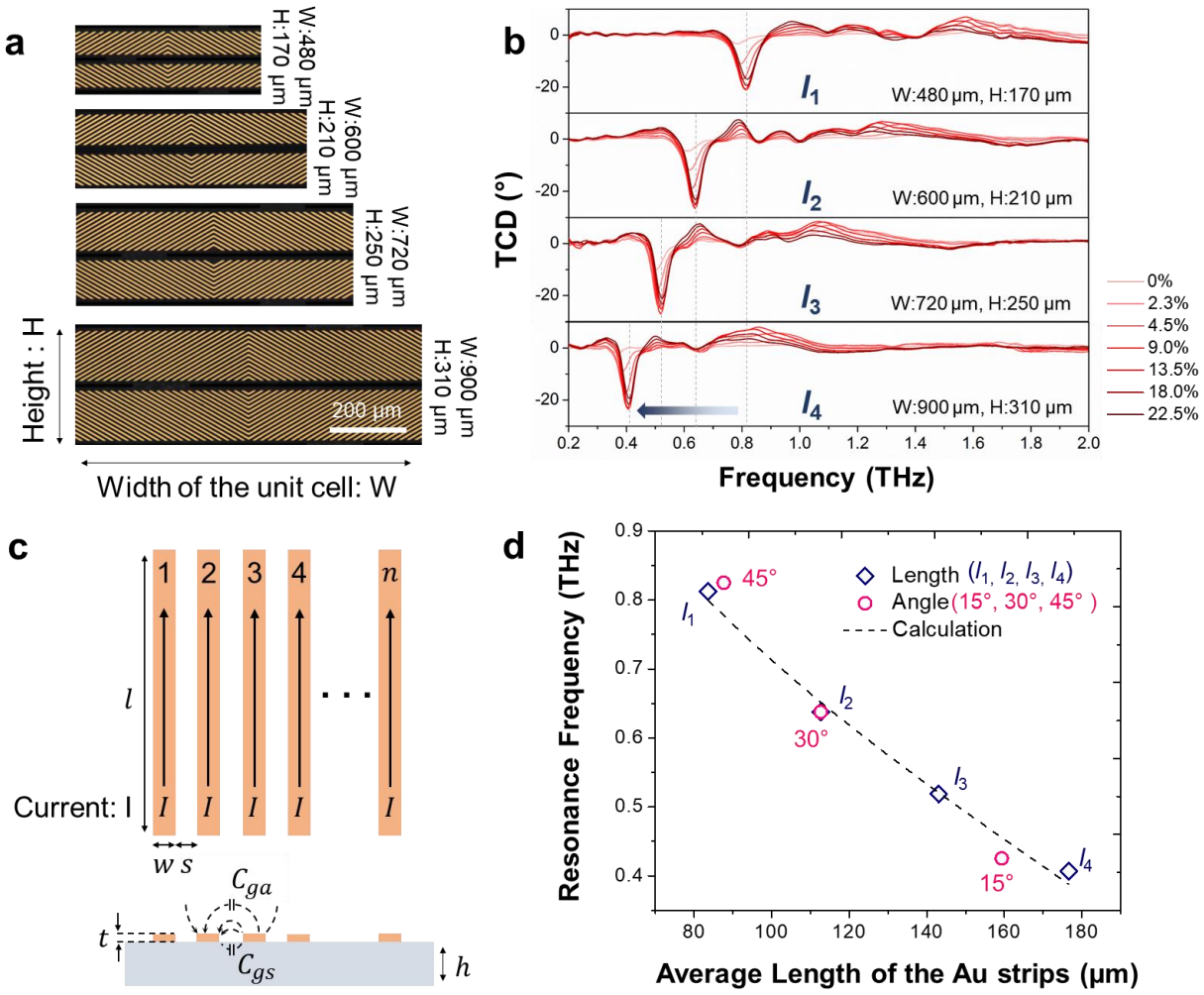

Figure 3-16 Understanding physical meaning of resonance frequency. a, Optical microscope image of various length of unit cell. All samples have φ of 30°. b, Result of measured TCD from R- kirigami modulator with various length of unit cell. c, Upper figure shows parallel conducting strips to obtain total inductance of this configuration. Lower figure is for calculating capacitance of array of strips. d, Relation between resonance frequency and average length (l) of the Au strips. Scale bar in a is 200 μm. Reproduced from ref.(*1*).

3.7 Electromagnetic Simulations of Kirigami Modulators

TCD spectra of the kirigami optical components can be predicted with *ab ovo* electrodynamic simulations. Since the parylene substrate is very thin and shows low loss tangent over the THz range without chiroptical activity, we omitted it from the calculation model. Computed TCD spectra (**Figure 3-17a**) matched well the experimental data with respect to the signs of the polarization rotation angle, peak positions, relative peak widths and amplitudes (**Figure 3-14a**). Calculated time-averaged current norm distributions generated on the Au strips for the incident of the circularly polarized beam point to the origin of the plasmonic states responsible for individual peaks (**Figure 3-17b-d)** (*38*). At the off-resonant frequency of 0.57 THz, the induced currents are low for both co- and cross-circularly polarized beam and most of the Au strips are optically inactive (**Figure 3-17b)**. At the resonant frequency of 0.82 THz, however, the incident beam induces strong currents in the Au strips. Simultaneously, the currents excited by the right-handed circularly polarized beam significantly exceed those for left circularly polarized beam (**Figure 3-17c** and **Figure 3-17d**). As a result, the transmittance of the left circularly polarized beam is larger than that of the right circularly polarized beam due to the induced current, which is consistent with the sign of the peaks in **Figure 3-17a** and **Figure 3-14a**. On the other hand, we can find strong secondary peaks around 1.05 THz and 1.15 THz and these could come from the electromagnetic coupling between adjacent strips (*38*, *59*).

3.8.1 TCD Simulation and Surface Current Norm Distributions

TCD simulations and surface current norm distributions of illuminated kirigami modulators were numerically investigated with finite element simulation software (COMSOL Multiphysics 5.2a, COMSOL Inc.) using the reconstructed 3D models for the shape. Periodic boundary conditions were applied to the single unit cell of each model to simplify the simulation and to reduce the required computational power. It should be noted that this could lead to some simulation errors due to the infinite unit cells assumed by periodic boundary conditions. In the experiment, of course, there are a finite number of unit cells defined by diameter of the THz beam; this could be one of the reasons that the magnitudes of the simulation were slightly larger than the experimental data. Other possible reasons for this slight difference between experiment and simulation can be the frequency resolution limit of the experimental setup (*38*) and the errors generated during the modeling process and inherent limitations of COMSOL solvers. Apart from this slight difference, the simulated results matched well with the experimental data for the circular dichroism signs, peak positions, peak width and magnitudes.

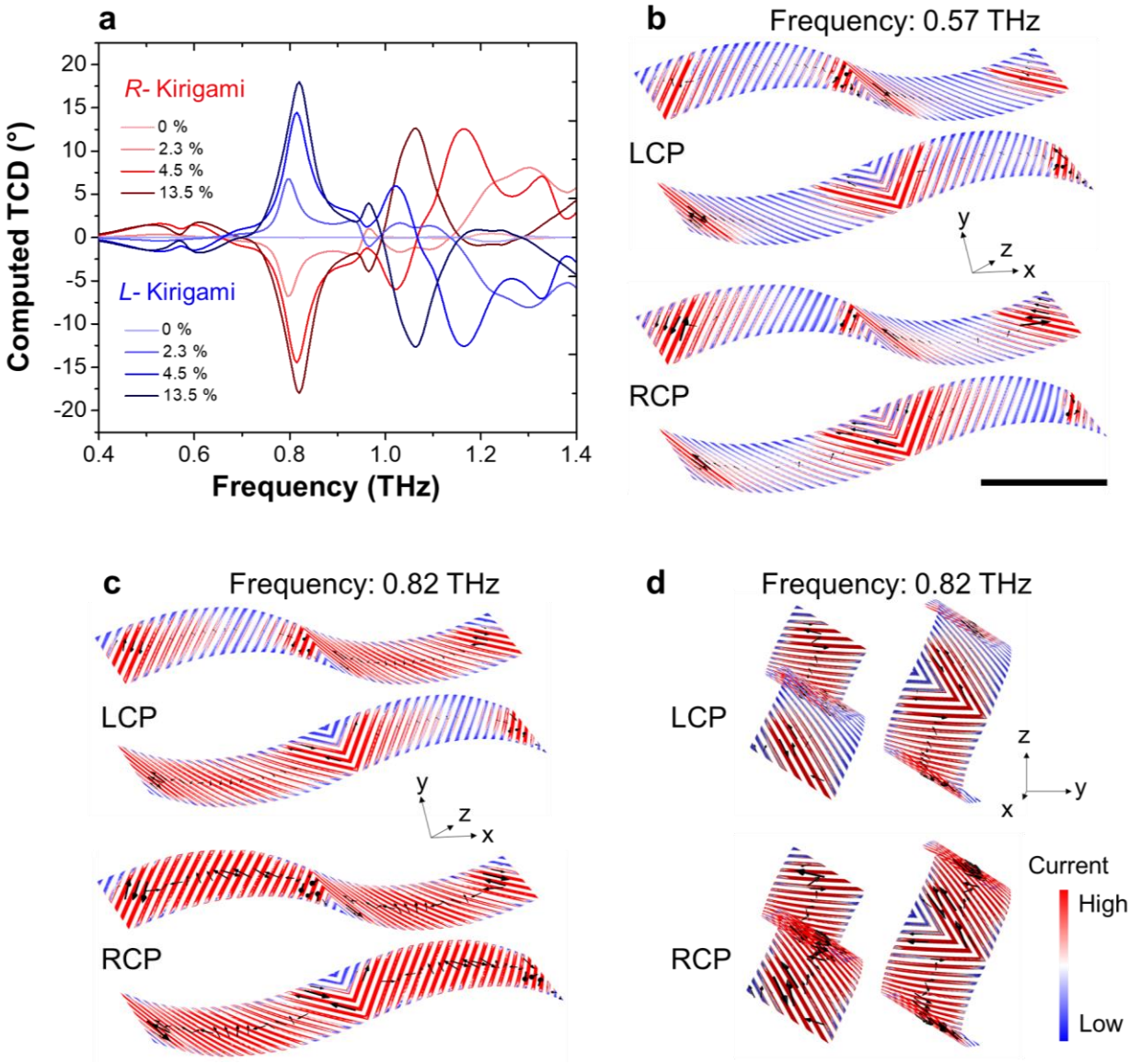

Figure 3-17 Computed terahertz circular dichroism and time-averaged current norm distributions on kirigami modulator (φ=45°). a, Computed TCD spectrum for 4 deformation states. **b** and **c**, Tilted view of current norm distributions of R- kirigami at the frequency of 0.57 THz, 0.82THz, respectively. **d,** Side view of current norm distributions of R- kirigami at 0.82 THz. Black arrows indicate the current directions. Here, right and left circularly polarized beam denoted as RCP and LCP, respectively. A scale bar is 200 μm. Reproduced from ref.(*1*).

3.8 Terahertz Circular Dichroism Spectroscopy Enabled by Kirigami Modulators

The unique combination of high ellipticity and tunability of kirigami optics makes possible its utilization for modulating THz light beams in practical realizations of TCD spectroscopy to investigate biological and other materials that are opaque in the visible range but transparent for THz radiation. To demonstrate this capability, we measured TCD spectra of several representative biological samples (**Figure 3-18**, including a leaf of sugar maple tree (*Acer saccharum*), an elytron of green beetle (*Chrysina gloriosa*), a petal of dandelion (*Taraxacum officinale*), a piece of pig fat and pellets of amino acid (*L*-, *D*- and *rac*-cystine). Here, the kirigami modulators function similarly to photoelastic modulators (PEMs) in conventional circular dichroism spectrometers (*58*) by generating left- and right- elliptically/circularly polarized light and TCD spectra were calculated directly from difference of transmission-intensity between left and right elliptically polarized THz beam (EPB) generated by kirigami modulators according to Eq. 25:

$$TCD\ by\ kirigami\ modulator = tan^{-1}(\frac{{I_{LK}}^{1/2} - {I_{RK}}^{1/2}}{{I_{LK}}^{1/2} + {I_{RK}}^{1/2}}) \quad (25)$$

where, I_{LK} and I_{RK} are the intensities of the left and right EPB after passing through sample, respectively. **Figure 3-18g** shows the TCD spectrum from air establishing the noise level of the TCD measurement over the full THz range of interest. We observed distinct TCD spectra from the tested biomaterials that can be associated with the chiral structural organization. An exemplary case is the transmissive TCD measurements of an elytron of *C. gloriosa* beetle (**Figure 3-18b** and **Figure 3-18c**), which is known to have the selective reflection of circularly polarized light in the visible range (*62*). A positive peak of TCD (**Figure 3-18h**) as large as about 3° at 0.68 THz is observed in the red circled area in **Figure 3-18f**. The strong chiroptical activity in the THz range for elytra can be associated with the chiral conical structures (**Figure 3-18d**) with dimensions of

about 10 microns having cholesteric liquid crystal phase (**Figure 3-18e**) (*62*). Results of computed TCD simulations (**Figure 3-24**) using models of the exoskeleton structure support this analysis. An additional case is the measurement of TCD from pellets of amino acid. Mirror-like image between *L*- and *D*-cystine at around 0.73 THz is obtained while TCD vanishes in the racemic state.

3.8.1 TCD of Biological samples using Kirigami Modulator

To further demonstrate the application of kirigami chiroptical modulators for TCD measurements of real biological samples, we measured TCD spectra of the elytron of a June beetle, a petal of a dandelion flower, a leaf of a maple tree and a piece of pig fat. Due to the small size of some biological samples, a focused THz beam with ~500 μm spot size was used and the schematic of the experimental setup is shown in **Figure 3-19**. The whole setup was enclosed in a box purged by extra-dry nitrogen and the relative humidity was maintained below 3% to minimize the water vapor absorption and to maximize the measurement sensitivity. The kirigami chiroptical modulators with 37.5° slant angle were used to generate left- and right-handed elliptically polarized beams. In some cases, Savitzky-Golay method is used reduce the noise. **Figure 3-20** shows the results: (d) the reference, with no biological sample in place, shows near zero TCD indicating the intensity transmissions of the two kirigami modulators were almost the same; (e) the sample of a maple leaf shows a very small chiroptical response with slightly noisier curves, which mainly could come from the lower signal-to-noise ratio caused by the THz absorption by the leaf; (f) a petal of a dandelion flower shows TCD signals between 0.3-0.8 THz with negative value and with a TCD that increases as the input ellipticity gets larger; (g) the sample of pig fat also shows negligible TCD. As we show here, characterizing the chirality of matter through

kirigami TCD spectroscopy could be the starting point for further studying of biological microstructure as well as a variety of biomolecules such as proteins and nucleic acids.

The measured absorption coefficients of these biological samples are shown in **Figure 3-21**. The oscillations in the absorption spectra mainly come from the THz pulse reflection inside the photoconductive THz emitter (Tera-SED10, Laser Quantum) which is made from ~640 μm thick low-temperature grown GaAs giving an oscillation period of approximately 0.06 – 0.07 THz. Here, the measured transmittance, $T = \frac{I_{sam}(\omega)}{I_{ref}(\omega)} = \frac{(E_{sam}(\omega))^2}{(E_{ref}(\omega))^2}$, is obtained from the THz transmittance through a sample attached to an aperture, $I_{sam}(\omega) = (E_{sam}(\omega))^2$, divided by the THz transmittance through the void aperture, $I_{ref}(\omega) = (E_{ref}(\omega))^2$. The absorption coefficient (α) is calculated by

$$\alpha(\omega) = -\frac{\ln(T)}{d_s} \tag{26}$$

where d_s is the thickness of the sample (*23*). All thicknesses were determined from the cross-sectional images using optical microscopy as shown in **Figure 3-22**. Here, the measured thickness for an elytron is about 250 μm, for a petal is about 200 μm, for a leaf is about 1mm and for a piece of fat is about 1 mm.

3.8.2 Linear and Circular Dichroism measured by Kirigami Modulator

Since the polarizations generated by kirigami modulators are frequency dependent and elliptical, the contribution of linear dichroism i.e. the anisotropic absorption of the sample should be taken into account.

To confirm TCD signal does come from the chirality of the elytron, we conducted the TCD measurements using kirigami modulators at three different positions on the same elytron with different random orientations. As shown in **Figure 3-23**, all three results have similar curve shapes and TCD are all positive around the main peak at ~ 0.7 THz. Moreover, all these results show the same increasing trend as the ellipticity of the input THz beam gets larger. These indicate that the measured TCD signal is mainly induced by chiral structures which should be modulated by ellipticity of the input beam and always show same positive sign independent of the position and orientation of the elytron.

3.8.3 Modeling of Microstructure of C.gloriosa and its TCD Simulation

To investigate the microscopic origin of the chiroptical activity in the THz range, we made 3D model for TCD simulation based on our observation. As reported, under optical micrographs, the exocuticle of *C.gloriosa* seems to consist of hexagonal cells (~10 μm), where each cell show bright yellow reflection from the core and greenish reflection from the body (**Figure 3-24a**) (*62*). It is well-known that this cuticle of beetles is a composite material including chitin and these chitin molecules self-organize into a helicoidal structure and show cholesteric liquid crystal phase (*63*). To mimic these mesoscale chiral conical structures, we used the 3D model of spiral structure and made arrangement of spiral exactly same as that of real exocuticle (**Figure 3-24b** and **c**). Besides,

we took into account the curvature of the surface. This curved feature can be found in **Figure 3-24a**, where only the central parts of the images are in focus. TCD simulations were numerically investigated with finite element simulation software (COMSOL Multiphysics 5.2a, COMSOL Inc.) using the 3D model. We used the refractive index for spiral from the experiment results. The real and imaginary part of refractive indices were determined from the transmission data of beetle, the detailed method is described elsewhere (*64*). Here, the diameter of top and bottom, height and number of turns are 0.5 μm, 10 μm, 10 μm and 10, respectively. We also tested various parameters for spiral, but the resulted TCD spectra were almost same, not that dramatic change was observed. Lastly, we considered the factor of kirigami modulator. Since the ellipticity of the beam generated by the kirigami modulator is frequency dependent, the normalized ellipticity with respect to the frequency was taken into account.

3.8.4 TCD Measurements of Pellets of Amino Acids

For the control experiment, we also measured pellets of amino acid. The samples in powder were pressed to self-standing pellets in 35 mm diameter. Thickness of the samples is all set to 4 mm. Pellets were subjected to 1 hour acid treatment by HCl (hydrochloride acid) to improve their crystallinity. Pellets of amino acids were measured under the ambient environment and the peaks from water were processed by algorithm. **Figure 3-25** shows the absorption coefficients and TCD results of the *L*-, *D*-cystine and its racemic mixture. We can clearly see the mirror-like image between *L*- and *D*-cystine at around 0.73 THz, and also the signal vanishes in the racemic state. There is some discrepancy in magnitude and shape between and *L*- and *D*-cystine. We think that this is because the *L*-cystine can be obtained by hydrolysis of animal materials but *D*-cystine can

only be artificially synthesized, so their tertiary or secondary structures, densities and purities could not be exactly same.

3.9 Conclusions

In conclusion, the double-pattern design of kirigami materials combining submillimeter cuts and micrometer scale plasmonic stripes affords the real-time tunability of helical structures oriented perpendicularly to the propagation of the light beam. Kirigami optical elements make possible realization of TCD spectroscopy and better understanding of liquid-crystal-like organization of soft and mineralized tissues (*65*, *66*). The lightweight capabilities and high polarization efficiency of kirigami optics open a possibility of portable compact THz spectrometers. The realization of real-time polarization modulation of THz beams also enable advances in secure high bandwidth communication and non-invasive imaging.

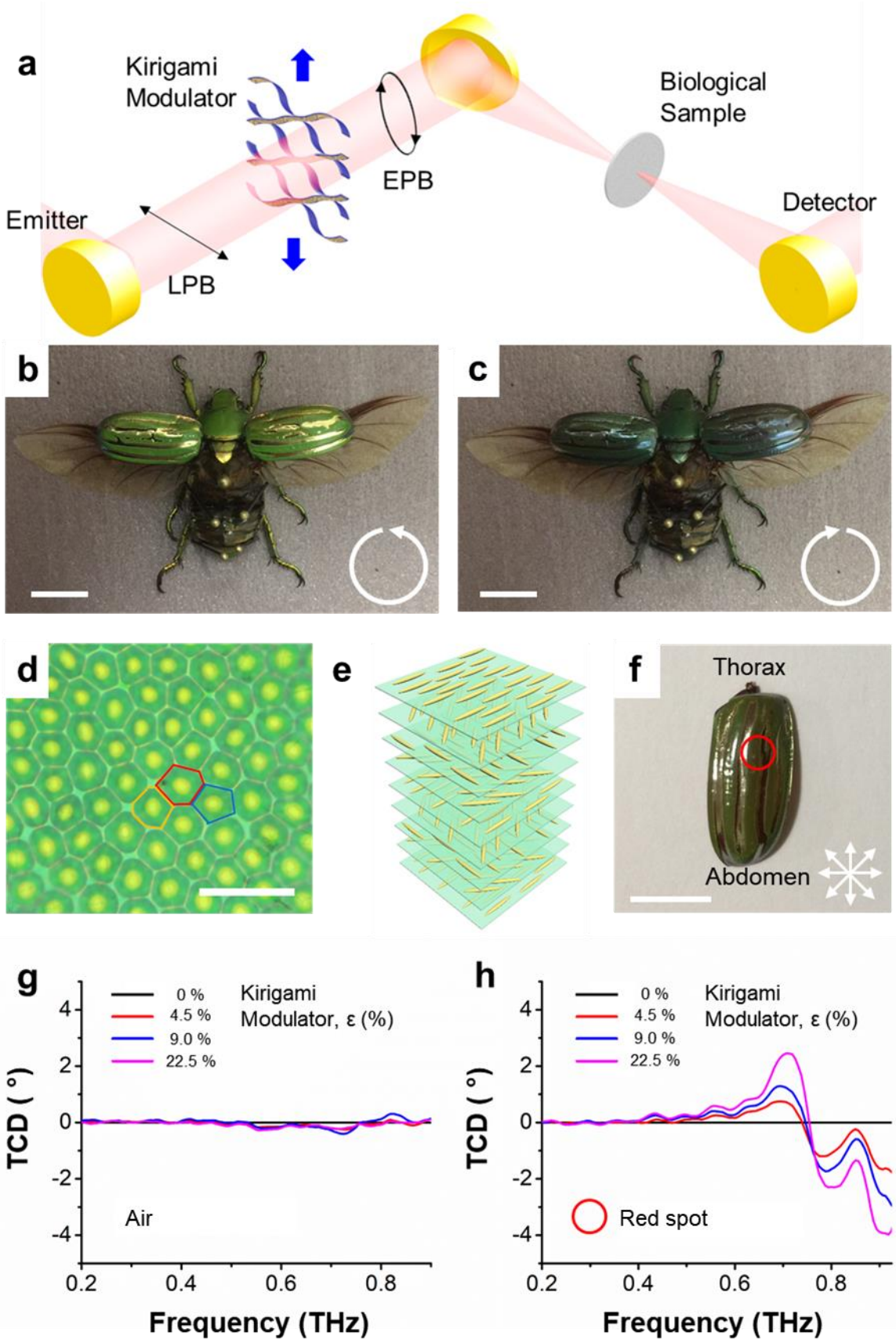
a
Kirigami
Modulator
EPB
Biological
Sample
Emitter
LPB
Detector
b
c
d
e
f
Thorax
Abdomen
g
0 %
4.5 %
9.0 %
22.5 %
Kirigami
Modulator, ε (%)
TCD (°)
Air
Frequency (THz)
h
0 %
4.5 %
9.0 %
22.5 %
Kirigami
Modulator, ε (%)
TCD (°)
Red spot
Frequency (THz)

Figure 3-18 Measurements of TCD using kirigami chiroptical modulator. a, Schematic of TCD spectroscopy using kirigami modulator. A focused THz beam with ~500 μm spot size was used to explore biological sample. LPB and EPB indicate the linearly and elliptically polarized beam in respectively. **b and c,** Photographs of the beetle C.gloriosa with a left and right circular polarizer front of the camera, respectively. **d,** An optical microscopy image of the exoskeleton of beetle C.gloriosa. The shape of the cells is pentagonal in blue, hexagonal in red and heptagonal in orange. Scale bar is 20 μm. **e,** Schematic representation of Bouligand structure. **f,** Image of an elytron of C.gloriosa without polarizer. Red circle indicates the spot corresponding to the TCD measurements. **g,** TCD spectrum from air. **h,** TCD spectrum from C.gloriosa measured by kirigami modulator at four different strains (%).Scale bars in **b**, **c and f** are 1 cm. Reproduced from ref.(*1*).

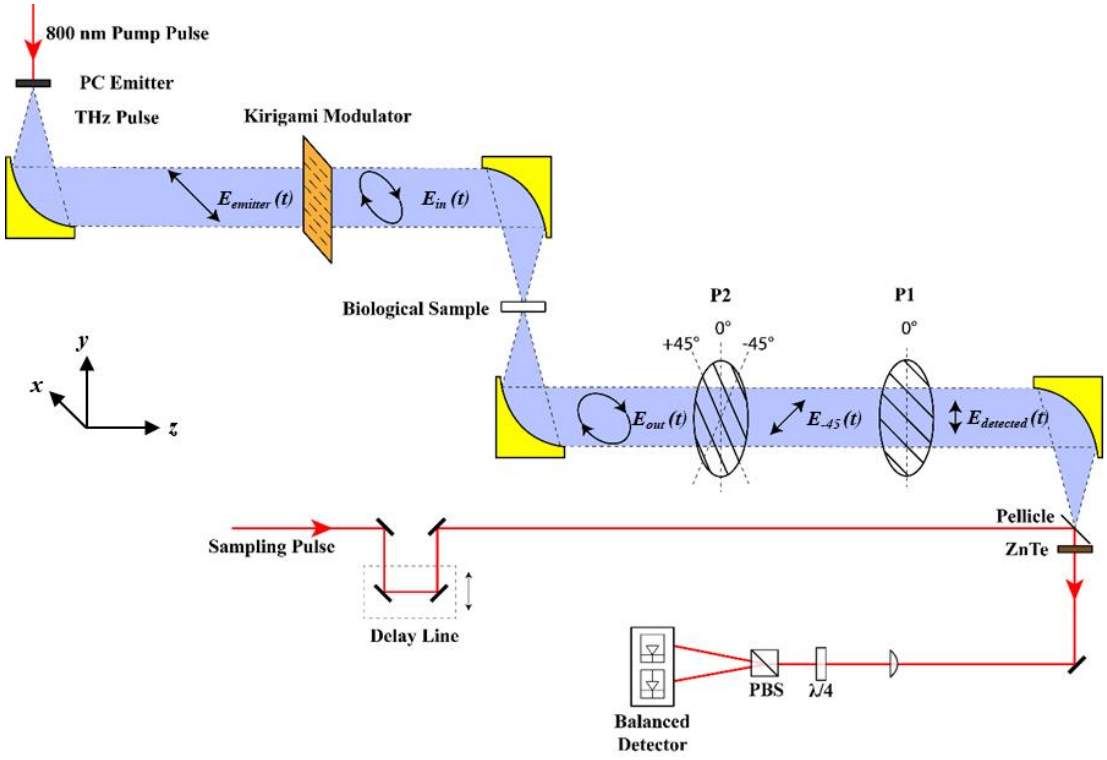

Figure 3-19 Schematic of the experimental TCD setup for biological samples. The elliptically/circularly polarized THz beam generated by the kirigami modulator is focused by an off-axis parabolic gold mirror to a spot size of approximately 500 μm and acts as the input for the biological samples. The transmitted THz beam through the sample is collected and collimated by another off-axis parabolic gold mirror for detection. Reproduced from ref.(*1*).

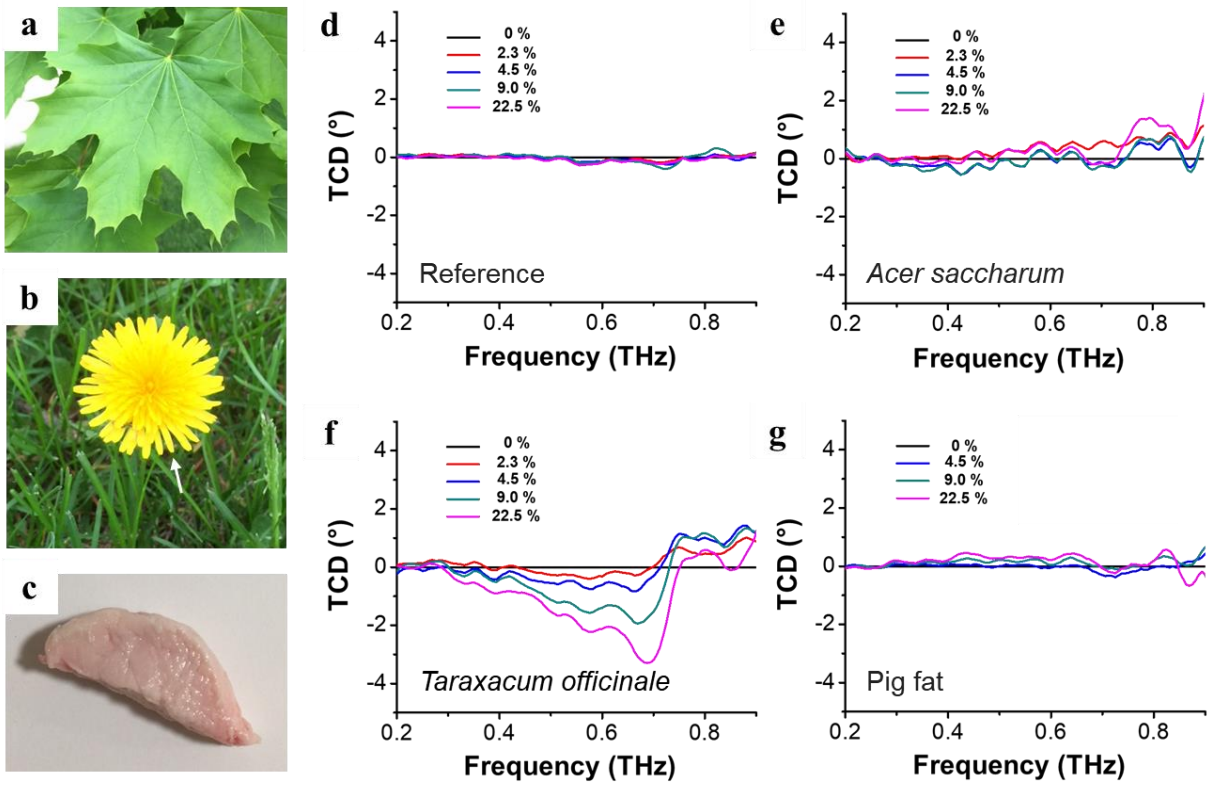

Figure 3-20 Experimental TCD spectra modulated by kirigami of biological samples. Photographs of a leaf of maple sugar tree (**a**), a petal of dandelion (**b**) and a piece of pig fat (**c**). The arrow in the dandelion image in (**b**) indicates the actual sample for the measurement. (**d**) to (**g**) show TCD spectra of reference, a leaf (Acer saccharum), a petal (Taraxacum officinale) and a piece of pig fat, respectively. The legend shows the strains applied to the kirigami modulators. The TCD curves for each sample were normalized to its ε = 0 % curve. Reproduced from ref.(*1*).

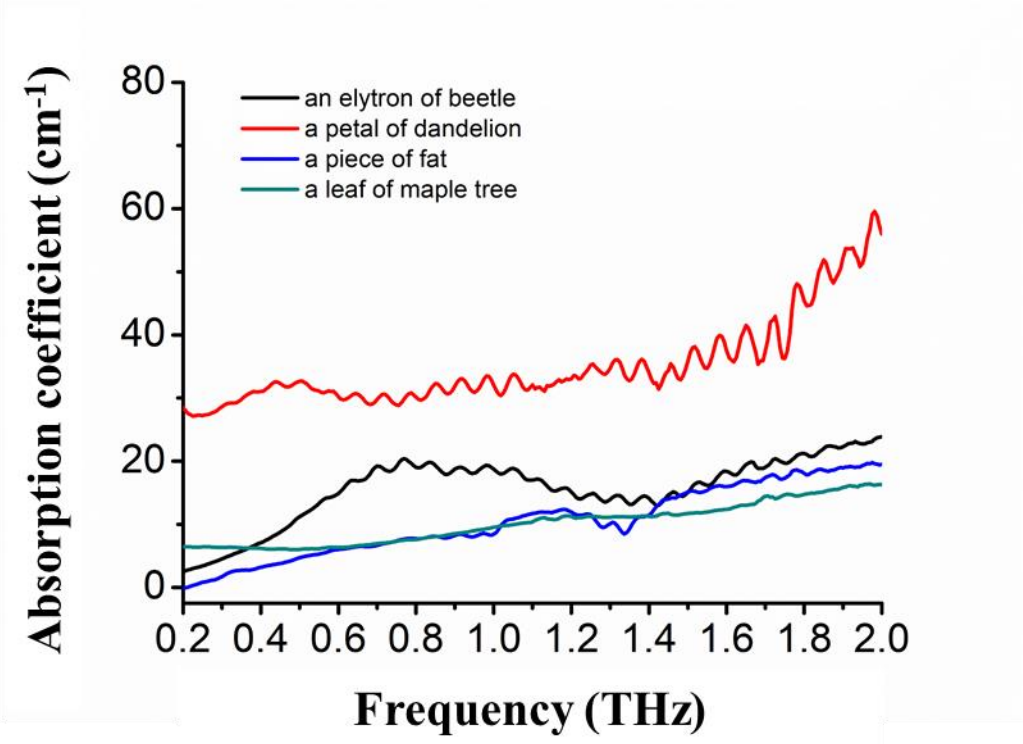

Figure 3-21 Absorption coefficient spectra of four biological samples. Absorption coefficients of an elytron of beetle, a petal of a dandelion, a leaf of a maple tree and a piece of pig fat. The oscillations with period of approximately 0.07 THz come from the pulse reflection inside the THz emitter. Reproduced from ref.(*1*).

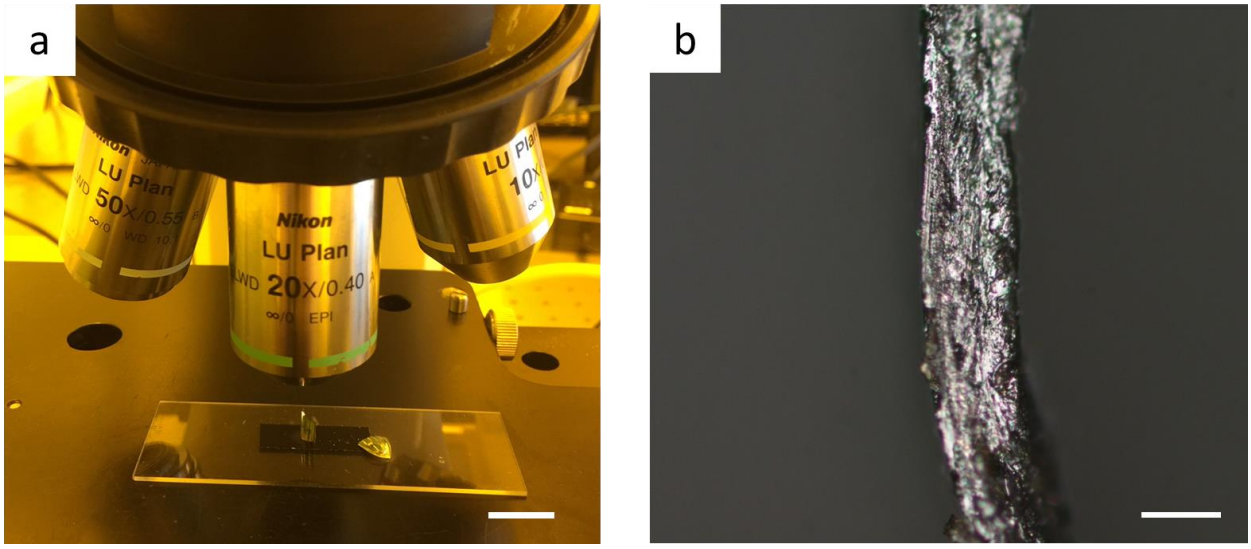

Figure 3-22 Thickness measurement of an elytron of beetle. (a) Photograph of vertically aligned elytron, Scale bar is 1cm. (b) optical microscope image of cross sectional view for an elytron. Scale bar is 250 μm. Reproduced from ref.(*1*).

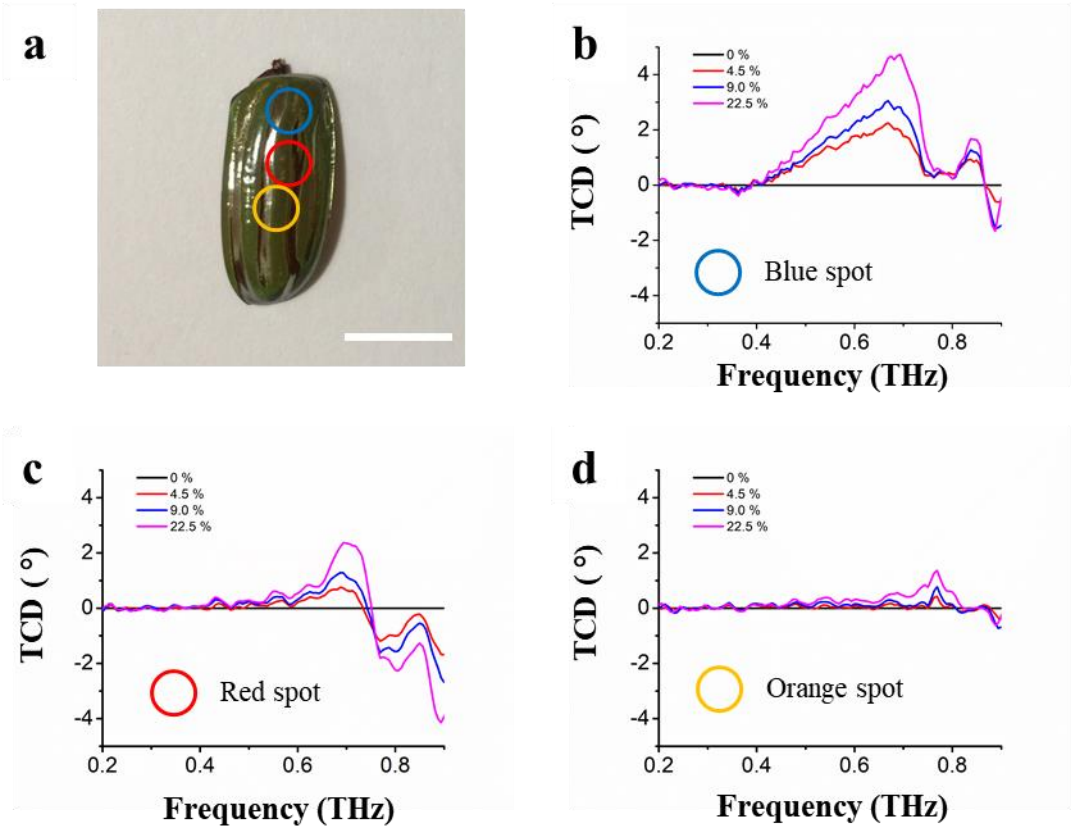

Figure 3-23 Experimental TCD spectra of different spots of the elytron of beetle measured by kirigami modulators. (a) Image of an elytron of C.gloriosa without polarizer. Scale bar is 1cm. (b) to (d) are the TCD spectra obtained from three different spots, blue, red and orange, respectively. Reproduced from ref.(*1*).

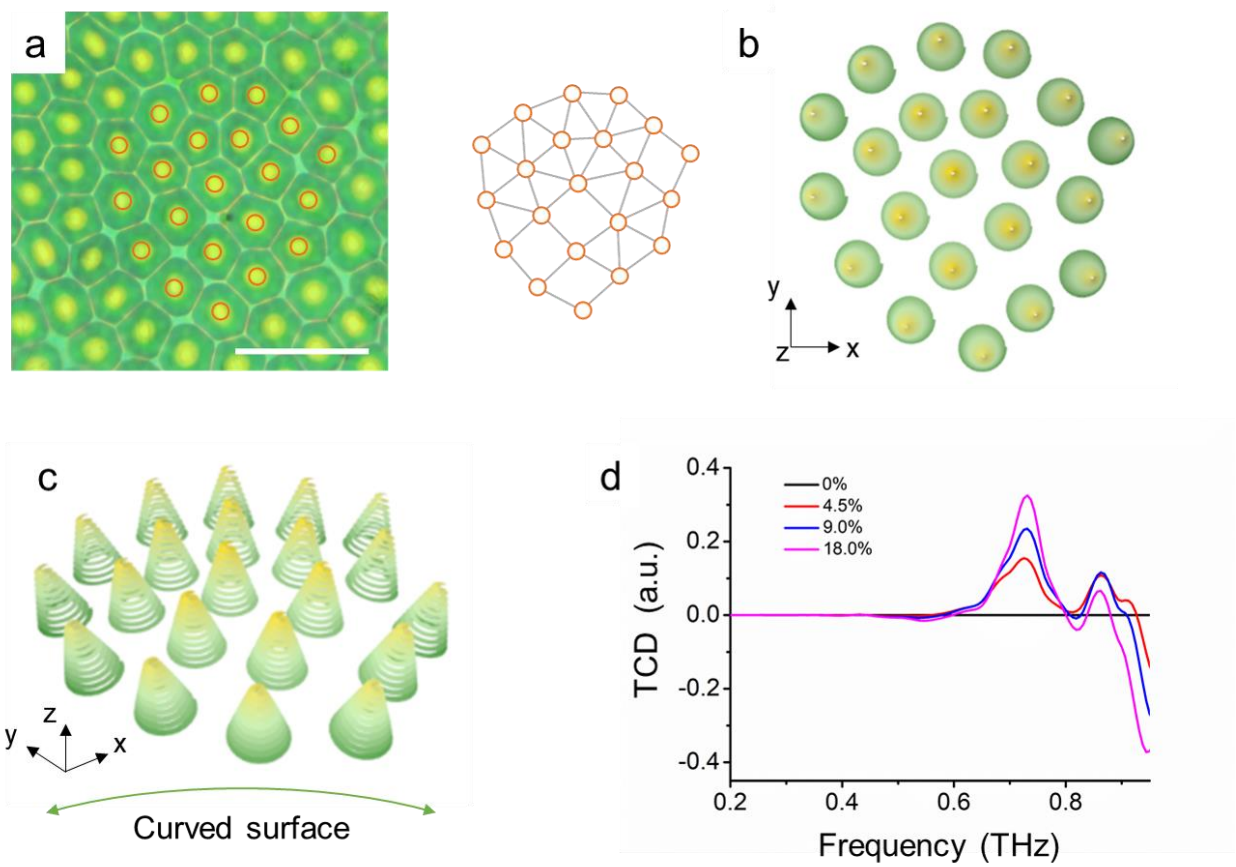

Figure 3-24 Morphology and microstructure of cellular pattern of C. gloriosa (a) An optical micrograph of the exoskeleton of beetle C. gloriosa. Bright yellow reflections from the core and greenish reflection from the edges. Scale bar is 25 μm. (b) and (c) top and tilted view of the reconstructed 3D model, respectively. (d) Computed TCD spectrum measured by chiral kirigami modulator**.** Reproduced from ref.(*1*).

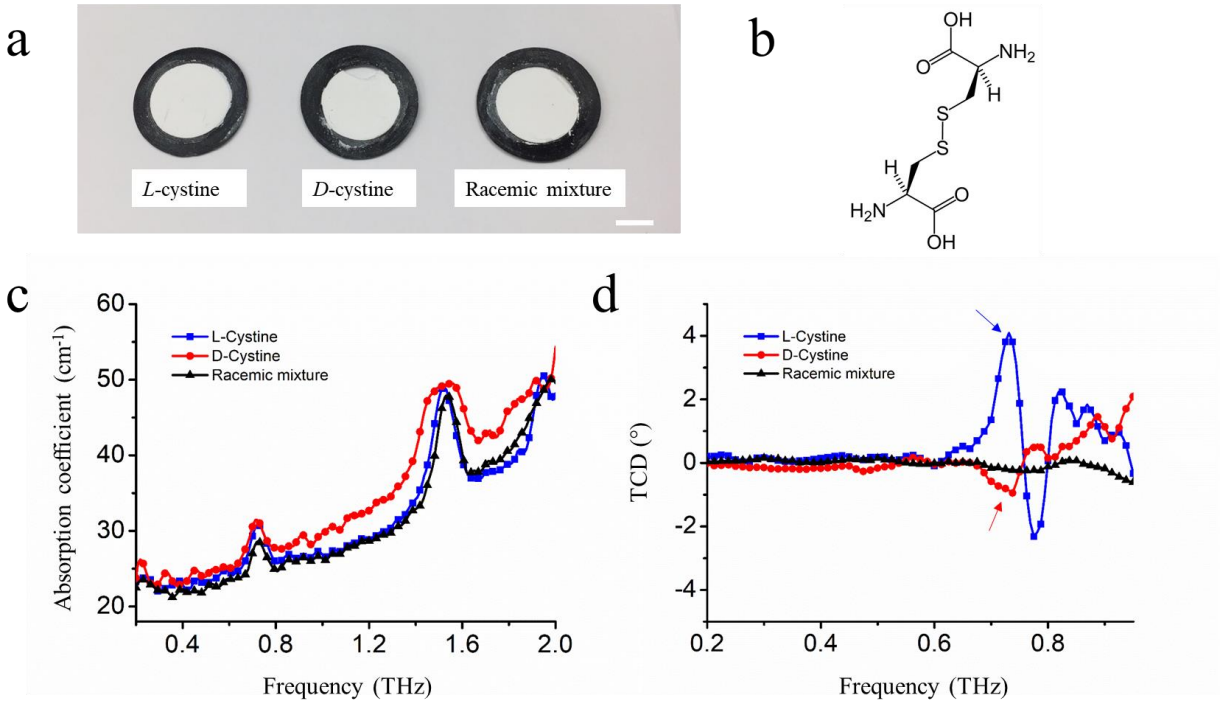

Figure 3-25 Terahertz measurement results of *L*-, *D*-, and *rac*-cystine. (a) Photo image of amino acid pellets. Scale bar is 1cm. (b) Molecular structure of L-cystine. (c) and (d) show absorption coefficients and TCD results, respectively. Reproduced from ref.(*1*).

Chapter 4. Chiral Phonons in Biocrystals[2]

4.1 Introduction

The vibrations in simple crystal lattices, typically described as longitudinal and transverse phonons, commonly consist of parallel or perpendicular oscillatory displacements of atoms, in respect to the propagation direction. As the complexity of the crystal lattice increases, the normal modes of phonons may become chiral as rotatory components emerge. Besides their fundamental significance, the chiral phonons favoring specific mirror-asymmetrical left- and right-handed modes could be uniquely suitable for application in a range of emergent chiroptical technologies (*67–75*) but macroscale materials supporting such lattice vibrations have not been hitherto identified.

Chiral phonons were initially predicted computationally and then recognized spectroscopically in two-dimensional materials, such as MoS_2 and WSe_2 (*67–70*). The hexagonal

---

[2] From Won Jin Choi, Keiichi Yano, Minjeong Cha, Felippe M. Colombari, Yichun Wang, Sang Hyun Lee, John M. Kruger, André F. de Moura* and Nicholas A. Kotov* "Chiral Phonons in Biocrystals" *Res. Sq. Prepr. arXiv* **2021**, 10.21203/rs.3.rs-248321/v1. https://doi.org/10.21203/rs.3.rs-248321/v1.(*2*)

Contributions: W.J.C., K.Y., and N.A.K. contributed to the design of the research, data analysis. W.J.C., A.F.M and N.A.K prepared the manuscript. W.J.C. performed the all the optical experiments and SEM measurements with analysis. K.Y. recrystallized all the biomolecules and performed the XRD measurements with analysis. F.M.C, Y.W. and A.F.M. performed the MD simulations. M.C. and S.L. provided technical support for python code and MATLAB code for plot and fitting. J.M.K provided the cystine stones.

lattices of these monolayer materials are, however, achiral. The left and right modes coexist as degenerate phononic states, which makes their individual observation and utilization difficult because the chiroptical light polarization effects from these lattice vibrations cancel out each other in bulk materials. One can hypothesize that chiral phonons with specific polarization should be common for crystals from mirror-asymmetric biomolecules, which for brevity will henceforth be referred to as *biocrystals*. Depending on the dispersion relations and the photon-phonon coupling strengths, the modes with left and right rotational components can be potentially detected by chiroptical spectroscopy because the degeneracy of the phonon states is lifted in biocrystals. The relationships between the asymmetry of the biomolecules forming the crystal lattice, their space group, and the normal modes of sustained phonons are some of the fundamental unanswered questions that could be addressed after that. Additionally, the different modes of chiral phonons in biocrystals would provide a unique tool for probing biomolecular arrangements in a wide range of structures with direct relevance to drug synthesis, biochemical quality control, protein folding, and disease diagnostics (*76–79*).

4.2 Challenges and Methodological Problems

Several methodological problems have thus far prevented the observation of chiral phonons in biocrystals. Specific chemical structures of prospective biomolecules, preferred crystal lattices, and spectroscopic modalities for the observation of chiral phonons are not known. Even their expected spectral range is ambiguous, because the non-covalent interactions defining the structure and deformations in biocrystals can theoretically cover a wide range of vibrational frequencies (*22*, *79*), leading to large spectral shifts compared to those of Weyl semimetals (*70*, *80*).

Furthermore, computational predictions of the collective vibrational modes of crystals with complex unit cells are also problematic. The diversity of non-covalent interactions, non-harmonicity and multiplicity of the coupled modes possible for biocrystals necessitate large models and thus become computationally too expensive, especially for long-period oscillations involving the collective movement of multiple molecular segments (*81–83*) that are characteristic of phonons. Numerical errors arising from convergence tolerances further exacerbate computational challenges, especially for *in-silico* discovery of low frequency modes (*81*, *82*).

4.3 Amino acids as Experimental models

Based on prior spectroscopic studies of proteins, DNA, and amino acids (*22*, *81*, *83–88*), we hypothesized that chiral phonons in biocrystals would be located in the far-infrared (IR) to terahertz (THz) spectral window. While the resonance frequency of 'localized' intermolecular vibrations of non-covalent interactions mostly lie in the mid-IR range, the phononic modes of biocrystals are likely to be observed between 0.2 and 3 THz (6 to 100 cm^{-1}) since the energies of their intermolecular forces lie between ~0.001 and ~0.02 eV, matching the photon energies of THz radiation. The molecular masses of units undergoing these vibrational motions are also relatively large (>50 g/mol) (*22*, *83*, *86*), which dramatically reduces the phonon frequencies compared to inorganic crystals.

We chose amino acids (AAs) as experimental and computational models because they are structurally versatile and serve as building blocks for many biomolecules. They are also known to have absorption bands of uncertain origin in the far-IR and THz ranges (*81*, *83*, *87*, *88*). Importantly, almost all AAs are available as left/right enantiomers and computational difficulties

related to calculations of chiral phonons can be addressed accurately and efficiently with the recently developed semiempirical GFN2-XTB Hamiltonian (*89*).

However, AAs also have disadvantages as experimental models for chiral phonons, due to the coexistence of multiple crystalline phases and hydration states in their bulk crystals. The seemingly minor presence of the opposite enantiomer and impurities can also distort or change their crystal habits (*22, 77*). Furthermore, AA powders and pellets have a wide range of particle sizes with crystals larger than 200 μm persisting even after grinding. Large dimensions and multiple crystal habits severely deteriorate the quality of THz absorption (TA) (*90*) and THz circular dichroism (TCD) spectra due to Mie scattering, resulting in broadened spectra with distorted peak features. A further challenge in this study is that the implementation of chiroptical spectroscopy methods in the THz range is far from being trivial especially for biological materials (*1*, *38*, *91*).

4.3.1 Recrystallization of 20 proteinogenic amino acids (AAs)

A recrystallization process is described in a flow diagram in **Figure 4-1**. In general, samples (approx. 0.5 to 2 grams) of AA enantiomers were stirred in a glass vial in boiling E-pure water until completely dissolved. The resultant hot solution was transferred into a Petri dish covered with a lid and left undisturbed for ~1 day for the crystal growth. The obtained crystals were filtered and washed with ethanol at least three times under reduced pressure. For anhydrous crystals, the filtered crystals were further dried at 60 °C under reduced pressure for 12 hours.

Specific recrystallization conditions for AAs are summarized in **Table 4-1**. E-pure water was used as solvent for most AAs, while 1 M oxalic acid solution and ethanol were used for tryptophan

(Trp) and proline (Pro), respectively, due to their low solubility in E-pure water. The hydration states of arginine (Arg) and asparagine (Asn) were controlled by the final heat drying process; as-recrystallized hydrated forms of arginine and asparagine crystals can be converted, by heat drying at 60 °C, into their anhydrous forms. Lysine (Lys) was used as received without further recrystallization.

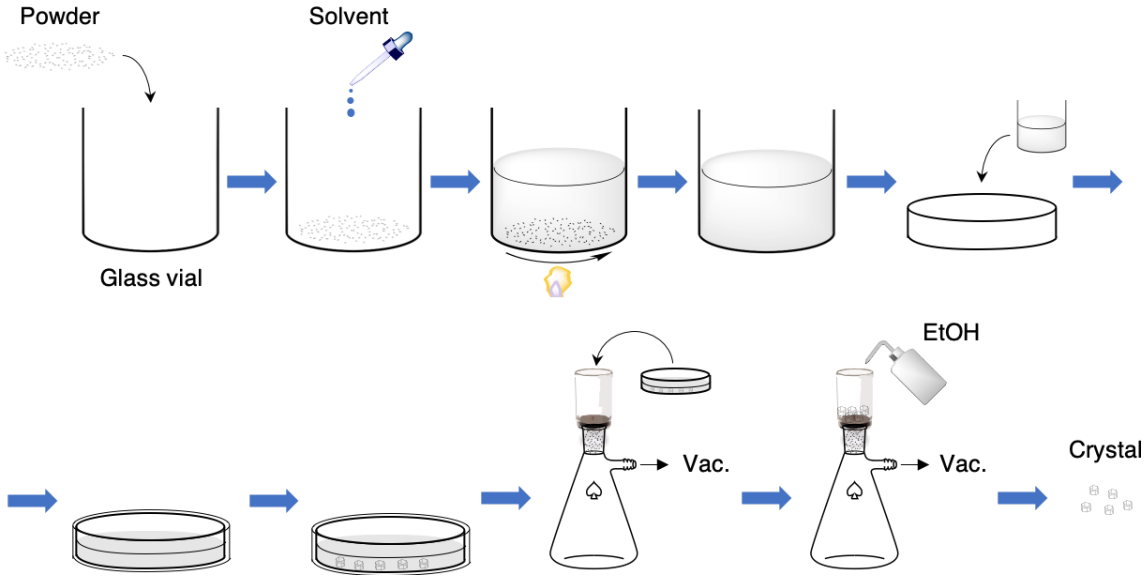

Figure 4-1 Recrystallization procedure for AAs and dipeptides. A powder sample of an AA or dipeptide was added to solvent. The dispersion was heated and stirred until AAs or dipeptide completely dissolved at 100 °C. The resultant hot solution was transferred to a Petri dish covered with a lid and cooled overnight. The dispersions with recrystallized crystals were filtered under vacuum and crystals were washed with ethanol at least three times. To obtain anhydrous crystals, the filtered crystals were dried at 60 °C at low pressure for 12 hours. Specific details of the recrystallization protocol for each AA and peptide are given in **Table 3.1**. Reproduced from ref.(*2*).

AAs/dipeptide	L/D	Product No.	Amount	Solvent	Volume	Yield (g, %)
Arginine (Arg)	L	A5006-100G	1.8 g	E-pure water	3.0 mL	1.5 g, 69%[*1]
	D	A2646-5G	1.8 g	E-pure water	3.0 mL	1.7 g, 78%[*1]
Histidine (His)	L	H8000-25G	1.4 g	E-pure water	13 mL	1.0 g, 71%
	D	H3751-5G	1.4 g	E-pure water	13 mL	1.0 g, 71%
Lysine (Lys)	L	L5501-5G	Used as received without further recrystallization.			
	D	L8021-5G	Used as received without further recrystallization.			
Glutamic acid (Glu)	L	128430-100G	1.8 g	E-pure water	35 mL	1.5 g, 83%
	D	G1001-25G	1.0 g	E-pure water	20 mL	0.71 g, 71%
Aspartic acid (Asp)	L	A93100-100G	0.54 g	E-pure water	22 mL	0.40 g, 74%
	D	219096-25G	0.54 g	E-pure water	22 mL	0.42 g, 74%
Glutamine (Gln)	L	G3126-100G	1.5 g	E-pure water	9.0 mL	1.2 g, 80%
	D	D9003-1G	0.80 g	E-pure water	5.0 mL	0.62 g, 78%
Asparagine (Asn)	L	A0884-25G	1.0 g	E-pure water	9.0 mL	0.95 g, 84%[*2]
	D	441697-25G	1.0 g	E-pure water	9.0 mL	0.79 g, 70%[*2]
Cysteine (Cys)	L	W326305-100G	1.5 g	E-pure water	5.5 mL	0.69 g, 46%
	D	30095-1G	0.80 g	E-pure water	3.0 mL	0.49 g, 61%
Threonine (Thr)	L	T8625-10G	1.5 g	E-pure water	10 mL	0.83 g, 55%
	D	T8250-5G	1.5 g	E-pure water	10 mL	0.80 g, 53%
Serine (Ser)	L	S2600-100G	1.5 g	E-pure water	3.0 mL	1.4 g, 93%
	D	S4250-5G	1.5 g	E-pure water	3.0 mL	1.1 g, 73%
Glycine (Gly)	–	G7126-100G	1.5 g	E-pure water	3.0 mL	0.95 g, 63%
Alanine (Ala)	L	A25802-100G	2.0 g	E-pure water	4.0 mL	1.7 g. 85%
	D	A7377-25G	1.0 g	E-pure water	2.0 mL	0.44 g. 44%
Proline (Pro)	L	81709-25G	1.0 g	Ethanol	25 mL	0.62 g, 62%
	D	858919-5G	0.40 g	Ethanol	10 mL	0.20 g, 50%
Valine (Val)	L	V0500-25G	1.5 g	E-pure water	18 mL	0.63 g, 42%
	D	855987-5G	1.0 g	E-pure water	12 mL	0.42 g, 42%
Isoleucine (Ile)	L	I2752-10G	1.0 g	E-pure water	18 mL	0.44 g, 44%
Leucine (Leu)	L	L8000-25G	1.0 g	E-pure water	20 mL	0.38 g, 38%
	D	855448-2.5G	0.80 g	E-pure water	25 mL	0.25 g, 31%
Methionine (Met)	L	M9625-25G	1.0 g	E-pure water	18 mL	0.13 g. 13%
	D	M9375-5G	1.0 g	E-pure water	18 mL	0.12 g, 12%
Phenylalanine (Phe)	L	P2126-100G	1.5 g	E-pure water	21 mL	0.96 g, 64%
	D	P1751-5G	1.0 g	E-pure water	14 mL	0.46 g, 46%
Tyrosine (Tyr)	L	T3754-50G	1.0 g	1 M Oxalic acid solution	16 mL	0.50 g, 50%
	D	855456-5G	1.0 g	1 M Oxalic acid solution	17 mL	0.49 g, 49%
Tryptophan (Try)	L	T0254-25G	0.50 g	E-pure water	15 mL	0.28 g, 56%
	D	T9753-5G	0.50 g	E-pure water	20 mL	0.24 g, 48%
Cystine (CYT)	L	C8755-100G	2.0 g	1 M HCl solution	16 mL	0.48 g, 24%
	D	286463-1G	1.0 g	1 M HCl solution	7.7 mL	0.15 g, 15%
	DL	C8630-5G	Used as received without further recrystallization.			
Deuterated Cystine (dCYT)	L	C8755-100G	2.0 g	1 M DCl solution in D_2O	18 mL	0.28 g, 14%

Table 4-1 Conditions for recrystallization. Reproduced from ref.(*2*).

4.3.2 Recrystallization of Cystine (CYT)

L- and *D*-cystine (CYT) were recrystallized according to the aforementioned procedure using 1M HCl solution. Deuterated *L*-cystine was recrystallized similarly but using 1 M deuterium chloride (DCl) solution in deuterium oxide (D_2O). Racemic *DL*-cystine was used as received without further recrystallization.

4.3.3 Characterization of Crystalline Phases and Sizes of Crystals

Crystalline phases of crystals were characterized by powder X-ray diffraction (PXRD) measurements using a SmartLab Powder X-ray diffractometer (Rigaku) equipped with a 2.2-kW Cu anode (Cu*K*α, λ = 1.54 Å), a *K*β filter, and a D/teX Ultra 250 high speed silicon strip 1D detector. The PXRD data were collected in a range of 15 to 60° in 2θ by a step-scan mode with a step size of 0.01°. The crystals were ground as fine as possible using a pestle and a mortar and mounted onto a glass plate for their PXRD measurements. The phase purity and space group of crystals were analyzed by comparing their experimental diffraction patterns with the reported data of the corresponding single crystals. The single crystal data were collected from the Cambridge Crystallographic Data Centre (CCDC)(*92*) and their diffraction patterns were reproduced using the Mercury software (*93*). **Figure 4-2** and **Figure 4-3** shows PXRD patterns of crystals and their crystalline phases are summarized in **Table 4-2**.

The precise size and crystal habit of each AA crystal was measured by scanning electron microscope (Tescan Mira3 FEG SEM) (**Figure 4-4**). Their size distributions were estimated by static light scattering measurements using a Mastersizer 2000 (Malvern) equipped with a Hydro 2000S wet dispersion unit. The size distribution data were collected in a wide range of 0.01 to

10,000 µm (**Figure 4-5**). The ground crystals were dispersed in 2-propanol in a measuring cell and subjected to intense stirring and agitation to ensure homogeneity. Effects of size and the crystallinity of the AA crystals on the THz behavior are discussed in the 'Discussion' section (**Figure 4-6** to **Figure 4-8**).

4.3.4 Preparation of slurry samples

The use of slurry samples has long been adopted in infrared spectroscopy, known as the Nujol mulling method (*94*). Slurry samples of crystals, 50 wt%, were prepared by mixing ~150 mg of ground crystals with ~150 mg (~180 µL) of mineral oil using a micro-spatula. The slurry samples were placed between two quartz plates with a ~100 µm thick spacer, and the sandwich cell was pressed by clamps to ensure a flat surface without voids.

4.3.5 Cystine stone samples from canine patients

Use of archived stones obtained from client-owned animals as part of standard veterinary medical care has been approved by the Michigan State University Institutional Animal Care and Use Committee. Four naturally occurring cystine stones removed from two client-owned canine patients as part of standard veterinary medical care were analyzed. All were removed from the bladder or urethra. One patient was a 7-year-old male *American pit bull terrier*, the other was a 6-year-old male *English mastiff*. The size of the cystine stones were between 3.5 mm to 6.0 mm and measured without further treatment.

4.3.6 Commercial L-carnosine (L-CAR) supplements and other various dipeptide samples

Five *L*-CAR supplements from different manufacturers were purchased and analyzed without further treatment: *L*-CAR1 from Bestvite, *L*-CAR2 from Jarrow Formulas, *L*-CAR3 from Now, *L*-CAR4 from Nutricost, *L*-CAR5 from Nova. Powders from each capsule were mixed with mineral oil (50 wt%) and 81 points were measured for 2D plot analysis. All other dipeptides including *L*-carnosine were purchased from Sigma-Aldrich for laboratory samples: *L*-carnosine (C9625-5G), Gly-Gly (G1002-25G), Ala-Tyr (A4003-100MG), Ala-Ala (A9502-1G), Ala-Gln (A8185-5G). Each of the dipeptide samples were analyzed using the slurry method.

AAs/dipeptide	L/D	Hydration state	Space group
Arginine (Arg, R)	L	Dihydrate	$P2_12_12_1$
	L	Anhydrous	$P2_1$
	D	Anhydrous	$P2_1$
Histidine (His, H)	L	Anhydrous	$P2_12_12_1$
	D	Anhydrous	$P2_12_12_1$
Lysine (Lys, K)	L	Hemihydrate	$C2$
	D	Hemihydrate	$C2$
Glutamic acid (Glu, E)	L	Anhydrous	$P2_12_12_1$
	D	Anhydrous	$P2_12_12_1$
Aspartic acid (Asp, D)	L	Anhydrous	$P2_1$
	D	Anhydrous	$P2_1$
Glutamine (Gln, Q)	L	Anhydrous	$P2_12_12_1$
	D	Anhydrous	$P2_12_12_1$
Asparagine (Asn, N)	L	Monohydrate	$P2_12_12_1$
	L	Anhydrous	$P2_1$
	D	Anhydrous	$P2_1$
Cysteine (Cys, C)	L	Anhydrous	$P2_12_12_1$
	D	Anhydrous	$P2_12_12_1$
Threonine (Thr, T)	L	Anhydrous	$P2_12_12_1$
	D	Anhydrous	$P2_12_12_1$
Serine (Ser, S)	L	Anhydrous	$P2_12_12_1$
	D	Anhydrous	$P2_12_12_1$
Glycine (Gly, G)	–	Anhydrous	$P2_1/n$
Alanine (Ala, A)	L	Anhydrous	$P2_12_12_1$
	D	Anhydrous	$P2_12_12_1$
Proline (Pro, P)	L	Anhydrous	$P2_12_12_1$
	D	Anhydrous	$P2_12_12_1$
Valine (Val, V)	L	Anhydrous	$P2_1$
	D	Anhydrous	$P2_1$
Isoleucine (Ile, I)	L	Anhydrous	$P2_1$
Leucine (Leu, L)	L	Anhydrous	$P2_1$
	D	Anhydrous	$P2_1$
Methionine (Met, M)	L	Anhydrous	$P2_1$
	D	Anhydrous	$P2_1$
Phenylalanine (Phe, F)	L	Anhydrous	$C2$
	D	Anhydrous	$C2$
Tyrosine (Tyr, Y)	L	Anhydrous	$P2_12_12_1$
	D	Anhydrous	$P2_12_12_1$
Tryptophan (Try, W)	L	Not assignable.	Not assignable.
	D	Not assignable.	Not assignable.
Cystine (Cyt)	L	Anhydrous	$P6_122$
	D	Anhydrous	$P6_122$
	DL	Not assignable	Not assignable
Deuterated Cystine (dCyt)	L	Anhydrous	$P6_122$

Table 4-2 The crystalline phases of AAs and CYT used for THz spectroscopies. Reproduced from ref.(*2*).

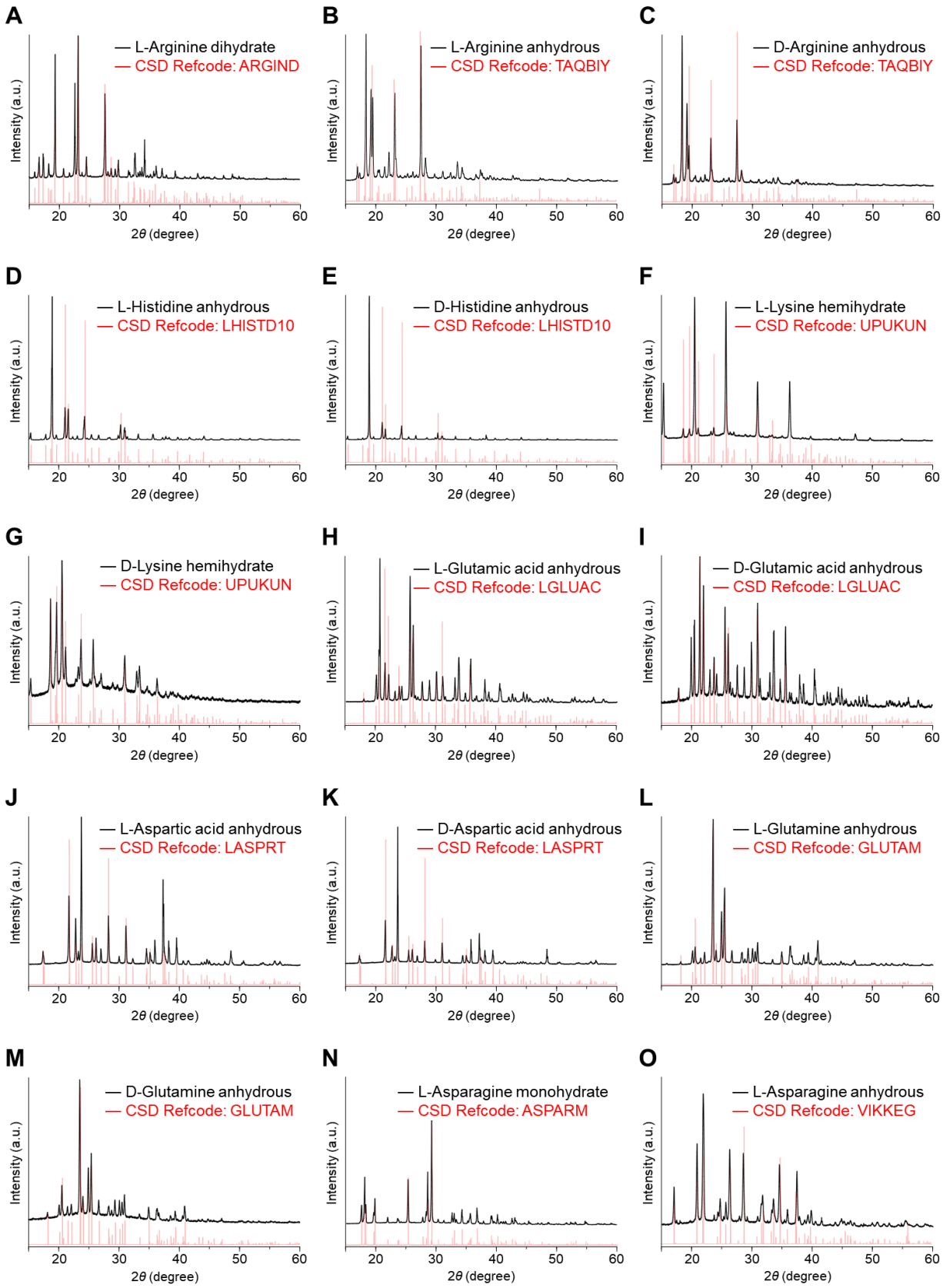
A
— L-Arginine dihydrate
— CSD Refcode: ARGIND
B
— L-Arginine anhydrous
— CSD Refcode: TAQBIY
C
— D-Arginine anhydrous
— CSD Refcode: TAQBIY
D
— L-Histidine anhydrous
— CSD Refcode: LHISTD10
E
— D-Histidine anhydrous
— CSD Refcode: LHISTD10
F
— L-Lysine hemihydrate
— CSD Refcode: UPUKUN
G
— D-Lysine hemihydrate
— CSD Refcode: UPUKUN
H
— L-Glutamic acid anhydrous
— CSD Refcode: LGLUAC
I
— D-Glutamic acid anhydrous
— CSD Refcode: LGLUAC
J
— L-Aspartic acid anhydrous
— CSD Refcode: LASPRT
K
— D-Aspartic acid anhydrous
— CSD Refcode: LASPRT
L
— L-Glutamine anhydrous
— CSD Refcode: GLUTAM
M
— D-Glutamine anhydrous
— CSD Refcode: GLUTAM
N
— L-Asparagine monohydrate
— CSD Refcode: ASPARM
O
— L-Asparagine anhydrous
— CSD Refcode: VIKKEG
Intensity (a.u.)
2θ (degree)
20
30
40
50
60

(Continued)

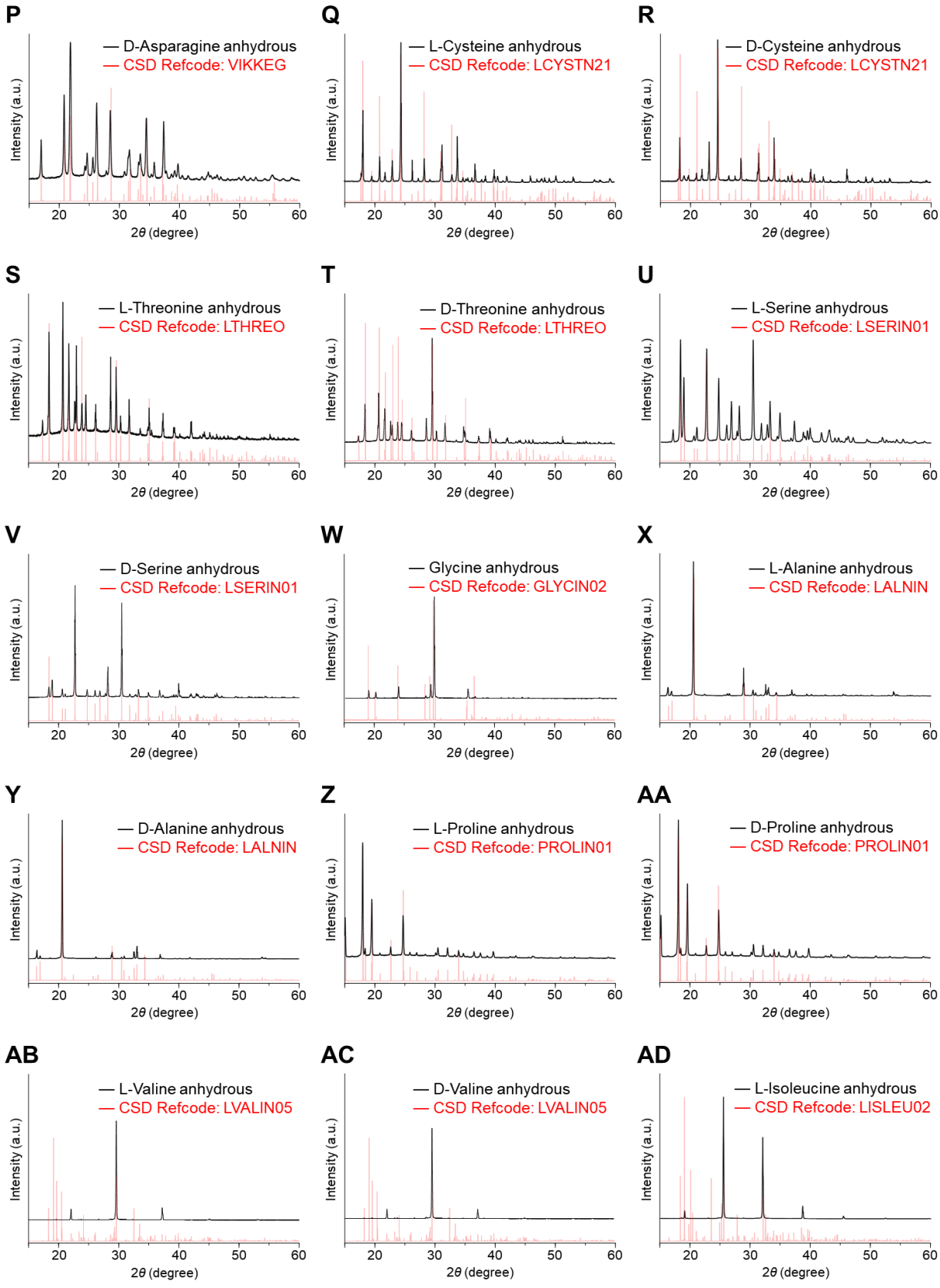
P
— D-Asparagine anhydrous
— CSD Refcode: VIKKEG
Q
— L-Cysteine anhydrous
— CSD Refcode: LCYSTN21
R
— D-Cysteine anhydrous
— CSD Refcode: LCYSTN21
S
— L-Threonine anhydrous
— CSD Refcode: LTHREO
T
— D-Threonine anhydrous
— CSD Refcode: LTHREO
U
— L-Serine anhydrous
— CSD Refcode: LSERIN01
V
— D-Serine anhydrous
— CSD Refcode: LSERIN01
W
— Glycine anhydrous
— CSD Refcode: GLYCIN02
X
— L-Alanine anhydrous
— CSD Refcode: LALNIN
Y
— D-Alanine anhydrous
— CSD Refcode: LALNIN
Z
— L-Proline anhydrous
— CSD Refcode: PROLIN01
AA
— D-Proline anhydrous
— CSD Refcode: PROLIN01
AB
— L-Valine anhydrous
— CSD Refcode: LVALIN05
AC
— D-Valine anhydrous
— CSD Refcode: LVALIN05
AD
— L-Isoleucine anhydrous
— CSD Refcode: LISLEU02
Intensity (a.u.)
2θ (degree)
20
30
40
50
60

(Continued)

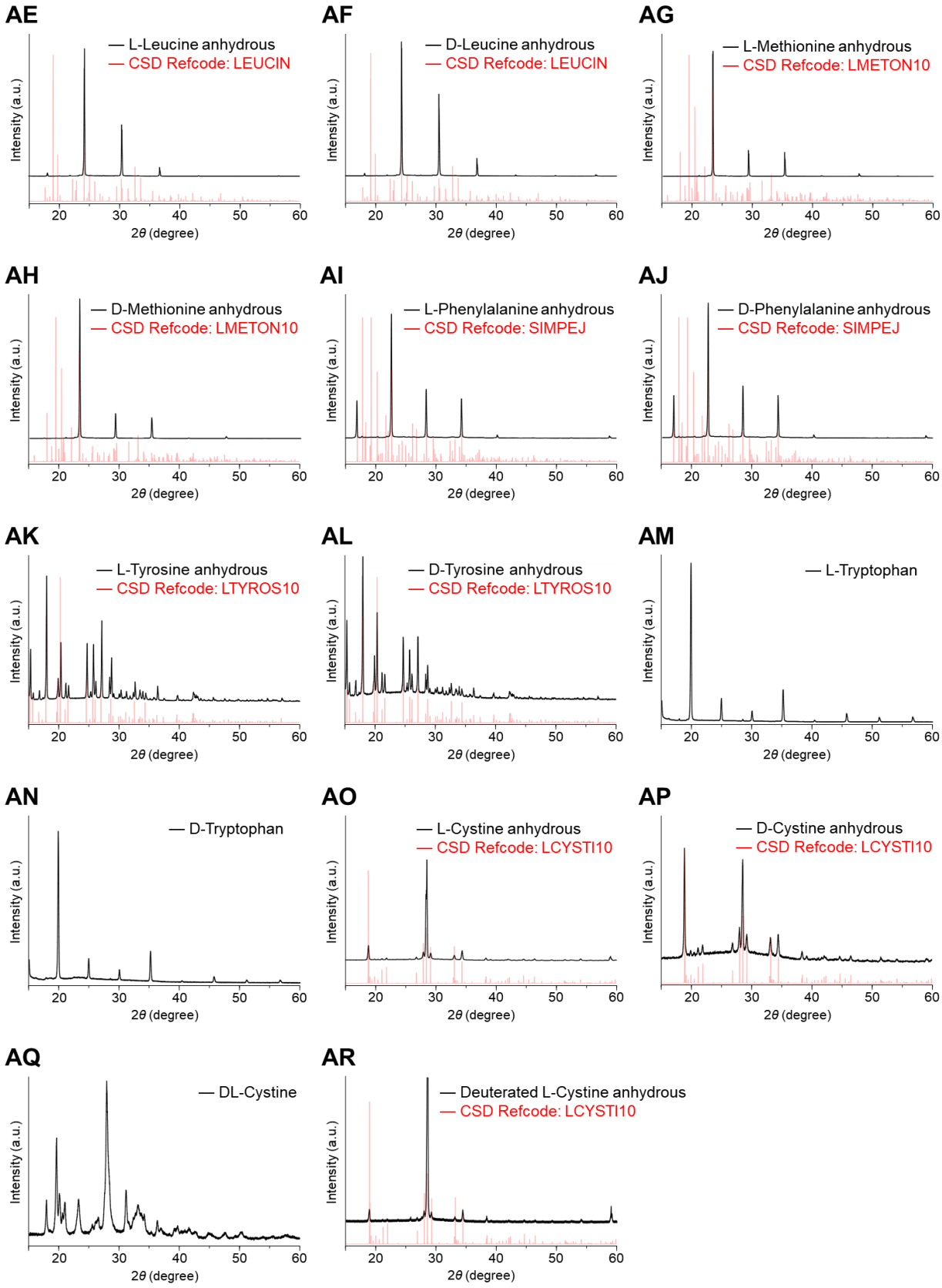
AE
— L-Leucine anhydrous
— CSD Refcode: LEUCIN
AF
— D-Leucine anhydrous
— CSD Refcode: LEUCIN
AG
— L-Methionine anhydrous
— CSD Refcode: LMETON10
AH
— D-Methionine anhydrous
— CSD Refcode: LMETON10
AI
— L-Phenylalanine anhydrous
— CSD Refcode: SIMPEJ
AJ
— D-Phenylalanine anhydrous
— CSD Refcode: SIMPEJ
AK
— L-Tyrosine anhydrous
— CSD Refcode: LTYROS10
AL
— D-Tyrosine anhydrous
— CSD Refcode: LTYROS10
AM
— L-Tryptophan
AN
— D-Tryptophan
AO
— L-Cystine anhydrous
— CSD Refcode: LCYSTI10
AP
— D-Cystine anhydrous
— CSD Refcode: LCYSTI10
AQ
— DL-Cystine
AR
— Deuterated L-Cystine anhydrous
— CSD Refcode: LCYSTI10
Intensity (a.u.)
2θ (degree)
20
30
40
50
60

Figure 4-2 Powder XRD patterns of crystals from proteinogenic AAs and dipeptides. (**A–C**) arginine (Arg), (**D, E**) histidine (His), (**F, G**) lysine (Lys), (**H, I**) glutamic acid (Glu), (**J, K**) aspartic acid (Asp), (**L, M**) glutamine (Gln), (**N–P**) asparagine (Asn), (**Q, R**) cysteine (Cys), (**S, T**) threonine (Thr), (**U, V**) serine (Ser), (**W**) glycine (Gly), (**X, Y**) alanine (Ala), (**Z, AA**) proline (Pro), (**AB, AC**) valine (Val), (**AD**) isoleucine (Ile), (**AE, AF**) leucine (Leu), (**AG, AH**) methionine (Met) , (**AI, AJ**) phenylalanine (Phe), (**AK, AL**) tyrosine (Tyr), (**AM, AN**) tryptophan (Trp), and (**AO–AR**) cystine (CYT). Note that abbreviations for cysteine and cystine are not the same, Cys and CYT, respectively. Experimental data were shown in black, and the reference data, collected from CCDC, are shown in red with their CSD reference codes (refcodes). All AAs except for lysine were recrystallized as described in **Table 3.1**. Reproduced from ref.(*2*).

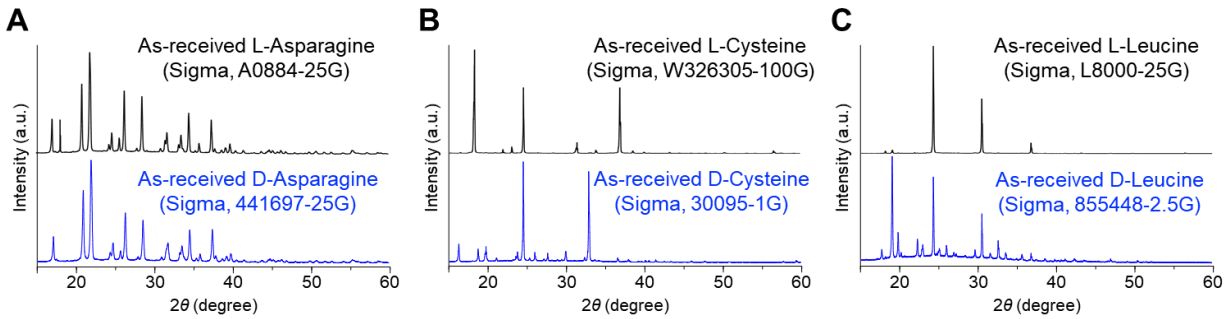

Figure 4-3 Powder XRD patterns of as-received *L*- and *D*-enantiomers of Asp, Cys, and Leu. Crystalline phases of many as-received crystals are different and especially between *L*- and *D*-enantiomers due to their different chemical production processes. Most *L*-enantiomers of AAs are natural whereas *D*-enantiomers of AAs are chemically synthesized, and therefore have different impurities and structures. Reproduced from ref.(*2*).

As-received crystals

Recrystallized crystals

A1

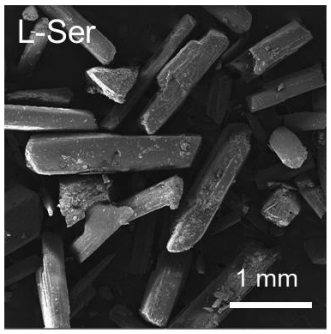

Shape:
Rods

Avg. Long axis:
1.599 mm
Avg. Short axis:
0.367 mm

A2

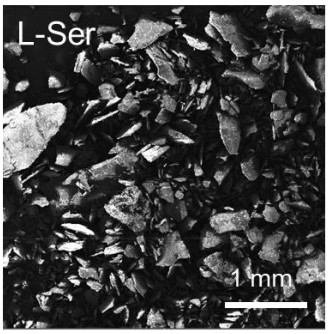

Shape:
Plates

Avg. Long axis:
0.384 mm
Avg. Short axis:
0.236 mm

B1

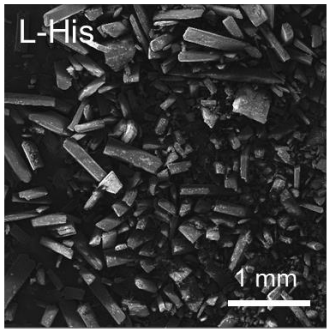

Shape:
Rods

Avg. Long axis:
1.013 mm
Avg. Short axis:
0.285 mm

B2

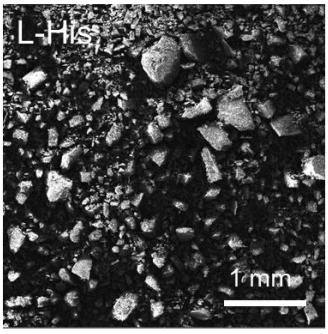

Shape:
Blocks

Avg. Long axis:
0.283 mm
Avg. Short axis:
0.178 mm

C1

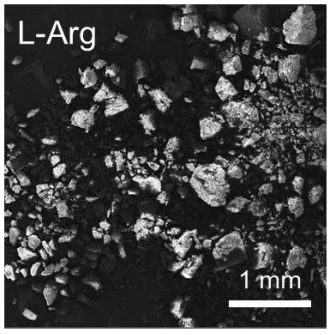

Shape:
Mixed

Avg. Long axis:
0.121 mm
Avg. Short axis:
0.097 mm

C2

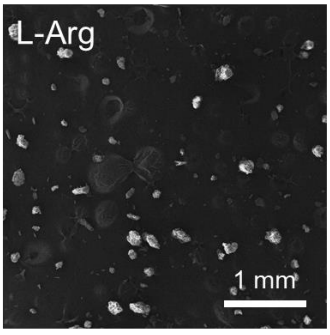

Shape:
Blocks

Avg. Long axis:
0.246 mm
Avg. Short axis:
0.192 mm

(Continued)

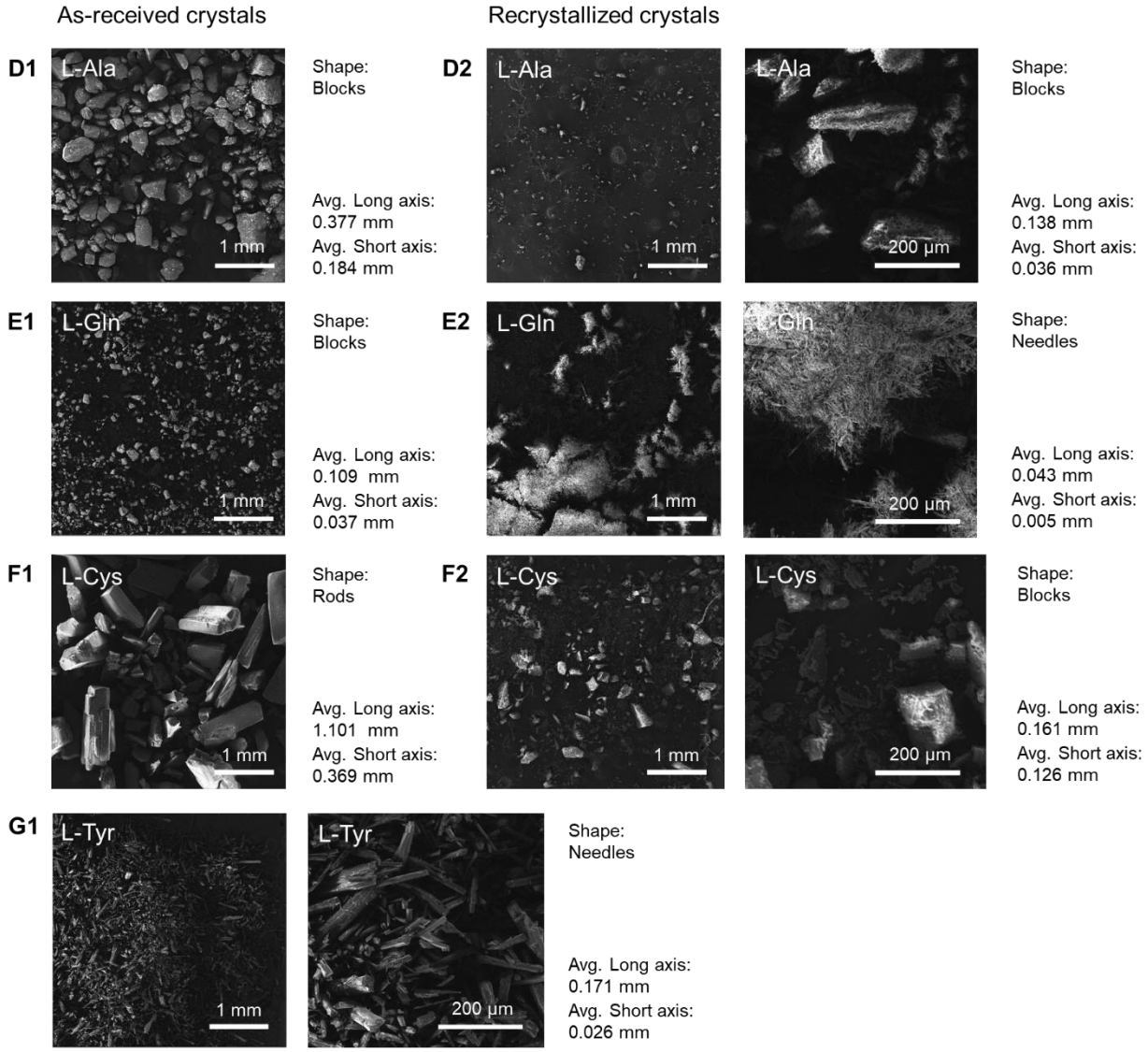

Figure 4-4 SEM images of AA crystals before and after recrystallization. Crystals in as-received samples have larger sizes than those after recrystallization. Crystals larger than 100 µm need to be ground and dispersed into a slurry to obtain accurate THz spectra. SEM images of (**A1** and **A2**) as-received and recrystallized *L*-serine. (**B1** and **B2**) As-received and recrystallized *L*-histidine. (**C1** and **C2**) As-received and recrystallized *L*-arginine. (**D1** and **D2**) As-received and recrystallized *L*-alanine. (**E1** and **E2**) As-received and recrystallized *L*-glutamine. (**F1** and **F2**) As-received and recrystallized *L*-cysteine. (**G1**) As-received *L*-tyrosine. Reproduced from ref.(*2*).

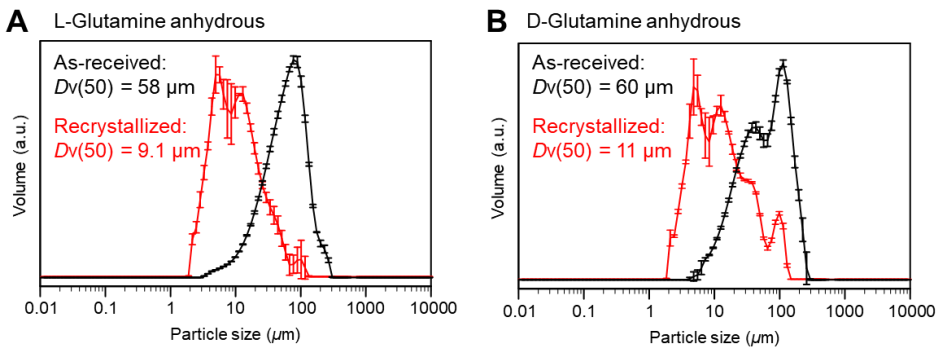

Figure 4-5 Size distribution analyses of *L*- and *D*-glutamine powders before and after recrystallization. The particle sizes of as-received and recrystallized powders from anhydrous (**A**) *L*- and (**B**) *D*-glutamine were measured in triplicate and averaged. *D*v(50) refers to the median diameter in volume or the particle size that splits the distribution of volume with half above and half below this diameter. Reproduced from ref.(*2*).

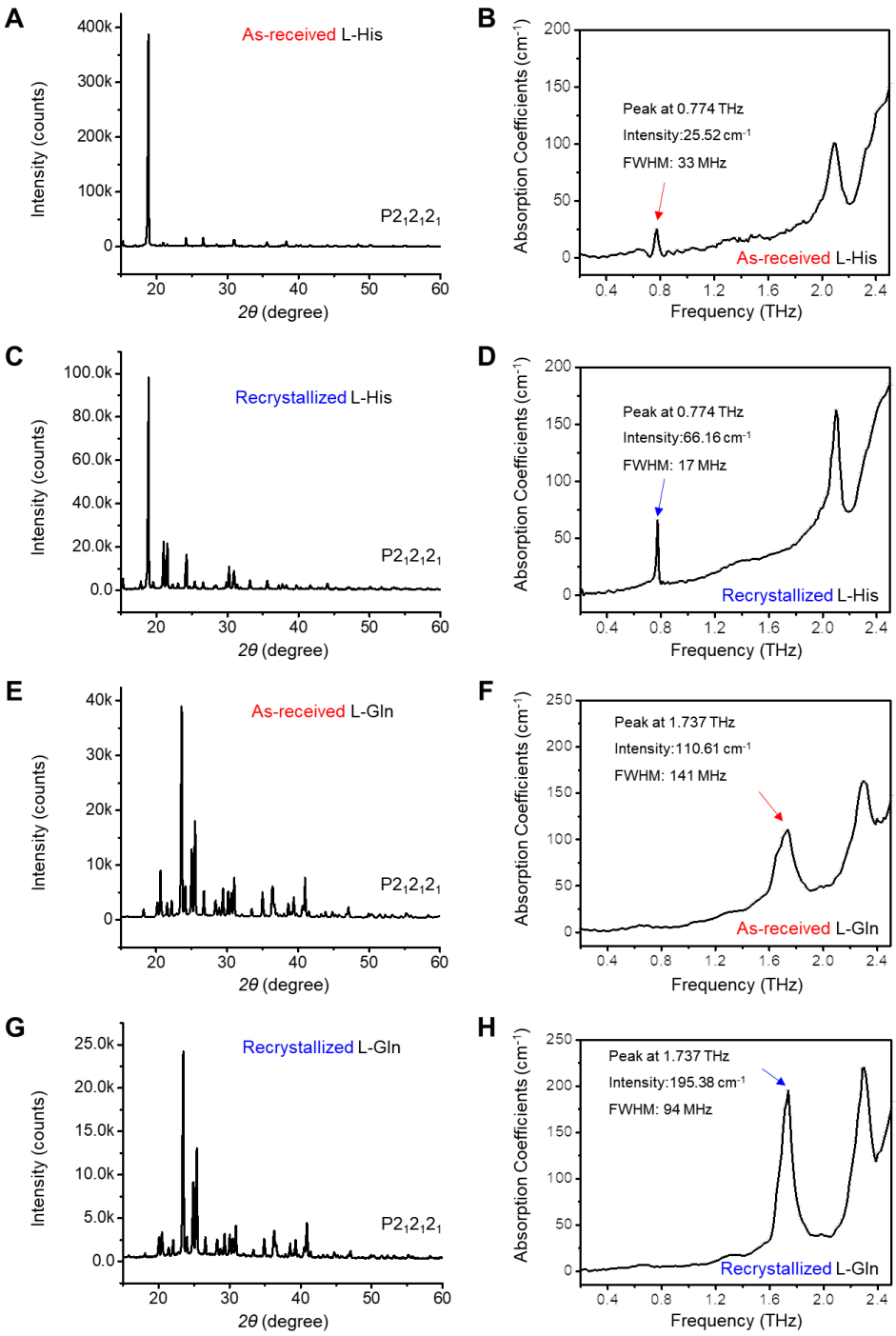

Figure 4-6 THz absorption (TA) spectra of *L*-histidine and *L*-glutamine for samples with different degrees of crystallinity. XRD (**A** and **C**) and averaged TA spectra (**B** and **D**) of as-received and recrystallized *L*-histidine. XRD (**E** and **G**) and averaged TA spectra (**F** and **H**) of as-received and recrystallized *L*-glutamine. After recrystallization, the average size of the crystals is generally smaller; stronger and sharper TA peaks are observed as a result. Reproduced from ref.(*2*).

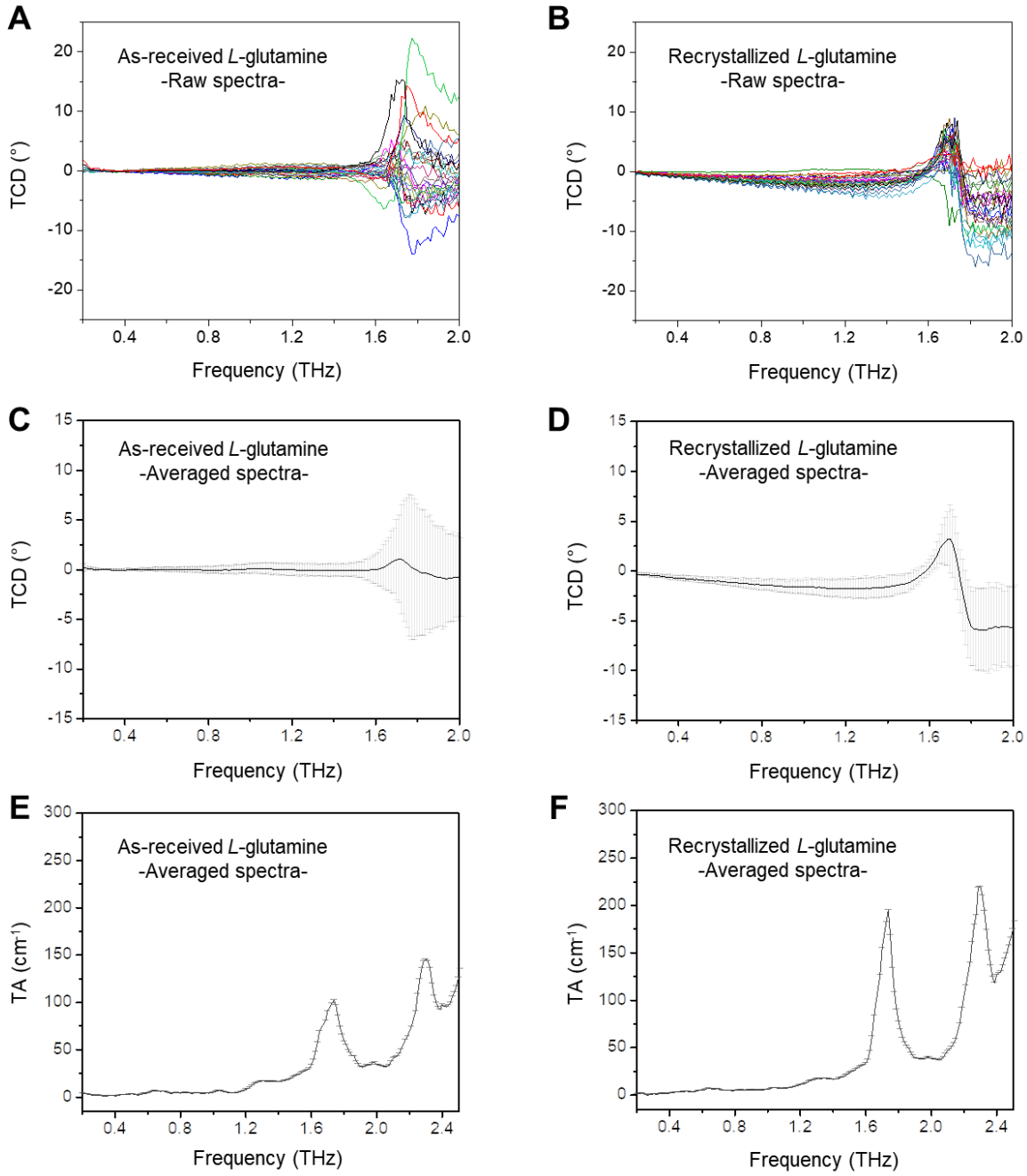

Figure 4-7 The effects of recrystallization on TCD spectra. (**A** and **B**) TCD raw spectra of as-received and recrystallized *L*-glutamine at each of 25 different positions. (**C** and **D**) averaged TCD spectra with standard deviation of as-received *L*-glutamine (Sigma, G3126-100G) and recrystallized one. (**E** and **F**) averaged TA spectra with standard deviation of as-received *L*-glutamine (Sigma, G3126-100G) and recrystallized samples. Reproduced from ref.(*2*).

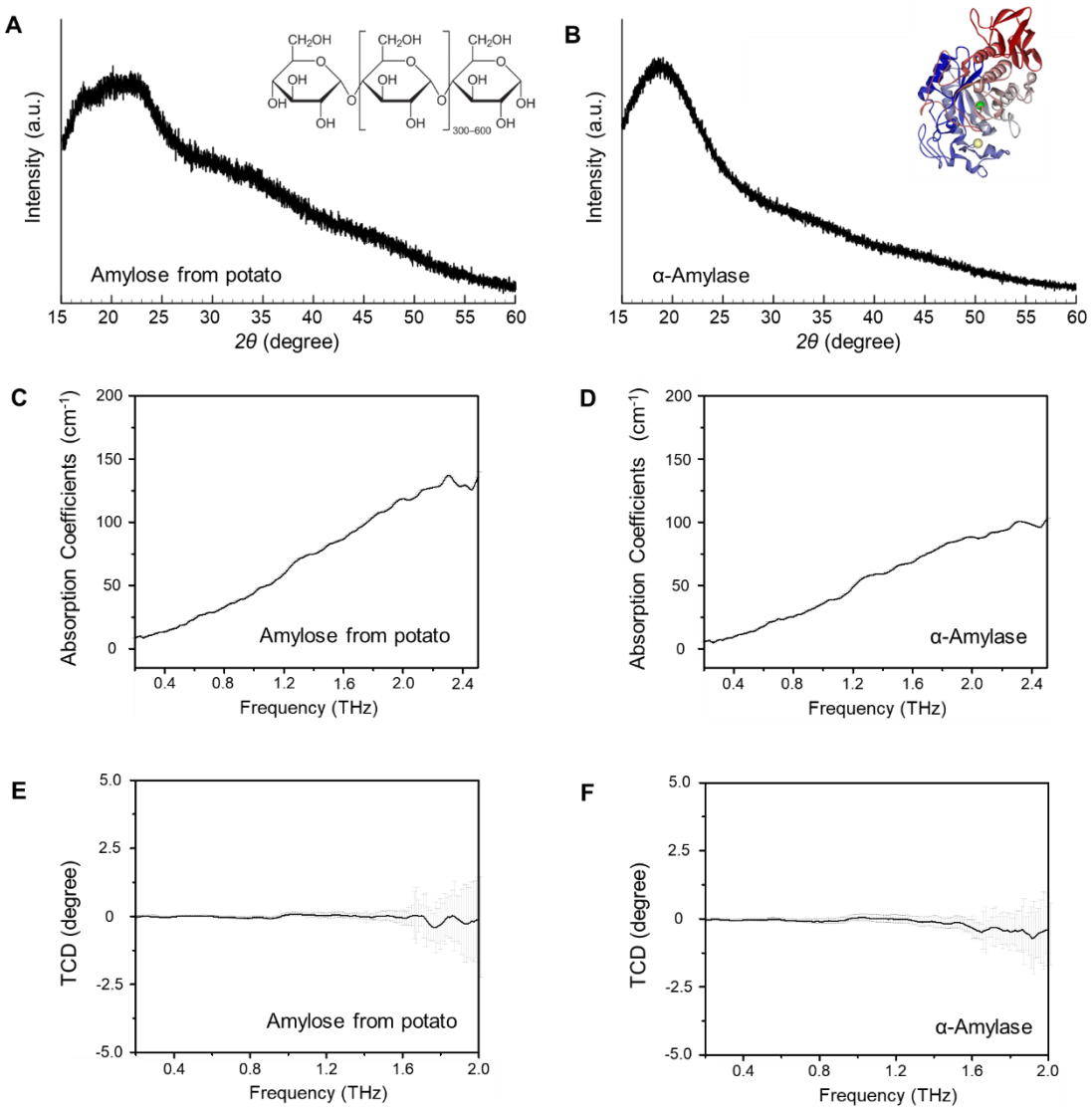

Figure 4-8 TA and TCD spectra from amorphous biomolecules. (**A** and **B**) XRD data of amylose and α-amylase, respectively. Both charts are featureless, indicating their amorphous structures. (**C** and **D**) averaged TA spectra with standard deviations of amylose and α-amylase, respectively. (**E** and **F**) averaged TCD spectra with standard deviations of amylose and α-amylase, respectively. Reproduced from ref.(*2*).

4.4 Hyperspectral THz-TDP setup

To obtain high quality spectra of the biocrystals, we developed a hyperspectral THz setup with motorized XY scanning (**Figure 4-9**). This setup enables accurate measurements and identification of chiral phonons by acquiring spatially resolved TA, TCD, and THz optical rotation dispersion (TORD) spectra (**Figure 4-9**) in concentrated slurries containing ~ 50 wt% of recrystallized AA crystals in mineral oil (MO). The random orientation of the densely packed microcrystals in the slurries eliminates spectral distortions typically observed in pressured and pelleted samples arising from birefringence and linear dichroism (**Figure 4-9A,B**). Similar problems were reported for circular dichroism measurements in the visible range (*95*, *96*).

A quartz sandwich cell with a 100 μm spacer maintaining the uniformity of the optical wavefront and sample thickness was utilized to obtain high signal-to-noise ratios. Also important was maintaining crystal phase purity and AA crystal sizes below 50 μm, which was achieved by careful recrystallization of the commercial chemicals (**Figure 4-1**and **Table 4-1,Table 4-2**). Their crystalline phase and size distributions were confirmed by powder X-ray diffraction (XRD) analysis, scanning electron microscopy (SEM) and particle size analyzers, respectively (**Figure 4-9C,D** and **Figure 4-2** to **Figure 4-5**

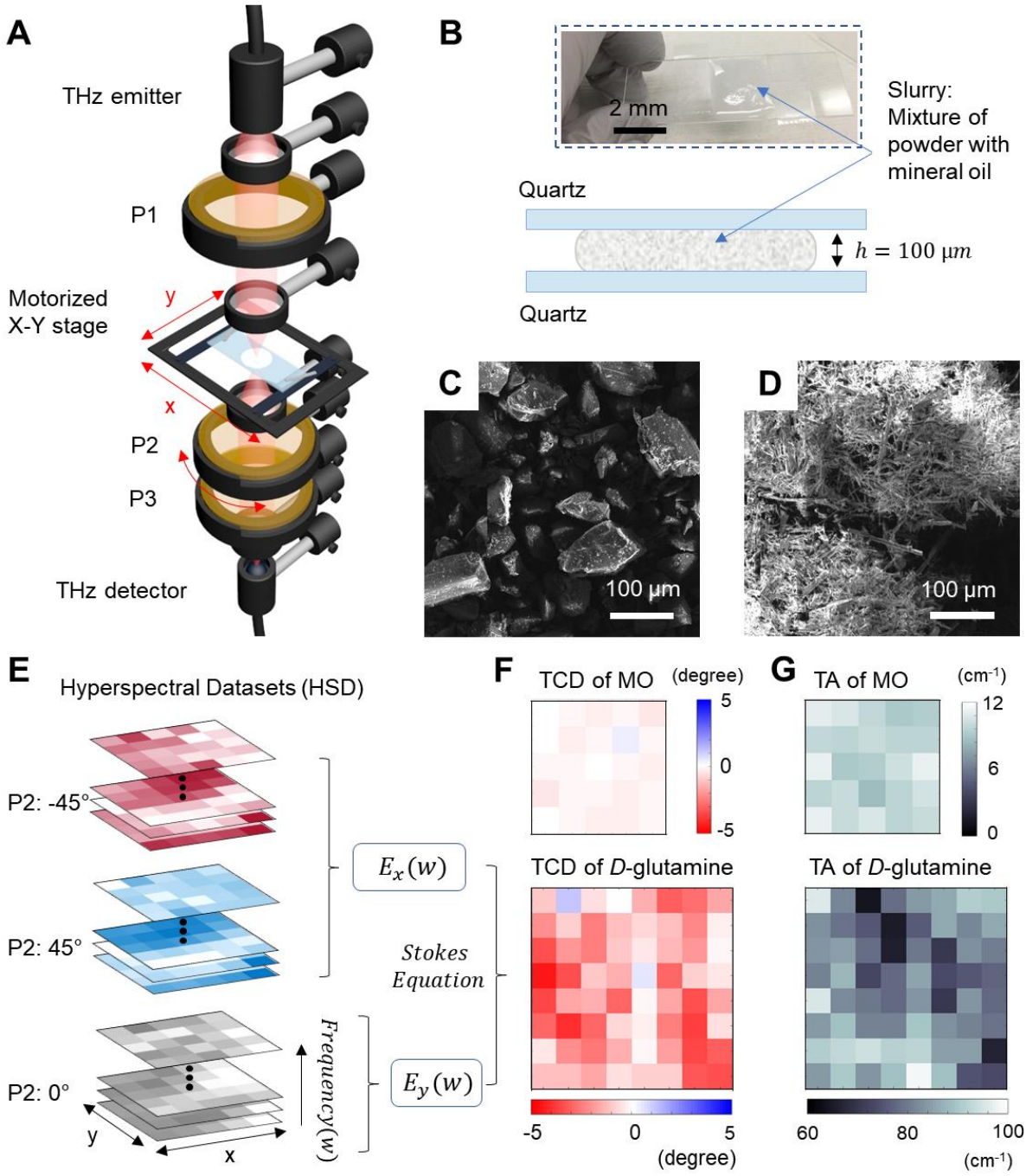

Figure 4-9 Hyperspectral THz-TDP set-up for observation of chiral phonons in AA microcrystals. (**A**) Schematics of the THz-TDP setup. Three wire grid polarizers (P1, P2 and P3) were used to analyze polarization states of the beam after passing through the sample. A motorized X-Y stage was used for mapping. (**B**) Photograph and schematic of sandwich quartz cell with slurry mixtures, respectively. (**C** and **D**) SEM images of before (C) and after (D) recrystallization of *L*-glutamine. (**E**) Fourier-transformed hyperspectral datasets of electric fields were measured by three different polarization measurements for each pixel. $E_x(w)$ is obtained from the

measurements of 45° and -45° for the P2 polarizer and $E_y(w)$ is from 0°, which is along the *y* direction. (**F**) Example of TCD mapping for reference mineral oil and *D*-glutamine at 1.69 THz, respectively. (**G**) Example of TA mapping for reference mineral oil and *D*-glutamine at 1.69 THz, respectively. Reproduced from ref.(*2*).

4.4.1 Hyperspectral THz-TDP Methodology

Hyperspectral terahertz time-domain polarimetry (THz-TDP) was used to measure the chiroptical responses of the AA samples. The generation and detection of the terahertz waveform were accomplished with a standard time-domain terahertz spectrometer (TeraSmart, Menlo Systems) using photoconductive antennas with a pulsed laser at 1560 nm. Same Tera15-FC antenna modules were used as emitter and detector, respectively. The four identical lenses (TPX50, Menlo Systems) made of TPX polymer (polymethylpentene) with a diameter of 1.5" and a focal length of 50 mm were used to make collimated THz rays. Sample scanning in the THz focal plane was achieved by motorized XY stage. Three linear polarizers were used to determine the optical rotatory dispersion, TORD, (θ) and circular dichroism, TCD, (η) of arbitrarily polarized THz waves (*1*, *38*). Here, micro-patterned gold strips on the parylene C film were used for wire grid polarizers exhibiting high extinction ratio over the THz range (*1*, *97*).

4.4.2 Configuration of Three polarizers (P1, P2 and P3)

Orientation of the linear polarized THz beam from the THz emitter was fixed at a horizontal orientation to the optical breadboards (defined here as the *x* axis, **Figure 4-10**) while the THz detector was fixed at a vertical orientation (defined as the *y* axis) (*1*). The first polarizer (P1) was placed in front of the emitter and its transmission direction (perpendicular to the wire grid orientation) was fixed to the *x* axis. The third polarizer (P3) was placed right before the THz emitter

and its transmission direction was fixed to the *y* axis, making it cross-polarized to P1 and the emitter. The second polarizer (P2) was placed between P1 and P2 and was rotated to different orientations to determine the complete polarization state of the transmitted electric field (*1*).

When the P2 transmission axis was along the *y* direction (defined as 0°), it was co-polarized with P1 and the *y*-component of the transmitted electromagnetic waves through sample $E_y(t)$ was measured. The *x*-component $E_x(t)$ was readily measured by rotating the orientation of P2 transmission axis to +45° and -45° and calculated by the subtraction of the two *x*-components $E_{+45^\circ}(t)$ and $E_{-45^\circ}(t)$. Because any arbitrary electric field can be decomposed into two perpendicular components, polarization states such as the TORD and TCD can be fully determined with three measurements (*1*, *38*).

4.4.3 Calculation of Electric fields and Stoke equations for TA, TORD and TCD

Obtaining terahertz absorption coefficients (TA), optical rotational dispersion (TORD) and circular dichroism (TCD) is started with calculation of the *x* and *y* components of the electric field as stated elsewhere (*1*). The *x*-component of the electric field can be calculated by

$$E_x(t) = E_{+45^\circ}(t) - E_{-45^\circ}(t) \quad (1)$$

where $E_{+45^\circ}(t)$ and $E_{-45^\circ}(t)$ are the time-domain electric field for the orientation of polarizer P2, where transmission axes are at +45° and -45° relative to the *y*-axis, respectively.

Complex frequency-domain electric field spectra are obtained using fast Fourier transform (FFT) from the electric fields measured in the time-domain as follows:

$$\tilde{E}_x = \tilde{E}_x(\omega) = FFT\{E_x(t)\}$$
$$\tilde{E}_y = \tilde{E}_y(\omega) = FFT\{E_y(t)\} \quad (2)$$

The transmittance spectrum of the sample and refence can be calculated from two electric fields

$$T_s = \sqrt{\left|\tilde{E}_x\right|^2 + \left|\tilde{E}_y\right|^2} \quad (3)$$

$$T_{ref} = \sqrt{\left|\tilde{E}_{ref,x}\right|^2 + \left|\tilde{E}_{ref,y}\right|^2} \quad (4)$$

Here, T_s is transmittance through a quartz sandwich cell with slurry, mixture with highly concentrated sample powder with mineral oil (MO), and T_{ref} is transmittance through a quartz sandwich cell with just MO as a reference.

Accordingly, TA can be obtained by

$$TA = -\frac{\ln(T_s/T_{ref})}{d_s} \quad (5)$$

where d_s is the thickness of the sample. Here, the measured thickness for all samples is 100 μm (*1*). For the calculation of relative TA, normalization by thickness was not achieved.

Since the polarization of the incident THz beam is linear and emitter and detector are cross-polarized, TORD and TCD can be calculated directly by the measured THz spectra of $\tilde{E}_s = \begin{pmatrix} \tilde{E}_x \\ \tilde{E}_y \end{pmatrix}$ using Stokes equations. The four Stokes parameters are defined as

$$\begin{aligned} S_0 &= \tilde{E}_x \tilde{E}_x^* + \tilde{E}_y \tilde{E}_y^* \\ S_1 &= \tilde{E}_x \tilde{E}_x^* - \tilde{E}_y \tilde{E}_y^* \\ S_2 &= \tilde{E}_x \tilde{E}_y^* + \tilde{E}_y \tilde{E}_x^* \\ S_3 &= i(\tilde{E}_x \tilde{E}_y^* - \tilde{E}_y \tilde{E}_x^*) \end{aligned} \tag{6}$$

And the TORD and TCD can be calculated using Stokes parameters as follows:

$$\begin{aligned} TORD &= \frac{1}{2} tan^{-1}\left(\frac{S_2}{S_1}\right), \quad -\frac{\pi}{2} \le TORD \le \frac{\pi}{2} \\ TCD &= \frac{1}{2} sin^{-1}\left(\frac{S_3}{S_0}\right), \quad -\frac{\pi}{4} \le TCD \le \frac{\pi}{4} \end{aligned} \tag{7}$$

4.4.4 TCD mapping Method and the Reference sample

As mentioned above, since many samples have linear polarization effects such as linear birefringence, an averaging process of the THz spectra from different orientations of the randomly dispersed small-sized crystals is necessary to eliminate linear birefringence and measure signals only originating from the chirality. Here, not only each single spot is measured more than 400 times for an accumulated averaging process, but also 5 to 100 spatially different spots were typically measured for calculation of averaged values and standard deviations. Using a high

precision motorized XY positioning stage, measurements of exactly the same spot for every polarization state (i.e. three different orientations of the P2 polarizer angles: -45°, 0°, 45°) were achieved. The algorithms for hyperspectral image processing and calculation of Stokes equations for each pixel were verified by a known chiral kirigami sample as a reference. Details of the reference kirigami sample can be found in elsewhere (*1*). Briefly, the kirigami sample is made from parylene sheet that was patterned with straight cuts in a face-centred rectangular lattice. Herringbone-patterned thin layers of chromium and gold are deposited on the Parylene C using electron beam evaporator (Enerjet evaporator) after a standard photolithography process (MA/BA6 Mask/Bond aligner, Suss Microtec). Exactly the same protocols and dimensions of the kirigami cuts were used for this study. The slant angle of the gold strips was 30º. The kirigami sample is designed to have a topologically equivalent helix structure with patterned gold strips on the curved polymer sheet. Here, to show our microscopic THz-TDP's mapping capability, kirigami samples with two chiral domains were chosen and tested. As expected, distinct mirror-like TCD peaks from each domain and zero-TCD peaks from the achiral domain boundary were successfully measured even with very short accumulation times (~2s for each pixel), showing the high signal-to-noise level performance and high accuracy of this mapping system (**Figure 4-11**).

4.4.5 TA and TCD spectra of all AA Microcrystals

TA and TCD spectra were measured by equations (5) and (8), respectively. The reference sample for TA is a quartz sandwich cell with MO as discussed earlier. 25 different spots were measured and averaged to obtain TA and TCD. MO was chosen as a host material for the slurry because it shows high transparency across the THz range and non-chiroptical responses. The raw data of transmission, TA, TCD and TORD of MO are shown in **Figure 4-12**. Likewise, results of

all AA crystals are shown in **Figure 4-13**. Most of the multiple reflection etalon effects from quartz sandwich were eliminated by dividing the data of reference (quartz with MO) from the samples. To remove water vapor peaks, an algorithm was used to remove the data at nine points; nine peaks of water are found at 1.10, 1.16, 1.41, 1.66, 1.67, 1.71, 2.16, 2.20, 2.22 THz. Savitzky-Golay (SG) filter for 3 polynomial order was applied to remove the etalon effect from the quartz substrates. To capture low-intensity peak features in the low frequency range (peaks below 1 THz), the data at the exact peak positions were excluded for the SG processing. Averaged TA spectra were cross-checked with some of the previously reported data to confirm and justify our slurry method with a data processing algorithm (**Table 4-3**). Almost identical spectra were found when the AAs and the phase of the samples were matched.

4.4.6 Effect of Size of AA Crystals on the THz behavior

Recrystallization processes of crystals are of primary importance because of the following reasons:

(1) A homogeneous phase of a biological crystal is always required for proper linkage between phase and terahertz (THz) behavior.

(2) Identical crystalline phases of *L*- and *D*-enantiomers are needed for understanding chiroptical properties.

(3) Small (< 50 μm) diameter crystals are important to prevent scattering.

Since THz spectra from biological crystals are very sensitive to their phase, including various hydration states (*24*, *77*, *98*), obtaining single and homogeneous phases must be preceded to assign the TA and TCD properly. It should also be noted that the crystalline phases of many as-received

crystals are not homogeneous. Also, the phases of the *L*- and *D*-enantiomers are frequently different (**Figure 4-3**). This is probably due to their different chemical production processes.

The size of biological crystals affects their THz behavior. **Figure 4-4** shows SEM images of various AAs crystals before and after recrystallization. Mostly, the sizes of as-received crystals are larger than those of recrystallized samples. Crystals shown in the SEM images are from samples after recrystallization but before grinding. After confirming the size, we further ground the recrystallized crystals to obtain small (< 50 μm) crystals for proper THz spectra. We also conducted size distribution analyses (**Figure 4-5**) of crystals to measure their size more quantitatively. This revealed that the particle sizes become typically 3–5 times smaller after recrystallization than before, as similarly observed from SEM images.

Scattering effects from granular solids are well-known for TA in many references (*90*, *99*) but their effects on TCD are unknown. Here, we found when the size of the crystal is larger than 50 μm, it gets too close to the lower bound of the spectral window of interest (ca. 150 μm) and thus also severely affects optical activity due to Mie scattering, which introduces an unwanted glare that broadens the TCD signal and leads to poor resolution of the bands. Thus, the size of the biological crystals should be strictly controlled to be small (< 50 μm) to obtain proper TCD spectra and prevent linear polarization scrambling, i.e. linear birefringence and dichroism. We noticed that many as-received biological crystals exhibit TA and TCD spectra with very large deviations depending on the measurement positions due to their size and spatial and phase heterogeneity (**Figure 4-6** and **Figure 4-7**), resulting in less reliable spectral data.

In particular, when the size of the crystal is relatively large (>100 μm), lower intensity and broader peaks of TA are observed relative to those of smaller size crystals (**Figure 4-6**). This can be understood from the defect point of view. Normally, nanoparticles or smaller particles are

considered as having less defects and thus more perfect crystal lattices. Since the terahertz absorption probes phonon modes, high-quality crystal could have more propagation and it gives higher absorption coefficients.

Not only for TA, TCD is also strongly affected by the size of the crystals. When the size is larger, both the positive and negative sign of the TCD were frequently observed (**Figure 4-7**). This effect might arise from the waveguide effect from the edges of the large crystal where polarization of the THz beam could be guided or ellipticity of the large single crystal rather than the averaged circular dichroism from the random mixture of multi-crystals. After the recrystallization processes, however, these deviations typically became smaller as the size decreases with the homogeneous crystalline phase and clear cotton effects were observed in the TCD spectra (**Figure 4-7B and Figure 4-7D**). It is almost impossible to completely rule out linear polarization effects in the solid-state samples, but we strongly believe that the TCD spectra from small-sized crystals (after recrystallization) contain much less contribution from birefringence as we measure CD spectra in the visible range from chiral nanoparticles and superstructures (*100*, *101*).

4.4.7 Slurry samples for THz spectroscopy

The use of slurries in mineral oil (MO) (instead of dry pelleted samples obtained by compression of powders) was crucial for obtaining reproducible and accurate TA, TCD, and TORD spectra because:

(1) MO has low absorption in the 0.2 – 2.5 THz region and shows no optical activity, with near zero TCD and TORD over this range;

(2) Slurries minimize Mie scattering;

(3) Similarly for the conditions needed for reproducible and accurate spectroscopy in the visible range of spectra which require homogeneous solutions of molecules, slurries enable rotational averaging of microcrystals, enabling the observation of TCD and TORD;

(4) MO protects hydrophilic and hydroscopic microcrystals from environment contaminants, including water vapor;

(5) MO with appropriate viscosity and density yielded homogeneous crystals dispersions, filling gaps or voids and also spreading smoothly between quartz plates of the optical cells in order to make a flat beam front;

(6) In sharp contrast to pellets, slurries allow the control of the volumetric loading of AA crystals (concentration).

4.4.8 THz spectra from amorphous samples

All sharp spectral features disappear in the frequency range of interest in amorphous samples due to the random spatial distribution of vibrational motions (**Figure 4-8**). Similar phenomena were also observed in the previous studies using amorphous glucose and vitreous ice (*22*, *102*, *103*).

4.4.9 TA and TCD spectra of crystals of AAs having Similar Molecular Structures

A slight change in molecular structure of AAs greatly alters the THz signature of their crystals. For example, *L*-serine (**Figure 4-14F**) and *L*-cysteine (**Figure 4-14T**) differ only by one

atom - sulfur is replaced by oxygen in cysteine. Nevertheless, their TA and TCD spectra are dramatically different (*81*). Another example of a large change in the THz spectra with minimal change of chemical structure is glutamine (**Figure 4-14I**) vs asparagine (**Figure 4-14H**). Glutamine is one CH_2 unit longer than asparagine, but the THz spectra are again markedly different. The same can also be seen for glutamic acid (**Figure 4-14E**) and aspartic acid (**Figure 4-14D**). These results indicate that the structure of crystals rather than the single molecules is responsible for the observed spectral features.

4.4.10 TA and TCD spectra of DL-CYT and deuterated L-CYT

To confirm the attribution of both bands to chiral phonons, *DL*-CYT and deuterated *L*-CYT were tested. *DL*-AAs are known to crystallize in P1 or $P\bar{1}$ racemic space groups (*104*). Correspondingly, *DL*-CYT biocrystals show low-intensity peaks in TA and near-zero values in averaged TCD (**Figure 4-23A**). On the other hand, deuterated *L*-CYT shows a red-shift of the second absorption peak in TA (normal: 1.51 THz; deuterated: 1.48 THz, P-value < 0.01), while other features remain the same. While the effect is weak in TA, it is stronger in the TCD spectrum manifesting as a 2.3-fold reduction of the magnitude and a 1.3-fold increase in the width (**Figure 4-23B**), showing remarkably high detection sensitivity.

4.4.11 TA and TCD spectra of Various Dipeptide Biocrystals

The library of THz fingerprints from basic AAs to complex proteins and other biomolecular complexes would open a new horizon of THz bioinformatics. In addition to AAs, registering high

quality spectra of dipeptides would be the first step toward THz bioinformatics. Also, several dipeptides are physiologically and commercially significant (*105*). Thus, TA and TCD spectra of dipeptides, including Cys-Cys, Ala-His, Ala-Ala, Ala-Tyr, Ala-Gln and Gly-Gly (**Figure 4-18B** and **Figure 4-19**) were acquired. As expected, TA and TCD from dipeptides could not be explained by simple combinations of THz results of two AAs. Since their intra- and intermolecular vibrations are totally different, their masses, spring coefficients and damping parameters, their resonance vibrations are dramatically changed. Simultaneously, the negative correlation between molecular weight and the position of the lowest resonance peak is observed (**Figure 4-14G**).

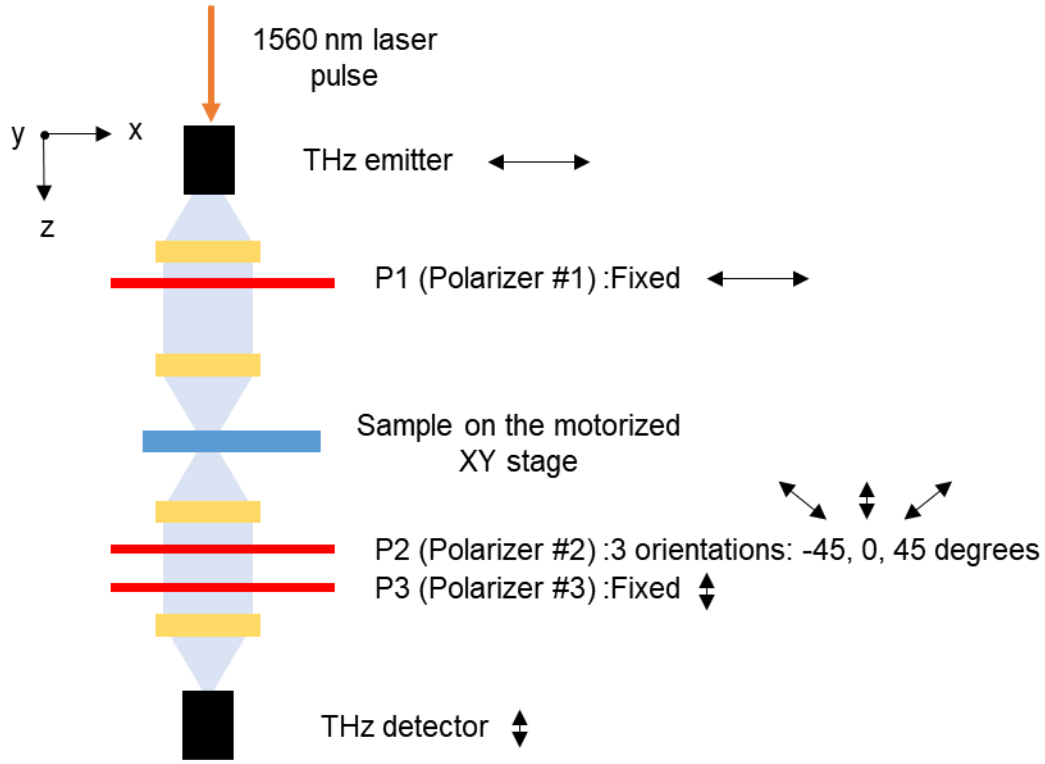

Figure 4-10 Schematic of hyperspectral THz-TDP setup. Three polarizers were used to determine polarization states of the THz beam after passing through the samples. Since P1 and P3 are cross-polarized, if there is no optical activity induced by the sample, the amplitude of $\tilde{E}_y$, the electric field in the y axis, is zero, and therefore TCD and TORD show near-zero values. Sample scanning in the THz focal plane was achieved using the motorized XY stage. Reproduced from ref.(*2*).

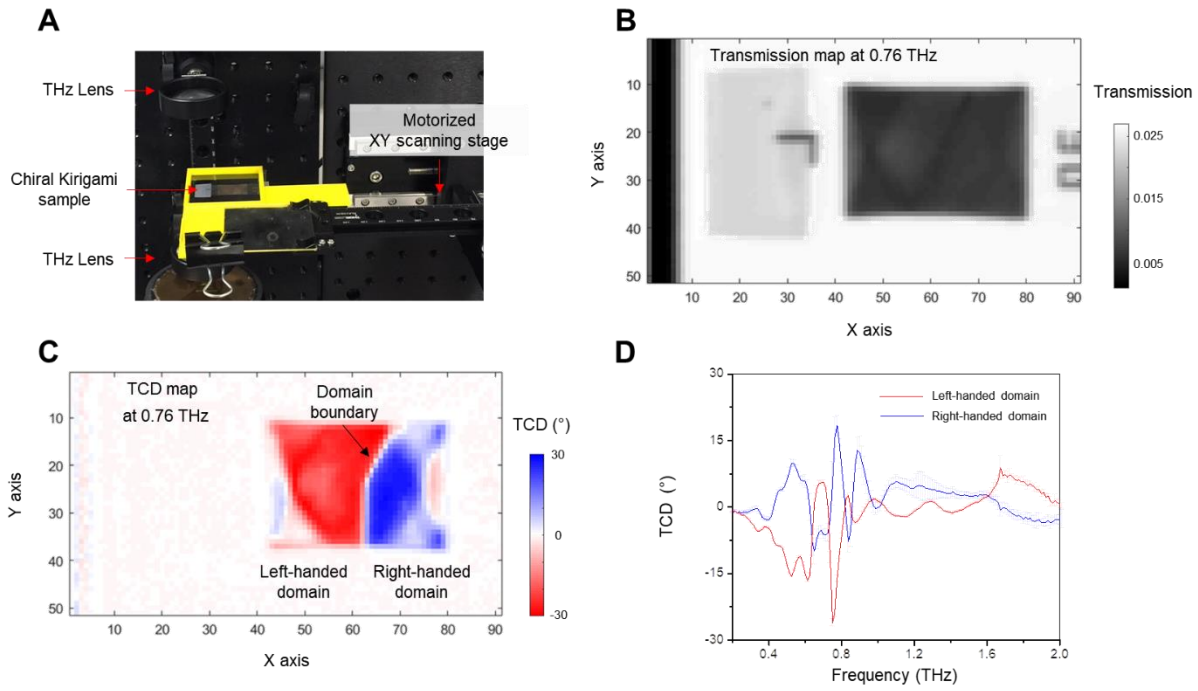

Figure 4-11 Mapping of chiral kirigami metamaterial as a reference sample. (**A**) Photograph of chiral kirigami sample (*26*) on the focal plane between two lenses. A stretched chiral kirigami sample is placed on the 3D printed holder with a motorized XY scanning stage. (**B**) Transmission map of kirigami sample at 0.76 THz. (**C**) TCD map of kirigami sample with two domains at 0.76 THz. The handedness of the kirigami sample was determined by the curvature of the 3D helical topology and the domain boundary was induced by mechanical defect. Here, we can clearly observe the hidden chiral domain by TCD mapping. (**D**) Mirror-symmetric averaged TCD spectra from red and blue domains, respectively. Reproduced from ref.(*2*).

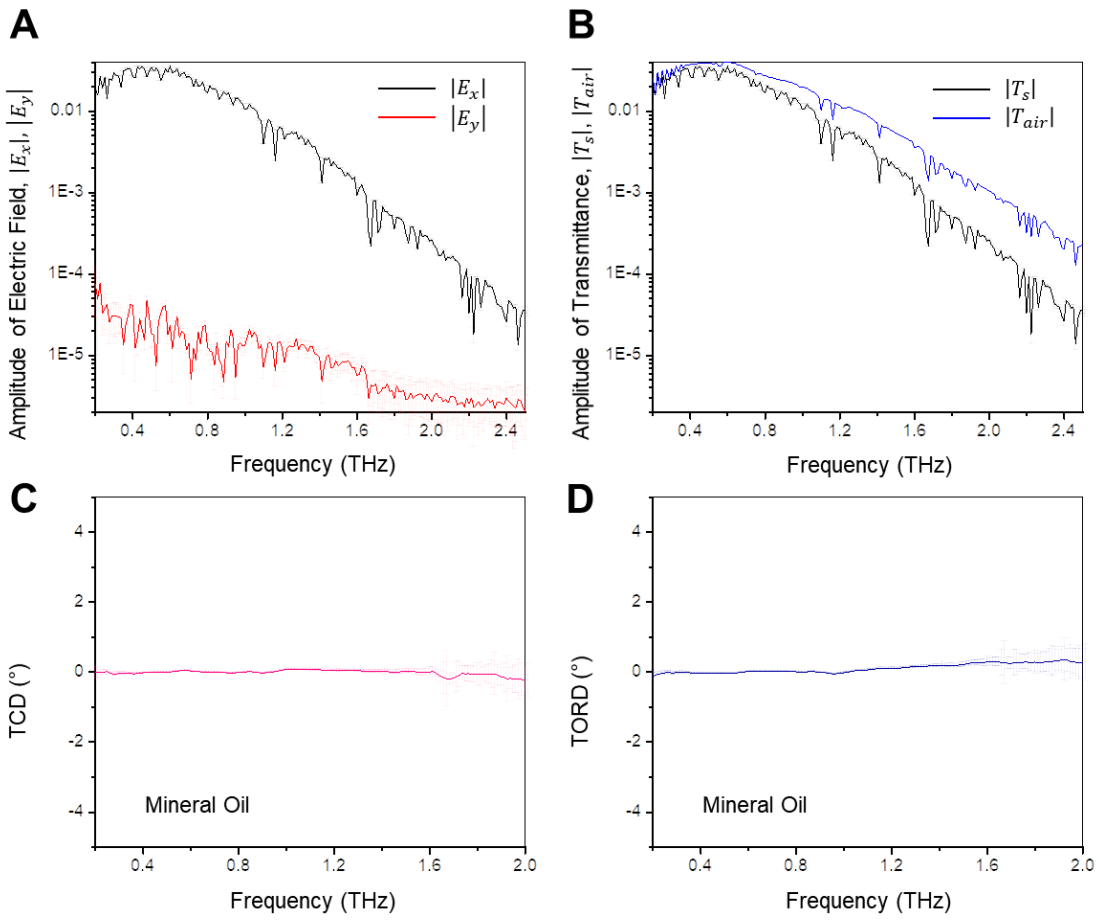

Figure 4-12 Spectral characteristics of mineral oil (MO) in the THz range. (**A**) Raw data of the averaged amplitude of the electric field from MO. (**B**) Raw data of averaged transmittance from MO and air, respectively, showing the high transparency of MO across the THz range. (**C** and **D**) Near-zero-TCD and TORD spectra from MO indicating there is no optical activity in this THz range, respectively. Reproduced from ref.(*2*).

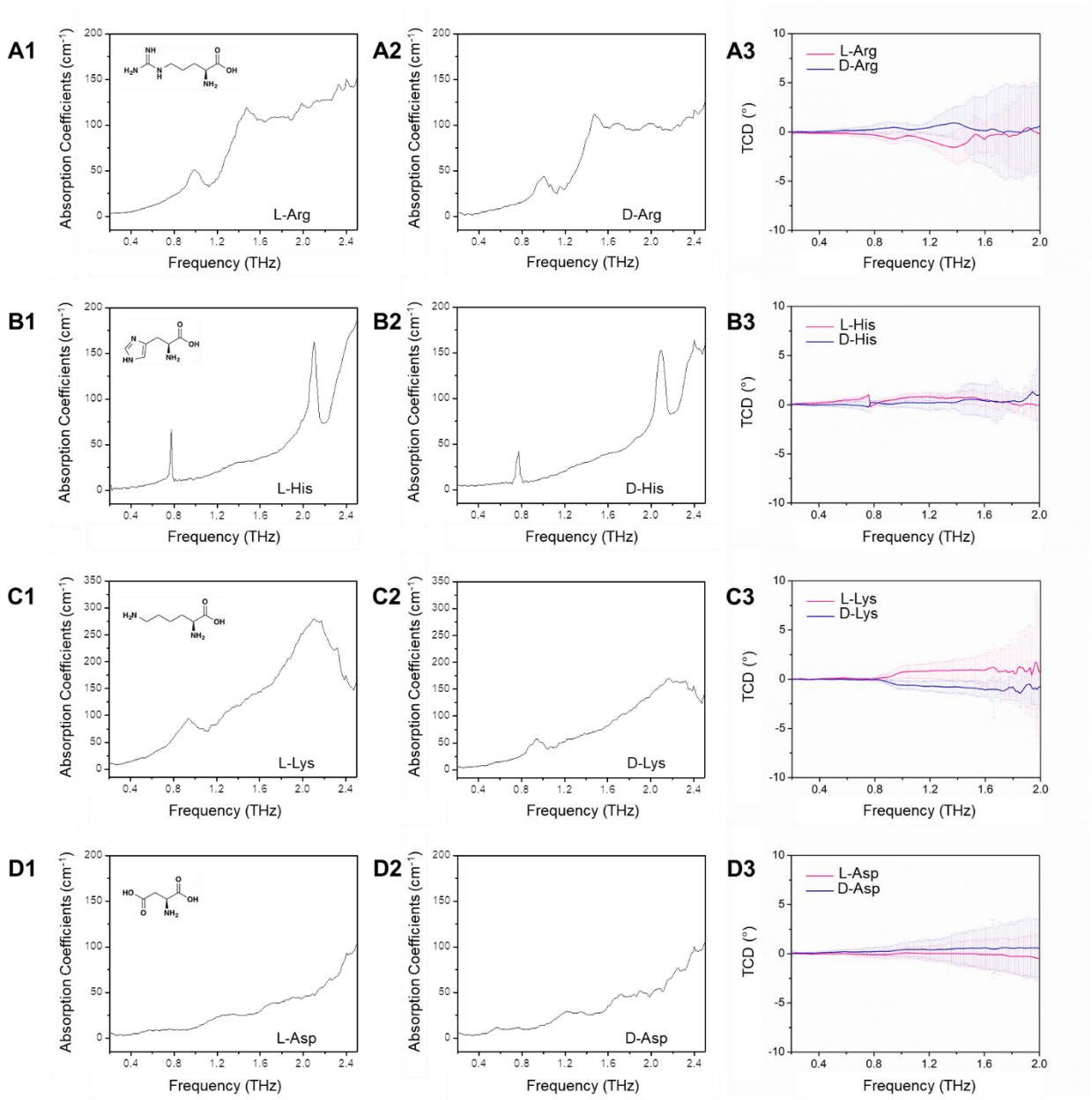
A1
Absorption Coefficients (cm-1)
L-Arg
Frequency (THz)
A2
Absorption Coefficients (cm-1)
D-Arg
Frequency (THz)
A3
L-Arg
D-Arg
TCD (°)
Frequency (THz)
B1
Absorption Coefficients (cm-1)
L-His
Frequency (THz)
B2
Absorption Coefficients (cm-1)
D-His
Frequency (THz)
B3
L-His
D-His
TCD (°)
Frequency (THz)
C1
Absorption Coefficients (cm-1)
L-Lys
Frequency (THz)
C2
Absorption Coefficients (cm-1)
D-Lys
Frequency (THz)
C3
L-Lys
D-Lys
TCD (°)
Frequency (THz)
D1
Absorption Coefficients (cm-1)
L-Asp
Frequency (THz)
D2
Absorption Coefficients (cm-1)
D-Asp
Frequency (THz)
D3
L-Asp
D-Asp
TCD (°)
Frequency (THz)

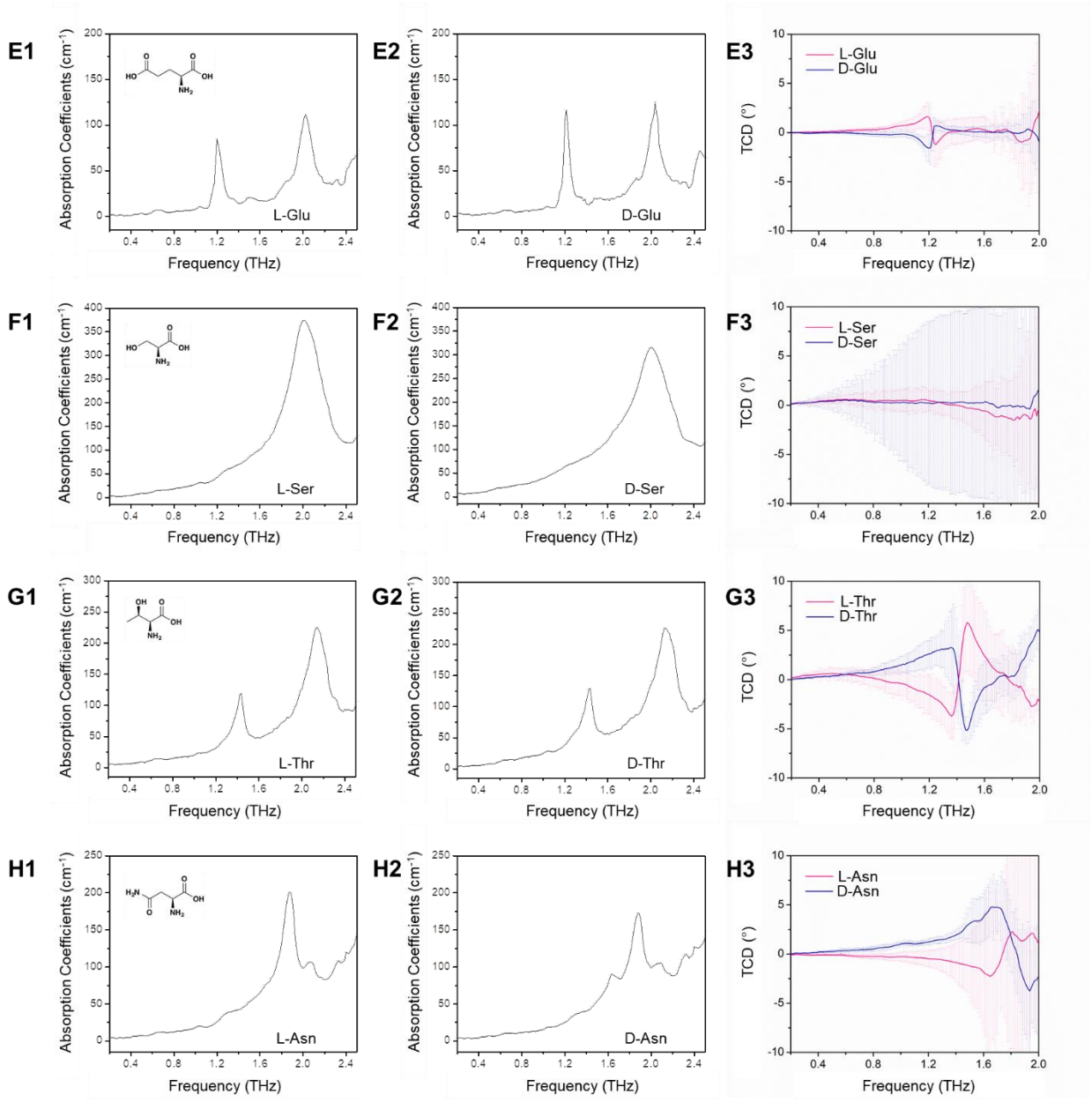
E1
Absorption Coefficients (cm⁻¹)
L-Glu
Frequency (THz)
E2
Absorption Coefficients (cm⁻¹)
D-Glu
Frequency (THz)
E3
L-Glu
D-Glu
TCD (°)
Frequency (THz)
F1
Absorption Coefficients (cm⁻¹)
L-Ser
Frequency (THz)
F2
Absorption Coefficients (cm⁻¹)
D-Ser
Frequency (THz)
F3
L-Ser
D-Ser
TCD (°)
Frequency (THz)
G1
Absorption Coefficients (cm⁻¹)
L-Thr
Frequency (THz)
G2
Absorption Coefficients (cm⁻¹)
D-Thr
Frequency (THz)
G3
L-Thr
D-Thr
TCD (°)
Frequency (THz)
H1
Absorption Coefficients (cm⁻¹)
L-Asn
Frequency (THz)
H2
Absorption Coefficients (cm⁻¹)
D-Asn
Frequency (THz)
H3
L-Asn
D-Asn
TCD (°)
Frequency (THz)

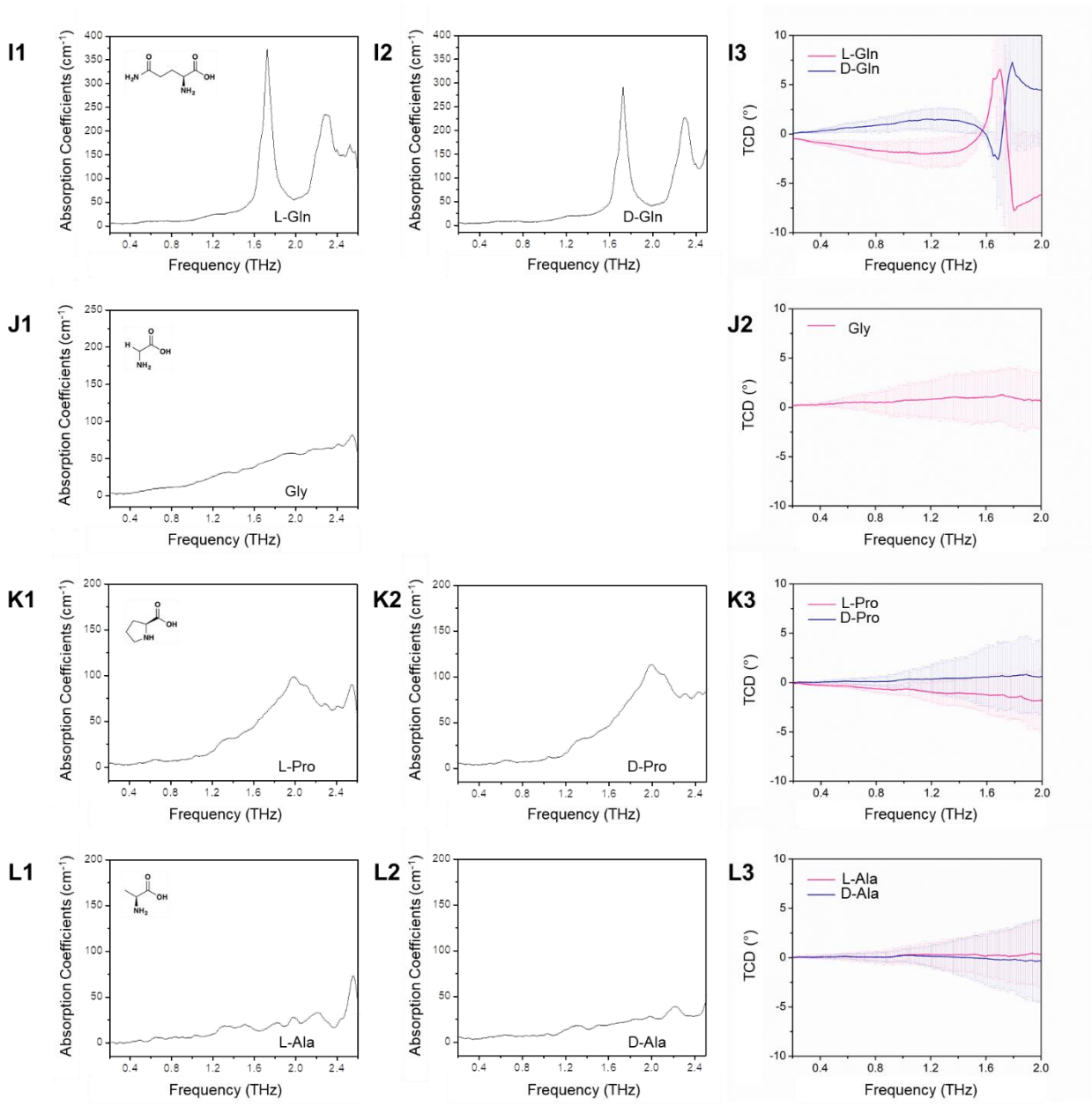
I1
Absorption Coefficients (cm⁻¹)
L-Gln
Frequency (THz)
I2
Absorption Coefficients (cm⁻¹)
D-Gln
Frequency (THz)
I3
L-Gln
D-Gln
TCD (°)
Frequency (THz)
J1
Absorption Coefficients (cm⁻¹)
Gly
Frequency (THz)
J2
Gly
TCD (°)
Frequency (THz)
K1
Absorption Coefficients (cm⁻¹)
L-Pro
Frequency (THz)
K2
Absorption Coefficients (cm⁻¹)
D-Pro
Frequency (THz)
K3
L-Pro
D-Pro
TCD (°)
Frequency (THz)
L1
Absorption Coefficients (cm⁻¹)
L-Ala
Frequency (THz)
L2
Absorption Coefficients (cm⁻¹)
D-Ala
Frequency (THz)
L3
L-Ala
D-Ala
TCD (°)
Frequency (THz)

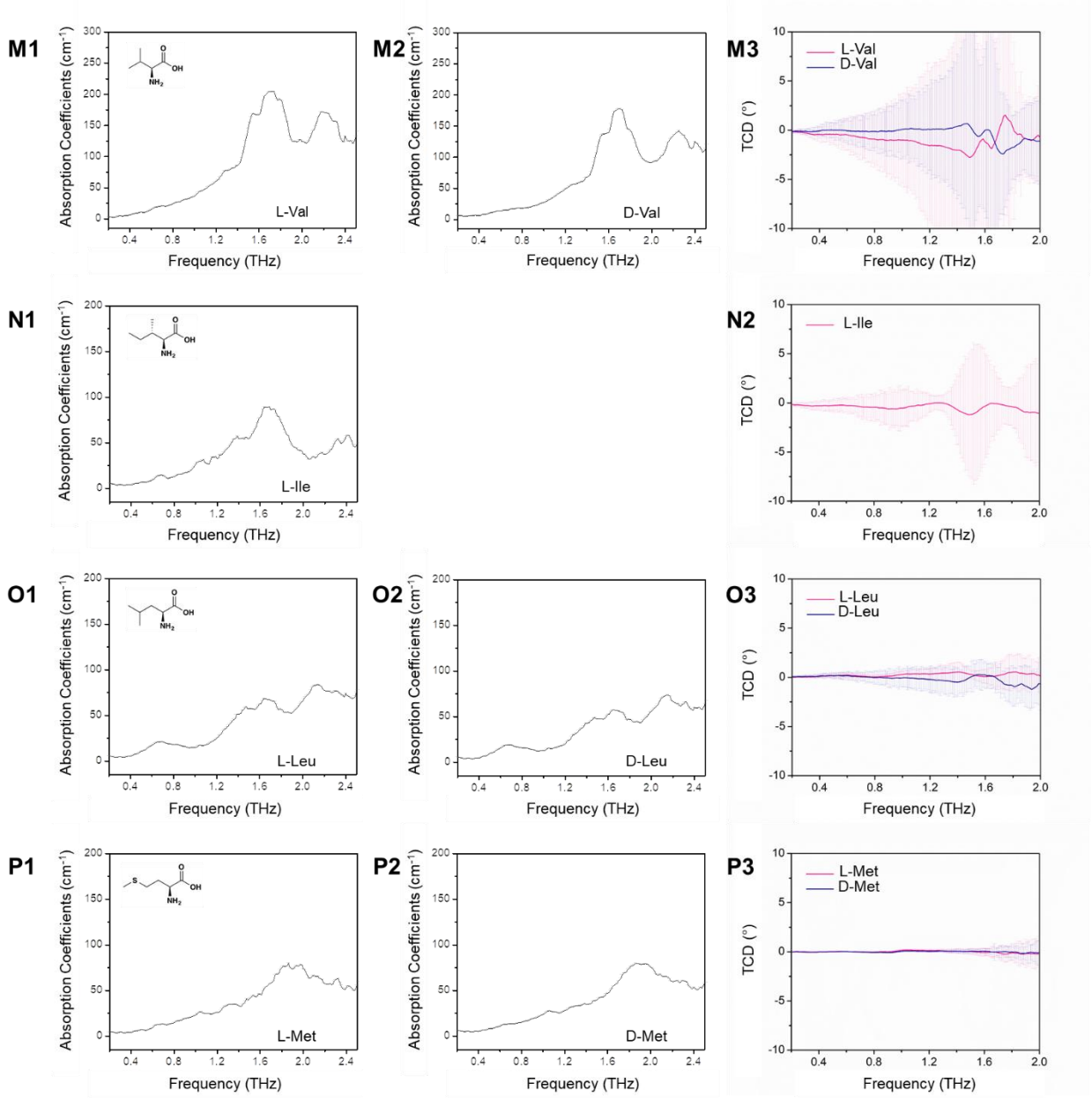
M1
Absorption Coefficients (cm-1)
L-Val
Frequency (THz)
M2
Absorption Coefficients (cm-1)
D-Val
Frequency (THz)
M3
L-Val
D-Val
TCD (°)
Frequency (THz)
N1
Absorption Coefficients (cm-1)
L-Ile
Frequency (THz)
N2
L-Ile
TCD (°)
Frequency (THz)
O1
Absorption Coefficients (cm-1)
L-Leu
Frequency (THz)
O2
Absorption Coefficients (cm-1)
D-Leu
Frequency (THz)
O3
L-Leu
D-Leu
TCD (°)
Frequency (THz)
P1
Absorption Coefficients (cm-1)
L-Met
Frequency (THz)
P2
Absorption Coefficients (cm-1)
D-Met
Frequency (THz)
P3
L-Met
D-Met
TCD (°)
Frequency (THz)

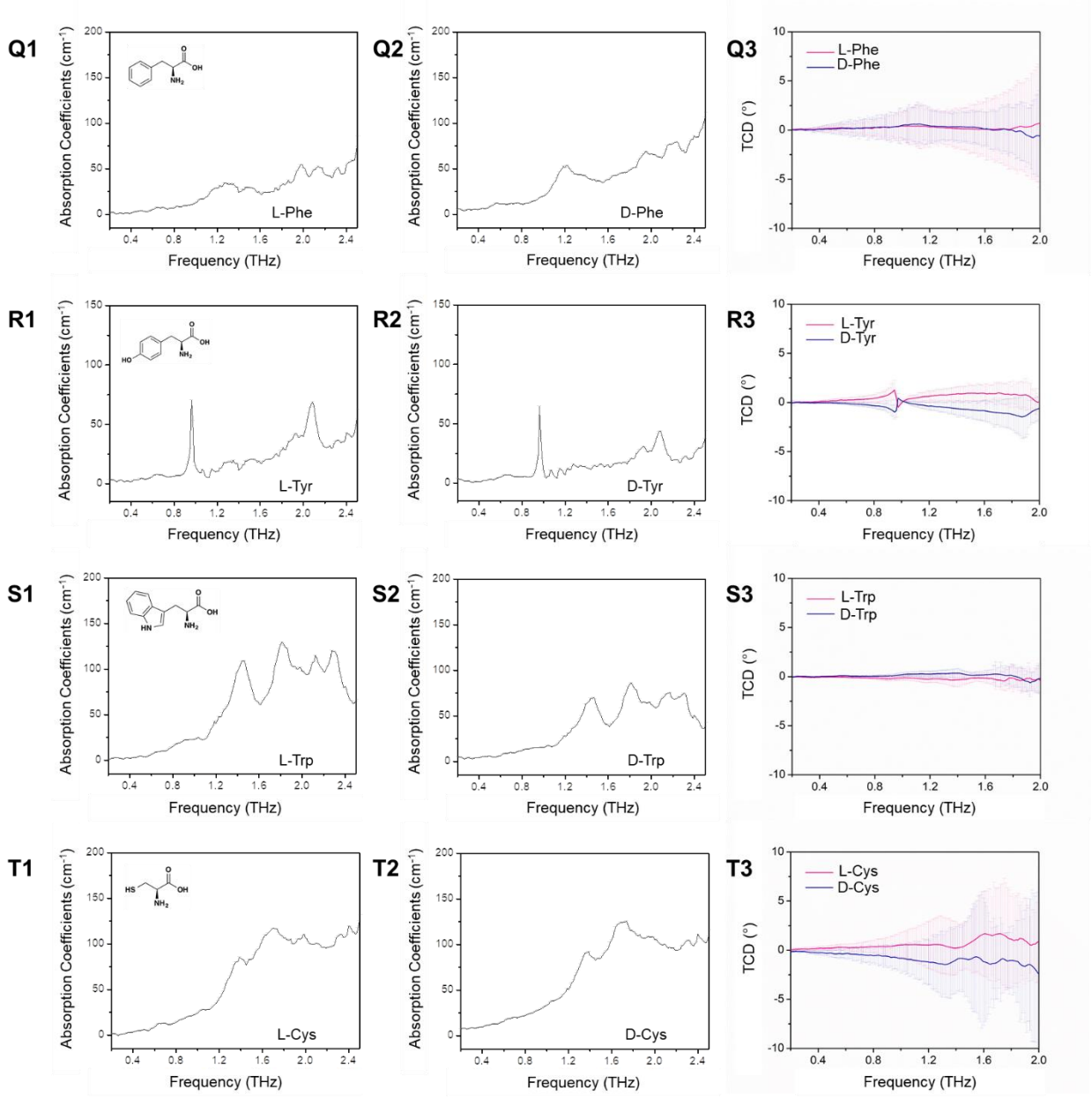

Figure 4-13 TA and TCD spectra from AAs crystals for (**A1** to **A3**) recrystallized *L*- and *D*-arginine. (**B1** to **B3**) Recrystallized *L*- and *D*-histidine. (**C1** to **C3**) *L*- and *D*-lysine. (**D1** to **D3**) Recrystallized *L*- and *D*-aspartic acid. (**E1** to **E3**) Recrystallized *L*- and *D*-glutamic acid. (**F1** to **F3**) Recrystallized *L*- and *D*-glutamic acid. (**G1** to **G3**) Recrystallized *L*- and *D*-threonine. (**H1** to **H3**) Recrystallized *L*- and *D*-asparagine. (**I1** to **I3**) Recrystallized *L*- and *D*-glutamine. (**J1** and **J2**) Recrystallized glycine. (**K1** to **K3**) Recrystallized *L*- and *D*-proline. (**L1** to **L3**) Recrystallized *L*- and *D*-alanine. (**M1** to **M3**) Recrystallized *L*- and *D*-valine. (**N1** and **N2**) Recrystallized *L*-isoleucine. (**O1** to **O3**) Recrystallized *L*- and *D*-leucine. (**P1** to **P3**) Recrystallized *L*- and *D*-methionine. (**Q1** to **Q3**) Recrystallized *L*- and *D*-phenylalanine. (**R1** to **R3**) Recrystallized *L*- and

D-tyrosine. (**S1** to **S3**) Recrystallized *L*- and *D*-tryptophan. (**T1** to **T3**) Recrystallized *L*- and *D*-cysteine. Reproduced from ref.(*2*).

Molecule name and abbreviation	Molecular weight (g/mol)	The First Peak positions (THz)
Glycine, Gly	75.07	2.55
Alanine, Ala	89.09	2.23
Serine, Ser	105.09	1.99
Proline, Pro	115.13	1.99
Valine, Val	117.15	1.53
Threonine, Thr	119.12	1.44
Cysteine, Cys	121.16	1.39
Isoleucine, Ile	131.17	1.39
Leucine, Leu	131.17	0.67
Asparagine, Asn	132.12	1.87
Aspartic Acid, Asp	133.11	1.25
Glutamine, Gln	146.14	1.72
Lysine, Lys	146.19	0.94
Glutamic Acid, Glu	147.13	1.22
Methionine, Met	149.21	1.04
Histidine, His	155.15	0.77
Phenylalanine, Phe	165.19	1.26
Arginine, Arg	174.2	0.99
Tyrosine, Tyr	181.19	0.96
Tryptophan, Trp	204.23	0.85
Ala-Ala	160.17	1.23
Ala-Gln	217.22	0.61
Carnosine, Ala-His, CAR	226.23	0.56
Cystine, Cys-Cys, CYT	240.3	0.71
Ala-Tyr	252.27	0.55

Table 4-3 Summary of the peak positions of all samples. Reproduced from ref.(*2*).

4.5 Results of TA and TCD spectra from Amino Acids

The TA for each pixel is calculated directly from E_x and E_y, fast Fourier transform of the electric fields in the *x* and *y* directions obtained by three different polarization measurements, while TCD and TORD spectra for each pixel were determined from the Stokes equations (**Figure 4-9F to G**) (*1*, *38*). The TA spectra for the *L* and *D* enantiomers of the 20 AAs obtained in this study (**Figure 4-14A,B**) as well as the TA spectra observed for their subset using pelleted samples in prior studies (*81*, *83*, *87*) consistently indicate that the molecular structure alone cannot explain their THz spectral features. For example, the one-carbon-atom difference in the side chains of aspartic acid, Asp, and glutamic acid, Glu, leads to a drastic change in the number, position, and width of all the TA peaks (**Figure 4-13 and Figure 4-14A,B**). The same conclusion can also be reached by analyzing the TA spectra using a dynamic time-warping (DTW) algorithm and 'violin' plots. Both of these methods reveal inconsistencies of TA spectra grouping according to the hydrophobic, charged or uncharged side chains in AA (**Figure 4-14C,D**), which means that local vibrational modes (i.e. *within* molecular segments) are unable to explain THz oscillatory phenomena. This conclusion is further substantiated by quantum mechanical (QM) calculations of the THz spectra of individual AA molecules, which differ strongly from the experimentally observed spectra.

Two dominant types of TA spectra can be recognized for all AAs in **Figure 4-14D to F**. *Type 1* spectra, exemplified by methionine (Met), show monotonically increasing absorptions with broad peaks, whereas *Type 2* spectra, exemplified by glutamine (Gln) or glutamic acid (Glu), display multiple sharp peaks. Note that attribution to *Type 1* or *Type 2* does not correlate with the chemical properties of the side chains (*i.e.* mass, charge and hydrophobicity), whereas a distinct

negative correlation between the molecular masses of the AAs and the lowest THz resonance peak positions for both types of TA spectra (**Figure 4-14G**) was observed. Such dependence on molecular mass indicates that the collective long-range displacements of AA molecules or their large segments are responsible for these peaks (*106*).

Going further, we found that *Type 1* and *Type 2* spectra are nearly perfectly correlated with the symmetry group of the unit cell of the AA crystals (**Table 4-2**). All five *Type 2* AAs crystallize in the orthorhombic space group $P2_12_12_1$ - the most common for biocrystals (*107*) (**Figure 4-14F**). *Type 1* AAs crystallize in monoclinic space groups $P2_1$ or C2 (**Figure 4-14E**). By comparing the XRD data with THz spectra, one can see that the crystallinity is the key requirement for the observation of the sharp TA peaks: subtle changes in XRD result in distinctly different features in the TA spectra (**Figure 4-6** and **Figure 4-7**). Concomitantly, the absence of the long-range order leads to featureless, broad spectra (**Figure 4-8**) (*22*, *108*). It therefore becomes clear that the sharp peaks at the low frequency observed for *Type 2* AAs are associated with well-resolved phonon modes. The broad peaks in crystals of *Type 1* and *Type 2* AAs are expected to be a superposition of multiple phonons and other vibrational modes.

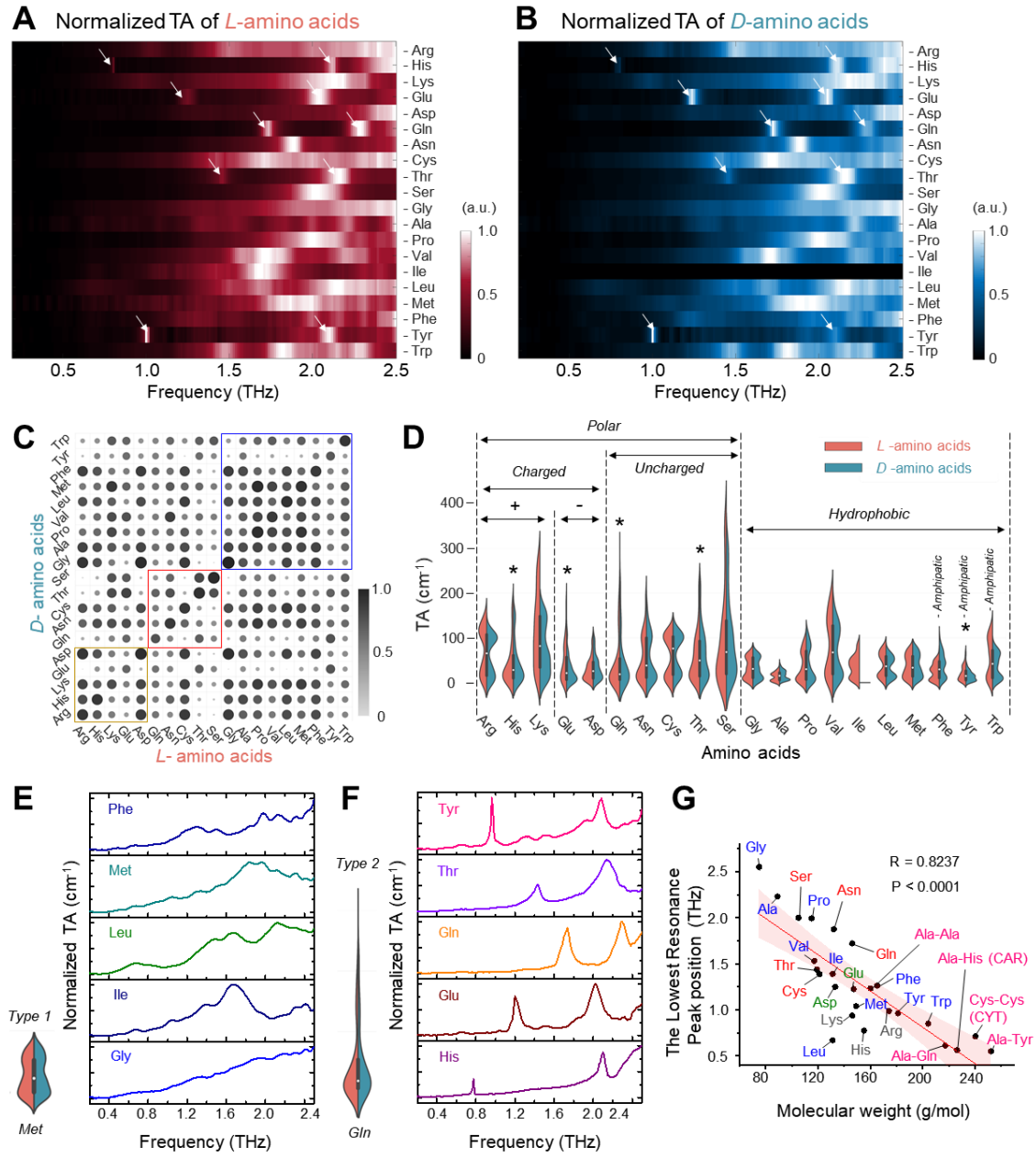

Figure 4-14 Analysis of TA spectra for *L* and *D* enantiomers of 20 AAs. (**A** and **B**) 2D plot of TA spectra with band intensity represented by the color brightness. The same samples of achiral glycine were used for the TA analysis. White arrows indicate the appearance of sharp peaks in the spectra. (**C**) 2D correlation matrix between *L*- and *D*-AAs without isoleucine. Larger sizes and darker colors indicate higher degrees of similarity between AAs. Some groups show similarity as indicated by square boxes; blue for hydrophobic, red for uncharged polar and gold for charged polar side groups. (**D**) 'Split violin' side-by-side plots for TA spectra of the two enantiomers of AAs. The left half shows those of *L*-AAs and the right shows those of *D*-AAs. (**E** and **F**) Normalized TA spectra of five representative *L*-AAs having broad peaks and sharp peaks,

respectively. The shape of the distribution is dependent on the width of the peaks: broad peak AAs – *Type 1*, sharp peak AAs – *Type 2*. (**G**) Molecular weight dependence of the lowest THz resonance peak position. The lowest peak appearing above the baseline was chosen for each AA crystal and the exact peak positions of the absorption peaks are summarized in Table S4. Color labels correspond to different groups; gray - positively charged polar, green - negatively charged polar, red - uncharged polar, blue - hydrophobic AAs and pink - dipeptides. AAs with larger molecular mass show lower resonance frequencies. Reproduced from ref.(*2*).

4.6 Statistical analysis of TA spectra

4.6.1 Correlation Matrix

To calculate the similarity between spectra and construct a correlation matrix, we adopted the dynamic time warping (DTW) approach (*109*, *110*). DTW has been widely used as a distance measure for series classification because matching is relatively elastic and robust for many cases. Since DTW determines an optimal alignment between two sequences, this allows DTW to practically match similar shape sequences together even though the sequences may be slightly shifted or distorted. Given two sequences, $X = (x_1, x_2, \dots x_N), N \in \mathbb{N}$ and $Y = (y_1, y_2, \dots y_M), M \in \mathbb{N}$, the optimal nonlinear warping function ϕ_x and ϕ_y remaps the series of X and Y, respectively. The average accumulated misalignment (distortion) between the two data series X and Y was computed by the following equation,

$$d_\phi(X,Y) = \sum_{k=1}^{T} \frac{d\left(\phi_x(k), \phi_y(k)\right) m_\phi(k)}{M_\phi} \tag{8}$$

where $m_\phi(k)$ is a per-step weighing coefficient and M_ϕ is the normalization constant (*109*).

The DTW algorithm computes the optimal warping path (alignment path) by minimizing the $d_{\phi}(X, Y)$, imposing following conditions (*110*):

1. The starting and ending points of the warping path must be aligned with the first and the last points of the sequence.
2. The data should preserve the order of points
3. The warping path has to follow the step-size limitation rule, $\boldsymbol{d_{l+1} - d_l} \in \{(\mathbf{1}, \mathbf{1}), (\mathbf{1}, \mathbf{0}), (\mathbf{0}, \mathbf{1})\}$

In this study, we used DTW instead of the conventional Euclidean distance method because the DTW method has ability to compromise slight spectral mismatches. Since terahertz spectra from AA have some variations due to the intrinsic heterogeneity of samples, elastic matching is essential for proper analysis. Specifically, we used 'dtaidistance' python package (https://pypi.org/project/dtaidistance/) and alignment results with optimal warping path between TA spectra of *L*-cys and *D*-cys generated by DTW algorithm are shown in **Figure 4-15** (*111*).

4.6.2 'Violin' Plots

'Violin' plots are a method of plotting numeric data and can be considered a combination of conventional box plot with a kernel density plot (*112*). Here, we treated TA spectra as the distribution density of magnitude of vibrations and plotted 'grouped violin plots with split' (specifically, the seaborn python package was used).
(https://seaborn.pydata.org/examples/grouped_violinplots.html)

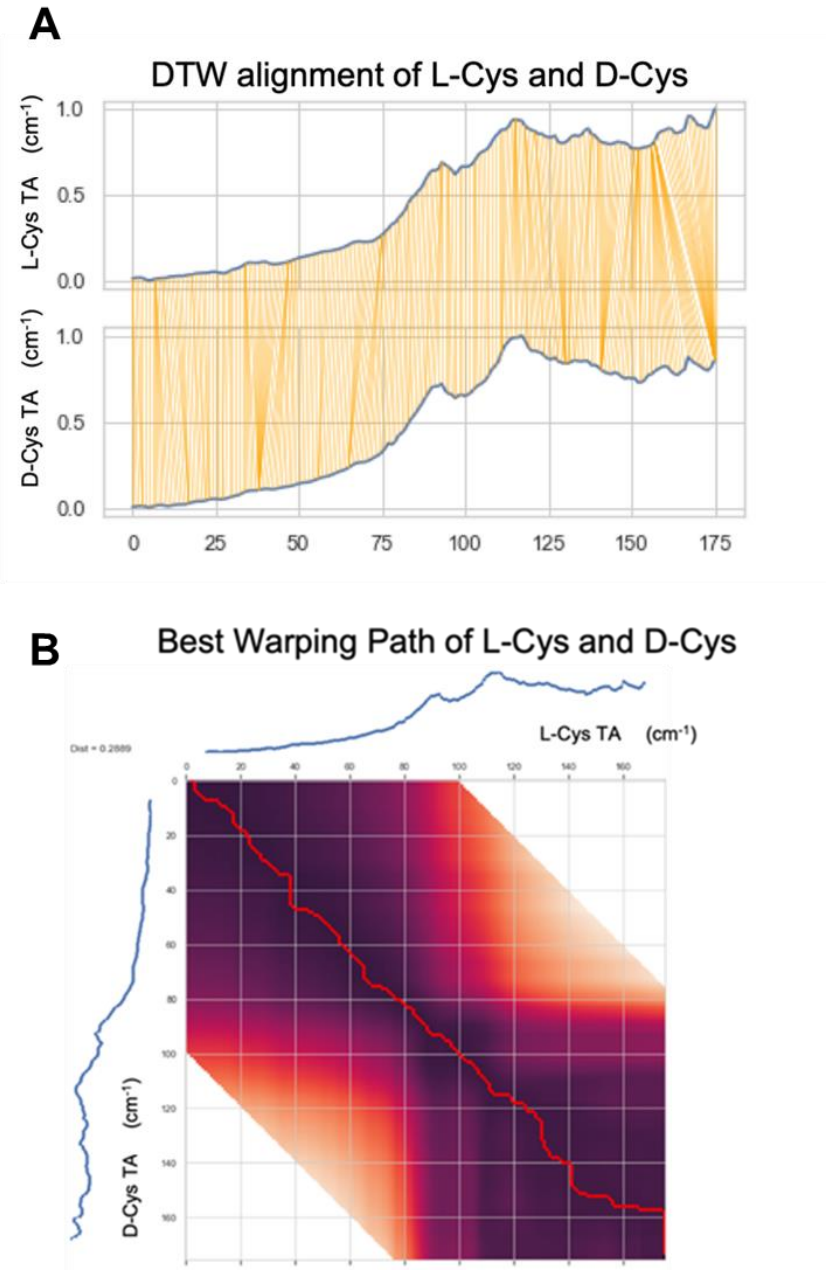

Figure 4-15 Example of warping path analysis of TA spectra of *L*-Cys and *D*-Cys. (**A**) The DTW algorithm finds the optimal path (pairing) between two spectra that yields the smallest dissimilarity between the spectra. (**B**) The optimal warping path aligning experimental spectra from (A). Reproduced from ref.(*2*).

4.7 Coupled Bi-Oscillator Model

4.7.1 Born-Kuhn (BK) model

Two coupled oscillators are separated and oriented relative to each other carrying out harmonic oscillations that could be excited by an incident electromagnetic wave as follows (*113*, *114*):

$$\partial_t^2 \vec{u}_1 + \gamma \partial_t \vec{u}_1 + w_0^2 \vec{u}_1 + \xi u_2 \hat{u}_1 = -\frac{e}{m^*}(\vec{E}_0 \cdot \hat{u}_1)\hat{u}_1 e^{i(\vec{k}\cdot\vec{r}_1 - wt)} \quad (9)$$

$$\partial_t^2 \vec{u}_2 + \gamma \partial_t \vec{u}_2 + w_0^2 \vec{u}_2 + \xi u_1 \hat{u}_2 = -\frac{e}{m^*}(\vec{E}_0 \cdot \hat{u}_2)\hat{u}_2 e^{i(\vec{k}\cdot\vec{r}_2 - wt)} \quad (10)$$

where each harmonic oscillation $\vec{u}_i$ is characterized by an amplitude $u_i(w,t)$, resonant frequency w_0, optical damping parameter γ, and coupling strength ξ, for $i,j = 1,2$. The oscillator locations can be described by $\vec{r}_i = \vec{r}_0 + \delta\vec{r}_i$, with $\delta\vec{r}_i$ being the oscillator displacement from the center of mass $\vec{r}_0$. Electron charge, effective mass and wave vector are e, m^*, $\overrightarrow{k}$, respectively. In order to investigate the value of the TORD and its associated TCD, determination of refractive indices of left-and right-handed circularly polarized light are required. Here, we solved this equation using a simplified model after making some assumptions. We assumed two identical corner-stacked, vertically displaced springs that have a 90° angle between them. Also, we assumed this media as an isotropic reciprocal spatially dispersive media (*113*, *114*). The displacement length between two springs in the z-axis is assumed to be d. The set of differential equations (9) and (10) together with Drude–Born–Fedorov constitutive equation (11) are readily solved and result in nonlocality tensor Γ(k, w) (*113*, *114*).

$$\vec{D}(w,\vec{r}) = \varepsilon_0 \varepsilon \vec{E}(w,\vec{r}) + \Gamma\Delta \times \vec{E}(w,\vec{r}) \quad (11)$$

$$\varepsilon_{iso} = 1 + \frac{2N_0e^2}{3m}\frac{w_0^2 - i\gamma w - w^2}{(w_0^2 - i\gamma w - w^2)^2 - \xi^2} \quad (12)$$

$$\Gamma_{iso} = \frac{dN_0e^2}{3m}\frac{\xi}{(w_0^2 - i\gamma w - w^2)^2 - \xi^2} \quad (13)$$

where $N_0$is number of 'Born molecules'. In turn, this tensor is associated to TCD and TORD by the relations $\mathrm{TCD} = \frac{2\mathrm{w}}{\mathrm{c}}\mathrm{Im}\{\Gamma\}$ and $\mathrm{TORD} = \frac{\mathrm{w}}{2\mathrm{c}}\mathrm{Re}\{\Gamma\}$, respectively, where c is the speed of light (*113*, *114*).

4.7.2 Parametric Fitting using non-Linear Regression Method

From the BK model, simplified TCD and TORD can be expressed as follows:

$$TCD = \frac{1}{\omega^2} Im\left(\frac{A\xi\omega}{(\omega_0^2 - i\gamma\omega - \omega^2)^2 - \xi^2}\right) \quad (14)$$

$$TORD = \frac{1}{\omega^2} Re\left(\frac{B\xi\omega}{(\omega_0^2 - i\gamma\omega - \omega^2)^2 - \xi^2}\right) \quad (15)$$

where the amplitude coefficients A and B, ω_0, γ, and ξ are the parameters needed to be fitted (*34*). The natural frequency, ω_0, was determined by the results of TA. The parametric fitting process of TCD and TORD were done separately and consequently fitting four parameters for each equation. Levenberg-Marquardt non-linear least-squares algorithm (*115*, *116*) was exploited to extract these fitting parameters. This algorithm is based on an iterative procedure to find the minima of the square error between the measured value and the calculated value:

$$\hat{\beta} \in argmin_\beta \sum_{i=1}^{n} [y_i - f(\omega_i, \beta)]^2 \quad (16)$$

where β is the fitting parameter, y_i is the measured TCD or TORD value, and f is the calculated TCD or TORD values from equations (14) and (15). Since multiple minima exist in this case, the algorithm was calculated using several different initial guesses to find the global minima. This calculation was performed using MATLAB. The results of this fitting are shown in **Figure 4-16** and in **Table 4-4**. It should be noted that the BK model perfectly matches with the experimental results of TCD and TORD.

4.8 Chiral Phonon peaks in Type2 AAs

The sharp peaks in the spectra of *Type 2* AAs were investigated in greater detail. The $P2_12_12_1$ space group, uniting this type of biocrystals, has three 2_1 screw axes producing chiral patterns inside the unit cell. Correspondingly, the nitrogen atoms of the amine groups ($-NH_2$) and N-H···O hydrogen bonds form helices in the unit cell (e.g., *L*-Glu in **Figure 4-17C**). To investigate the mirror asymmetry of the observed phononic modes, TCD and TORD spectra of AAs and their enantiomers were obtained (**Figure 4-13**, **Figure 4-17A,B**). All five *Type 2* AAs (His, Glu, Gln, Thr, Tyr) forming crystals in the $P2_12_12_1$ space group showed distinct bisignate TCD peaks at low frequency, with nearly perfect mirror symmetry for *L* and *D* enantiomers, clearly indicating the chirality of these phonons (**Figure 4-16**, **Figure 4-17, A, B, H and I)**. Other AAs may also support some modes of chiral phonons but their TCD spectra are broad, these features being likely to form from the superposition of multiple overlapping modes (**Figure 4-13**).

Born-Kuhn (BK) model of coupled bi-oscillators(*113*, *114*) may provide heuristic level of understanding of chiral phonons in various biocrystals**.** Unlike previous versions of BK used for chiral plasmons (*113*, *114*), the bi-oscillators in **Figure 4-17D,E** represent AA segments coupled

via hydrogen bonds. They are stacked on top of each other with twists between the molecules, similar to the $P2_12_12_1$ lattice in **Figure 4-17C**. A left- or right-circularly polarized beam matching the handedness of the bi-oscillators can thereby excite their collective vibrations (**Figure 4-17D,E**). The polarization-dependent light absorption is represented by the nonlocality tensor $\mathbf{\Gamma}(k, w)$, and for the model in **Figure 4-17C** it acquires the form (13). The inverse dependence of $\mathbf{\Gamma}(k, w)$ on m in Eq. 1 rationalizes the empirically observed inverse relationship between the TA peak position and molecular mass of AA (**Figure 4-14**). TCD and TORD spectra can be calculated from $\mathbf{\Gamma}(k, w)$ by applying the Drude–Born–Fedorov formalism (*113*, *114*) as

$$TCD = \frac{2w}{c} Im\{\mathbf{\Gamma}\} \qquad \text{Eq. 2}$$

$$TORD = \frac{w}{2c} Re\{\mathbf{\Gamma}\}, \qquad \text{Eq. 3}$$

where c and w are the speed of light and oscillation frequency, respectively (Supplementary Information). The calculated TCD and TORD spectra match the shape and position of the experimental ones very well (**Figure 4-16**, **Figure 4-17H,I**). As perhaps expected, increases in the coupling parameter ξ increase the amplitude of the TCD and TORD peaks, which shows that stronger intermolecular bonds in biocrystals promote the propagation of chiral phonons (**Figure 4-17G**). Concurrently, increase in the damping parameter γ reduces the intensity of the chiroptical THz peaks (**Figure 4-17F**). Since both ξ and γ strongly influence the shapes of the TCD and, in particular, TORD peak, one can confidently fit the experimental data with the BK model obtaining the values of γ and ξ (**Table 4-4**) for several *Type 2* AAs (**Figure 4-16**, **Figure 4-17H**,**I**). We found that the damping parameter (*117*, *118*) decreases with the increase of the polarizability, μ, of the AA constituting the crystals (**Figure 4-17J**), which can facilitate the selection of biocrystals predisposed to high-intensity chiral phonons.

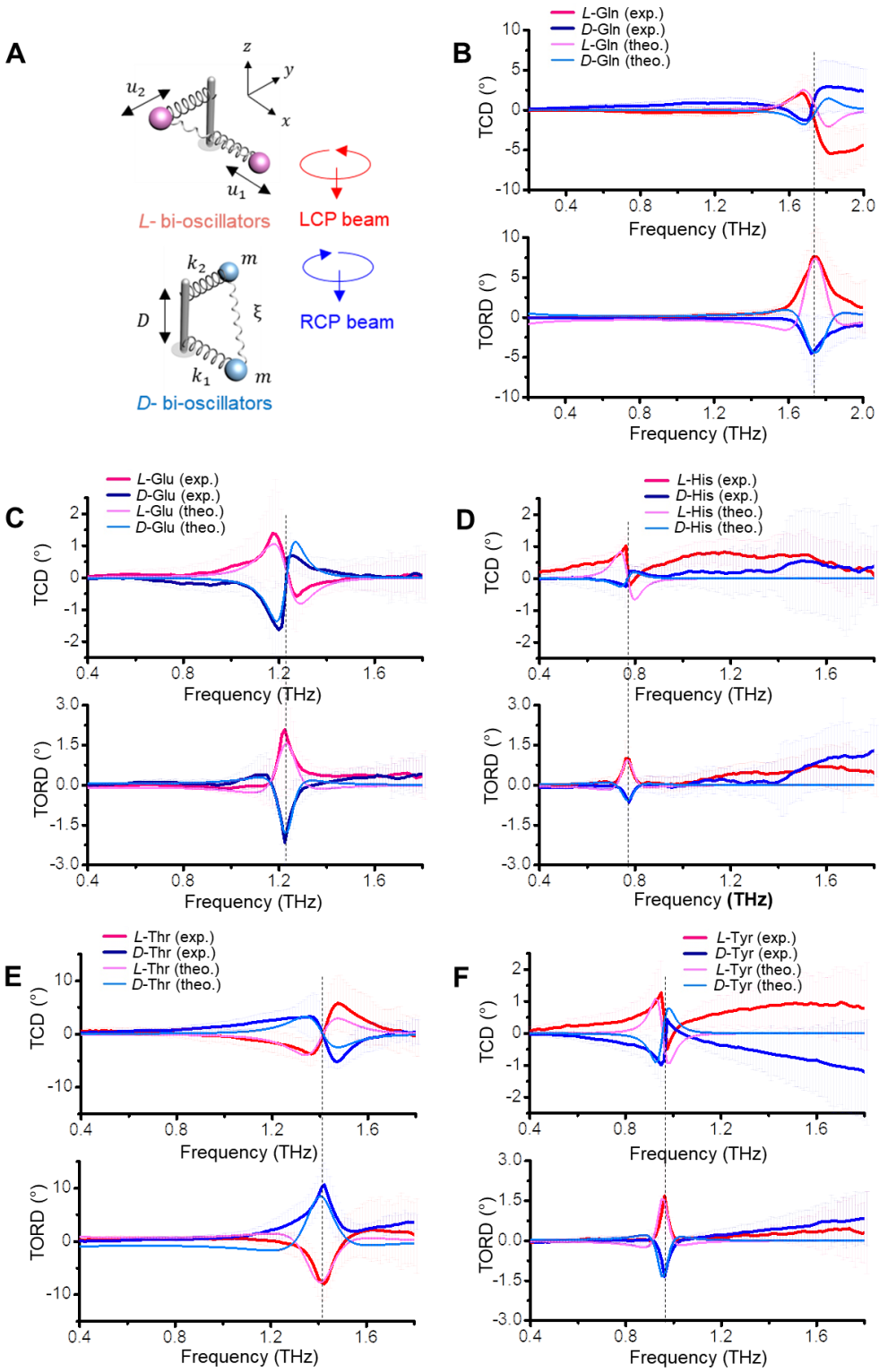

Figure 4-16 Experimental and calculated TCD and TORD spectra for *L* and *D* enantiomers of five *Type 2* AAs. (**A**) Coupled bi-oscillator BK models for *L* and *D* enantiomers. (**B**) glutamine (Gln). (**C**) Glutamic acid (Glu). (**D**) Histidine (His). (**E**) Threonine (Thr). (**F**) Tyrosine (Tyr). Reproduced from ref.(*2*).

Amino Acid	**BK Parameters** $: \frac{DN_0e^2}{3m}, w_0, \gamma, \xi$	**Values**
Glutamine (Gln)	A for L-Gln	37.806
	A for D-Gln	-35.749
	B for L-Gln	-36.017
	B for D-Gln	19.665
	w_0	1.233
	γ	0.0256
	ξ	0.0023
Glutamic Acid (Glu)	A for L-Glu	5.544
	A for D-Glu	-2.502
	B for L-Glu	-7.199
	B for D-Glu	4.009
	w_0	1.748
	γ	0.06482
	ξ	0.16046
Histidine (His)	A for L-His	4.043
	A for D-His	-0.899
	B for L-His	-2.519
	B for D-His	1.519
	w_0	0.771
	γ	0.00657
	ξ	0.08755
Threonine (Thr)	A for L-Thr	-310.105
	A for D-Thr	260.105
	B for L-Thr	455.874
	B for D-Thr	-505.874
	w_0	1.412
	γ	0.037712
	ξ	0.234758
Tyrosine (Tyr)	A for L-Tyr	6.092
	A for D-Tyr	-5.084
	B for L-Tyr	-6.251
	B for D-Tyr	5.341
	w_0	0.965
	γ	0.03771
	ξ	0.07892

Table 4-4 Fitted values of BK parameters for crystals of five *Type 2* AAs. Reproduced from ref.(*2*).

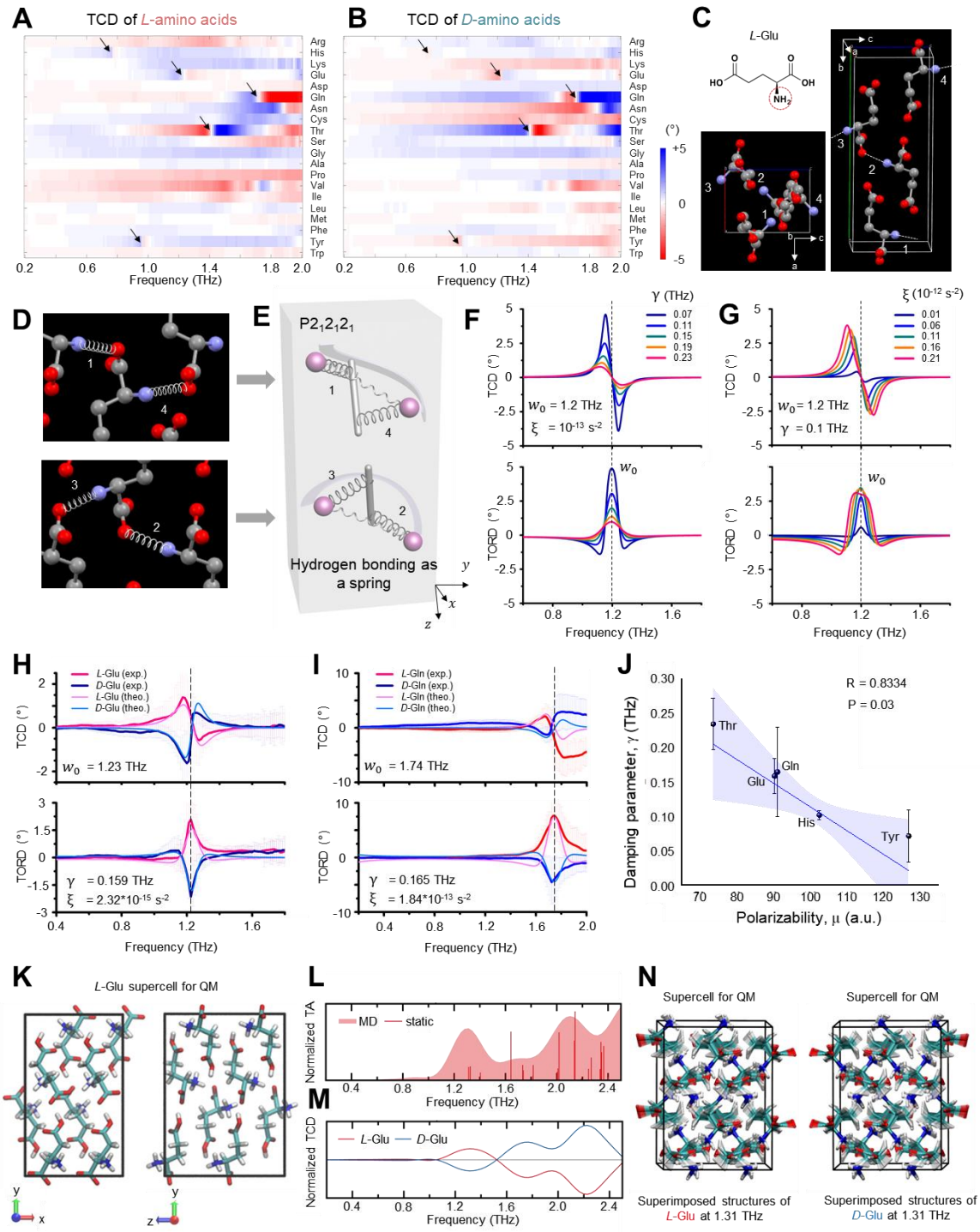

Figure 4-17 Analysis of TCD and TORD spectra for *L*- and *D*-enantiomers of 20 AAs. (**A** and **B**) 2D plot of TCD from 20 proteinogenic *L*- and *D*-AAs, respectively. *D*-isoleucine was not available. The same sample of glycine was used for analysis of both *L*- and *D*-AAs. Black arrows

indicate crossing zero points corresponding to resonance frequency, w_0 from *Eq. 1*. (**C**) Molecular configuration of *L*-Glu crystal cell as an example of a compound crystallizing in the $P2_12_12_1$ space group. Amine groups are helically arranged in the 1-2-3-4 progression. (**D**) Enlarged view of hydrogen bonds in (C), represented as springs in the BK model used for heuristic description of chiral phonons. (**E**) Schematic representation of the unit cell with bi-oscillators in $P2_12_12_1$ space symmetry. (**F** and **G**) TCD and TORD calculated from the BK model varying with damping parameter γ and coupling strength ξ. (**H** and **I)** Experimental and calculated TCD and TORD spectra of Glu and Gln, respectively. (**J**) Dependence of γ on the polarizability (μ) of AA molecules (*117*, *118*). (**K**) Supercell of *L*-Glu used for the QM computations of THz spectra. (**L**) Normalized TA spectra obtained from calculations of the *L*-Glu supercell in (K) using normal mode analysis (vertical lines) and MD simulations at the QM level (solid surfaces). (**M**) Normalized TCD spectra from the same MD simulations at the QM level used for TA in (L). (**N**) Superimposed structures of the *L*-Glu molecules along the normal mode (eigenmode) with a frequency of 1.31 THz for the system depicted in (K) (left) and its mirror image (right). Felippe M. Colombari and André F. de Moura performed the MD simulations. Reproduced from ref.(*2*).

4.9 Quantum Mechanical Simulation of Chiral Phonon mode

Further insight into the nature of lattice vibrations in crystals of AAs was obtained from atomistic computer simulations. A periodic supercell containing 2×1×2 unit cells of *L*-Glu was used for calculations of the phonon normal modes at the QM level using the GFN2-XTB Hamiltonian (*89*) (**Figure 4-17K**), as implemented in the CP2K program (*119*) (Supporting Information). The calculated TA (**Figure 4-17L**) and TCD (**Figure 4-17M**) spectra agree with the experimental results (**Figure 4-14F** and **Figure 4-17H)**. The computer simulations also enable identification of the actual chiral phonon modes responsible for the appearance of the peaks in the TCD spectra. As such, the normal mode for the 1.2-1.4 THz peak in crystals of *L*-Glu involves twisting of the carboxylate groups from both the main chain and the side chain with dihedral angles changing by tens of degrees (**Figure 4-17N** and Supplementary Information and a video file titled *Chiral Phonons*). The handedness of the rotatory motion of these groups is opposite for the two Glu enantiomers (**Figure 4-17, H and M**). The broad peaks observed for *Type 1* AAs represent

superposition of several normal modes, as exemplified for the lattice vibrations observed for *L*-Met (fig. S18). Comparison of the crystallographically-derived structures of the AAs shows the structural differences between the two types of AA crystals. In *Type 1 AAs* the side chains interact mostly by via van der Waals forces while the main chains are strongly bound by ionic interactions between charged groups. On the other hand, charged or polar groups in the side chains of *Type 2* AAs, allow for the formation of a homogeneous and strong network of supramolecular bonds throughout the crystal, which leads to the emergence of sharp TA, TCD, TORD peaks as spectroscopic signatures of chiral phonons and concurs with the high values of coupling parameter ξ established using the BK model. Besides its importance in rationalizing the TA and TCD results for various biocrystals, this structure-function relationship opens the possibility to 'tune' chiral phonon frequencies in engineered synthetic crystals.

4.9.1 Quantum Mechanical Simulation of the TA and TCD spectra

The normal modes analysis reported herein required a combination of accurate and efficient algorithms with a modern high-performance computing facility, achieving a total of 9500 hours of CPU time (meaning that a single-core CPU would have taken 13 months to have the calculations done). This timing does not include tests and validations which have not been reported here and it refers to only three out of 26 systems that were studied experimentally.

Quantum mechanical (QM) calculations were performed within the tight-binding approximation using the semiempirical GFN2-XTB Hamiltonian (*89*) as implemented in the CP2K 7.1 package (*119*). All structural optimizations were carried out using a tighter threshold for SCC convergence (10^{-8} E_h) and gradients (2×10^{-6} E_h/bohr). Vibrational analysis was then carried out

(using the same SCC convergence criteria) in order to check if the final structures correspond to true minima and also to compute the TA spectra and to assign normal modes in the region of interest. Equilibrium structures were taken as the starting structures for molecular dynamics runs (SCC convergence of 10^{-6} E_h, integration time of 0.5 fs).

4.9.2 DFT calculations for Single AAs or Dipeptide in vacuum

A single AA or dipeptide molecule was centered in a cubic cell with 1.4 nm of edge length and the Martyna-Tuckerman (MT) solver was used to treat the vacuum boundary conditions. Following the geometry optimization and vibrational analysis procedures, a short molecular dynamics equilibration run was performed in the NVT ensemble (1 ps, T = 300 K) using the Canonical Sampling through Velocity Rescale (CSVR) thermostat with a 5 fs time constant (strong coupling). Final coordinates and velocities were then taken as input for a longer molecular dynamics production run (50 ps, NVT ensemble, T = 300 K) using the Nosè-Hoover thermostat with a 100 fs time constant. Coordinates, velocities and Löwdin charges were saved for all timesteps of the production runs to compute the TA and TCD, as described below.

4.9.3 DFT calculations for Crystalline AAs or Dipeptide Supercell

The AA or dipeptide unit cell was replicated along a, b and/or c directions to draw the supercell model systems with edge lengths of at least 1 nm. Energy minimization was performed for each system by relaxing both the molecular geometries and cell vectors, but enforcing the shape corresponding to the corresponding space group. The pressure tolerance was set to 10 bar and an

external pressure of 1 bar was applied to the diagonal elements. Following the geometry optimization and vibrational analysis procedures, a short molecular dynamics equilibration run was performed at the NVT ensemble (1 ps, T = 300 K) using the Canonical Sampling through Velocity Rescale (CSVR) thermostat with a 5 fs time constant (strong coupling). Final coordinates and velocities were taken as input for a longer molecular dynamics production run (50 ps, NpT ensemble, T = 300 K using the Nosè-Hoover thermostat with τ_T = 100 fs, p = 1 bar with anisotropic coupling at fixed symmetry, τ_p = 1 ps). Coordinates, velocities and Löwdin charges were saved for all timesteps of the production runs to compute the TA and TCD, as described below.

4.9.4 Normal Mode Analysis within the Harmonic Approximation

The vibrational transitions for each system were computed by means of a normal mode analysis within the harmonic approximation. Since supercell calculations render hundreds of normal modes in the desired region (up to 2.5 THz), we took the most intense transition in this spectral region as the reference, normalized its intensity to 1.0 and discarded the transitions whose intensities were below 0.1 after this normalization.

4.9.5 TA and TCD spectra derived from MD Simulations

Both TA and TCD spectra can be obtained from atomic positions $\boldsymbol{r_i}$ and velocities $\boldsymbol{v_i}$ from the molecular dynamics trajectories and the atomic partial charges $\boldsymbol{q_i}$ computed for each geometry, by means of the Fourier transform of either the electric dipole moment $\boldsymbol{\mu}$ autocorrelation function or

the electric dipole moment $\boldsymbol{\mu}$ and the magnetic dipole moment $\boldsymbol{M}$ cross-correlation function, respectively:

$$\mu(t) = \sum_i q_i(t) r_i(t) \tag{17}$$

$$M(t) = \frac{1}{2c} \sum_i q_i(t) r_i(t) \times v_i(t) \tag{18}$$

$$TA(\omega) \propto \int_{-\infty}^{\infty} dt e^{i\omega t} \langle \mu(t) \cdot \mu(0) \rangle \tag{19}$$

$$TCD(\omega) \equiv TAC_R(\omega) - TAC_L(\omega) \propto -Im \int_{-\infty}^{\infty} dt e^{i\omega t} \langle \mu(t) \cdot M(0) \rangle \tag{20}$$

The partial atomic charges $\boldsymbol{q_i}$ were the Löwdin population computed at each timestep. Equations (17)-(20) were computed by the Travis software (*120*) using the whole production run trajectories with a depth of 8192 frames, which yielded TA and TCD spectra with a resolution of 1 cm^{-1} (0.03 THz).

4.10 Chiral Phonons in Dipeptide

The concerted movement of many atoms characteristic for chiral phonons makes them highly sensitive to the both short- and long-range organization of the molecular lattices. In the context of this study, this is essential because this sensitivity of chiral phonons makes possible their utilization in biomedical technologies. To demonstrate this capability and illustrate the generality of chiral phonons in biocrystals, TA, TCD, and TORD spectra of dipeptides, including Ala-Ala, Ala-Tyr, Ala-Gln, Gly-Gly as well as cystine (Cys-Cys linked via S-S bonds, CYT), and carnosine (Ala-His, CAR) were acquired (**Figure 4-18** and **Figure 4-19**). Among these six

dipeptides, Ala-Ala, Gln-Gln, Cys-Cys, and Ala-His display the strongest signatures of chiral phonons. Note that *L*-CYT is the key component of kidney and bladder stones (*121*), hair, nails, and skin, while *L*-CAR is known to scavenge reactive oxygen species (*122*) and formulations of its microcrystals are used as nutritional supplements, which prompted us to investigate them in greater details.

L-CYT crystallizes as hexagonal plates ($P6_122$ chiral space group, $a = b = 0.54$ nm, $c = 5.60$ nm) and the six CYT molecules in the unit cell are helically organized about the 6_1 screw axis (**Figure 4-18**) (*121*). Similar to *Type 2* AAs, TA spectra of *L*- and *D*-CYT show sharp peaks in the spectral window between 0.2 and 2.5 THz (**Figure 4-18B**). The lowest resonance peak positions at 0.71 THz and 0.56 THz shown in **Figure 4-14G** agree well with the molecular weight of CYT (240.3 g/mol) and CAR (226.23 g/mol), respectively. TCD spectra of CYT enantiomers display mirror-symmetrical peaks (**Figure 4-18B**) with the most intense TCD peak at 1.57 THz matching very well with the TCD predictions from simulations of the CYT supercell (**Figure 4-22**) The attribution of both bands to chiral phonons was also confirmed by the spectroscopic data for *DL*-CYT and deuterated *L*-CYT (**Figure 4-23**). Similarly, the TA and TCD spectra of *L*-CAR show collective vibrational modes having distinct TCD peaks (**Figure 4-18B**). Alanine-based dipeptides (Ala-Ala, Ala-Tyr, and Ala-Gln) other than *L*-CAR were also measured and the results are depicted in **Figure 4-14G** and **Figure 4-19**.

The sharpness of the TCD peaks, the selective identification of left and right modes of chiral phonons corresponding to the enantiomers of the biomolecules, and the sensitivity of their spectral attributes to small perturbations, suggest the utility of the spectroscopic toolbox for chiral phonons in biocrystals in a variety of potential biomedical and pharmaceutical applications. The non-destructive and non-ionizing nature of THz spectroscopy presents an additional benefit in this

context (*76, 77, 91, 123*), which is essential both for the patients and doctors. To evaluate the feasibility of such applications, we analyzed four naturally occurring cystine stones removed from two canine patients as part of standard veterinary medical care (**Figure 4-18C**). These stones showed strong TA peaks at exactly 0.71 THz, where the CYT slurry showed its strongest resonance (**Figure 4-18, B and D**). Hyperspectral THz mapping shows not only the size and position of the stones but also provides a phononic fingerprint of the chemical composition that cannot be obtained using X-ray diffraction (**Figure 4-18, E and F**). A negative-to-positive transition in the TCD was found in the central part of the stones and birefringence effects in the edges and non-flat areas indicate variations in the growth conditions and crystallization patterns of the stones within the patients. This method could potentially be adapted to diagnosis and analysis of calculi in the urinary bladder or kidneys.

The variability of chiral phonon signatures from *L*-CAR was also tested in commercial health supplements from five different manufacturers (**Figure 4-18G**). TA and TCD spectra (**Figure 4-18, H and I**) show large differences between the *L*-CAR formulations (**Figure 4-18B**). Ideally, the intensities of TA and TCD peaks should have the same ratio in all of the products and minimal sample-to-sample variations. However, this was not the case, as can be visualized by the TA and TCD distribution maps. These maps show distinct peak correlations specific to each manufacturer (**Figure 4-18, J and L**), which can be associated with structural differences in the *L*-CAR biocrystals and impurities. Since intermolecular interactions in biocrystals are also sensitive to aging caused by different environmental factors (*124*), the changes in TA and TCD spectra of *L*-CAR samples after heating at 65 °C for 48 hours were also evaluated. The data in **Figure 4-18, K and M** indicate that: (1) the phonon of the *L*-CAR biocrystals is temperature-sensitive, even when the environment is far below its melting temperature (T_{melt} = 253 °C) and (2)

changes occurring in TA and TCD spectra with temperature are specific to each manufacturer presumably due to various chiral and achiral additives. The observed tightening of the TCD spectra around the central point after thermal aging indicate that both recrystallization processes and chemical reactions have taken place even though appearance of the supplement does not change.

4.11 Conclusions

In conclusion, the identification of chiral phonons in the THz range in biocrystals, and the elaboration of a spectroscopic toolbox for them, opens the door to a large family of materials wherein the complex collective vibrations of crystal lattices with rotatory components can be investigated. Due to the strong sensitivity of chiral phonons to the chemical interactions in the crystal lattice, this methodological toolbox can be used for quality control in biomedical industry (*76*, *77*), biomedical imaging (*74*, *123*), and chiral photonics (*125*). The library of THz fingerprints from basic AAs to complex proteins and other biomolecular complexes would open a new horizon for THz bioinformatics and deepen our understanding of many collective-vibration-mediated (bio)chemical processes.

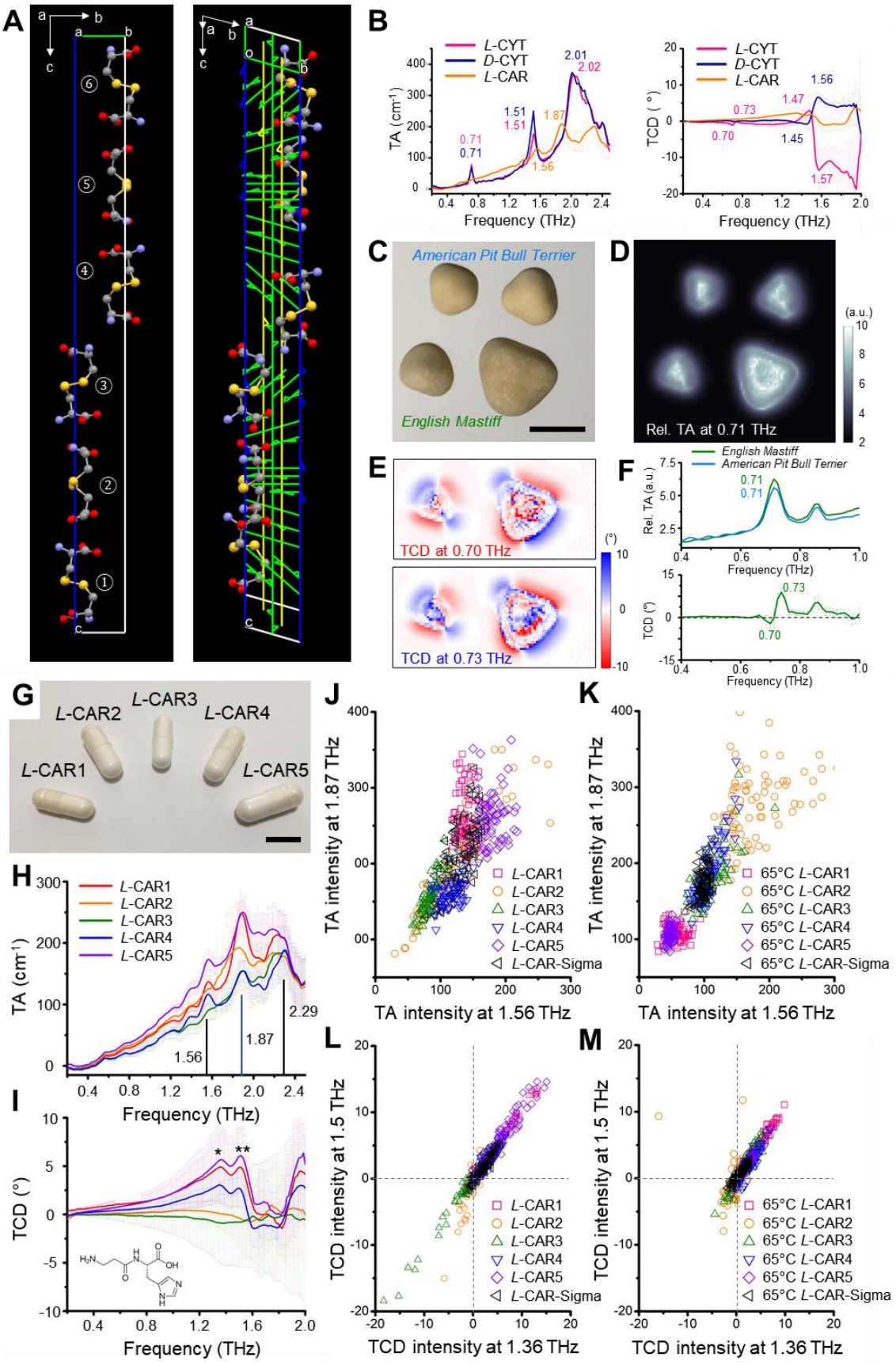
A
B
L-CYT
D-CYT
L-CAR
TA (cm-1)
Frequency (THz)
TCD (°)
C
American Pit Bull Terrier
English Mastiff
D
Rel. TA at 0.71 THz
(a.u.)
E
TCD at 0.70 THz
TCD at 0.73 THz
F
English Mastiff
American Pit Bull Terrier
Rel. TA (a.u.)
G
L-CAR1
L-CAR2
L-CAR3
L-CAR4
L-CAR5
H
I
J
TA intensity at 1.87 THz
TA intensity at 1.56 THz
L-CAR-Sigma
K
65°C L-CAR1
65°C L-CAR2
65°C L-CAR3
65°C L-CAR4
65°C L-CAR5
65°C L-CAR-Sigma
L
M
TCD intensity at 1.5 THz
TCD intensity at 1.36 THz

Figure 4-18 Chiral phonons in CYS and CAR. (**A**) Helical axis of *L*-CYT molecules in a unit cell. Six *L*-CYT molecules winding a 6_1 screw axis that coincides with the *c*-axis as indicated by green helical 'scaffold'. (**B**) Averaged TA and TCD spectra from *L*-CYT, *D*-CYT and *L*-CAR. (**C**) Photograph of four cystine stones from two canine patients. The upper two stones are from a seven-year-old male *American pit bull terrier* and the lower two stones are from a six-year-old male *English mastiff*, respectively. Scale bar is 5 mm. (**D**) Relative TA map of four cystine stones at 0.71 THz. (**E**) TCD map of cystine stones from *English mastiff* at 0.7 THz and 0.73 THz, respectively. A negative-to-positive transition in the TCD was found in the central part of the stones, while there are birefringence effects in the edges and non-flat areas, indicating variations in the growth conditions and crystallization patterns of the stones. (**F**) Averaged TA and TCD spectra from cystine stones matched well with that of *L*-CYT crystals prepared *in vitro*. (**G**) Photograph of five different pills from various manufacturers used for measurements. Scale bar is 1 cm. (**H** and **I**) Average TA and TCD spectra from as-received *L*-CAR from five different manufacturers. (**J** and **L**) 2D peak intensity distribution map of TA and TCD from as-received *L*-CAR samples. (**K** and **M**) 2D peak intensity distribution map of TA and TCD from *L*-CAR slurries after incubation at 65 °C for 48 h. Reproduced from ref.(*2*).

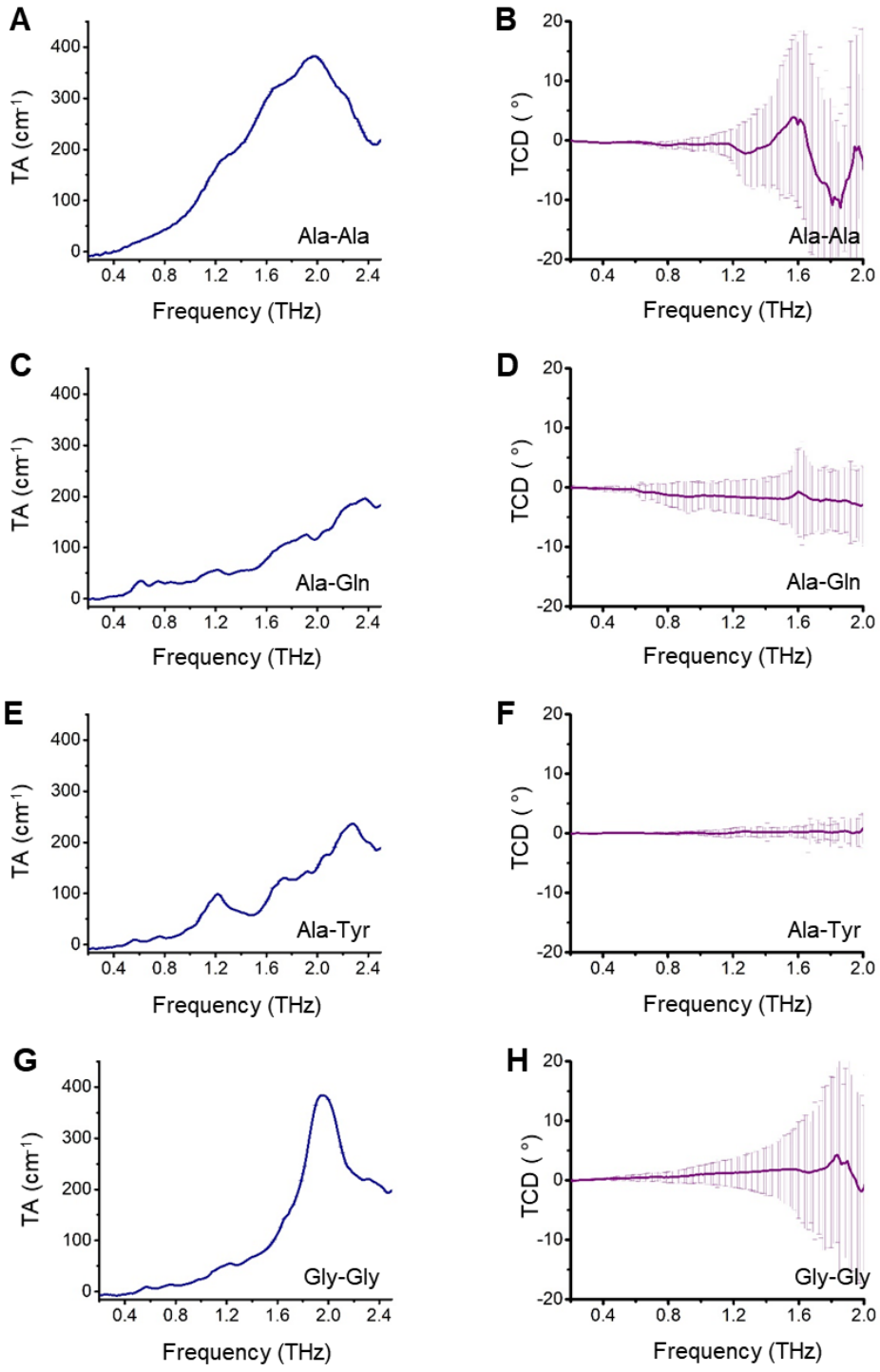

Figure 4-19 Averaged TA and TCD spectra from biocrystals of dipeptides. (**A** and **B**) Ala-Ala. (**C** and **D**) Ala-Gln. (**E** and **F**) Ala-Tyr. (**G** and **H**) Gly-Gly. Ala-Ala and Gly-Gly show large standard deviations in TCD spectra. Reproduced from ref.(*2*).

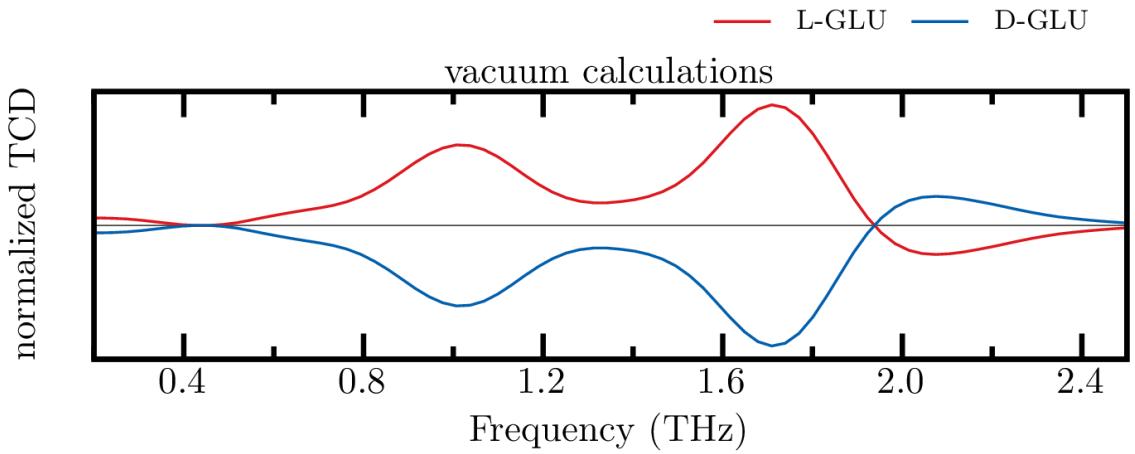

Figure 4-20 TCD spectra of *L*-Glu and *D*-Glu obtained from MD simulations of a single molecule in vacuum. Felippe M. Colombari and André F. de Moura performed the MD simulations. Reproduced from ref.(*2*).

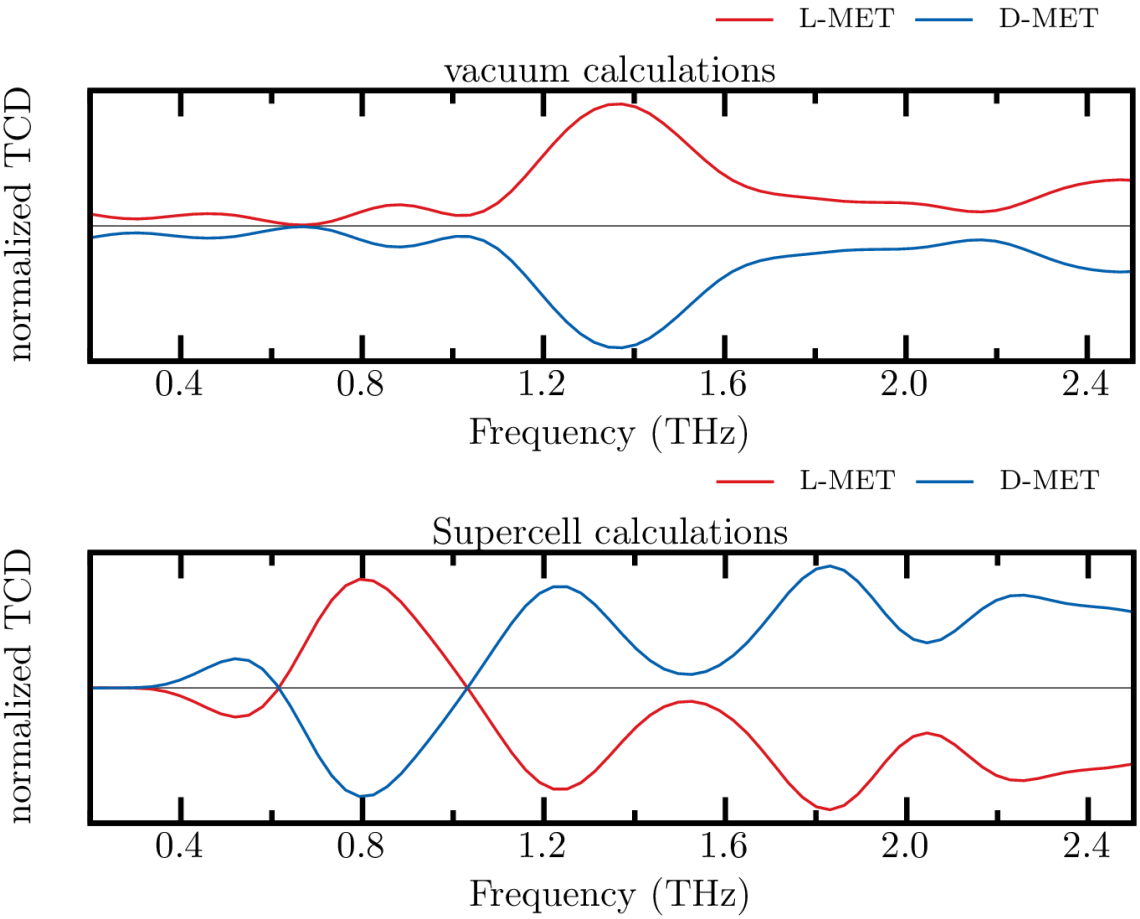

Figure 4-21 TCD spectra of *L*-Met and *D*-Met obtained from MD simulations of a single molecule in vacuum (top) or a periodic supercell (bottom). Felippe M. Colombari and André F. de Moura performed the MD simulations. Reproduced from ref.(*2*).

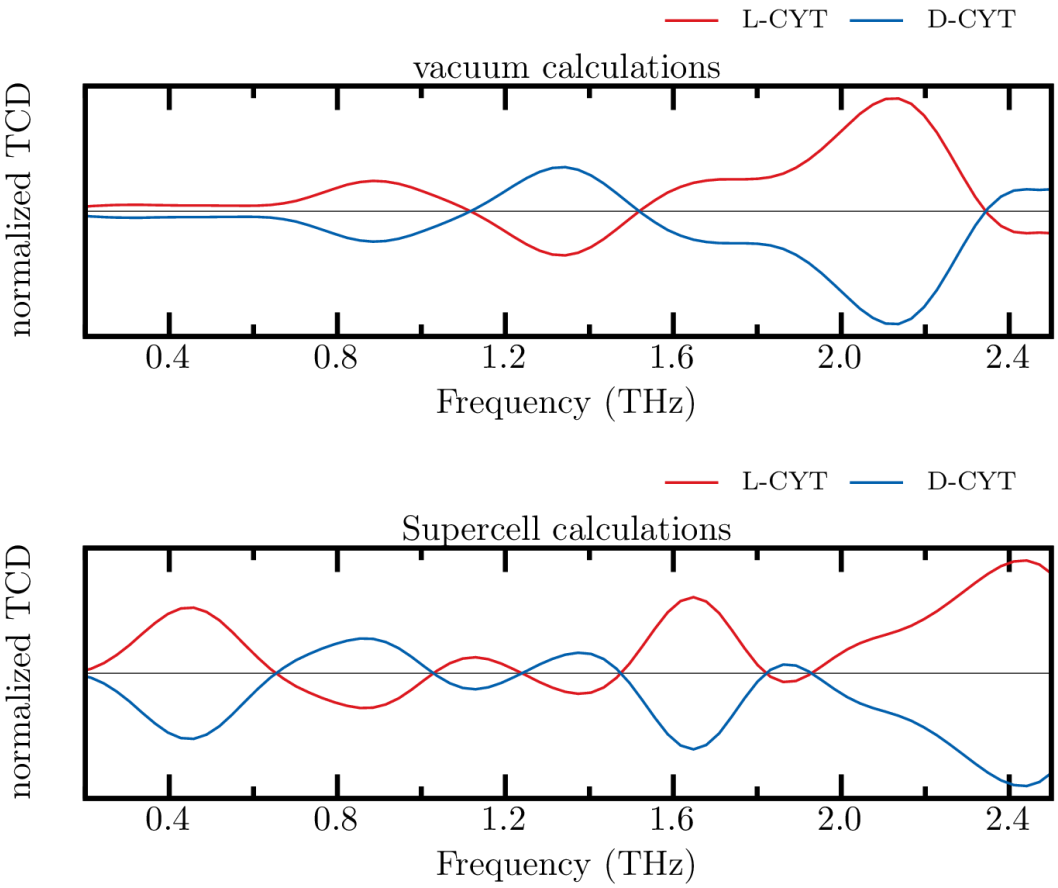

Figure 4-22 TCD spectra of *L*-CYT and *D*-CYT obtained from MD simulations of a single molecule in vacuum (top) or a periodic supercell (bottom). Felippe M. Colombari and André F. de Moura performed the MD simulations. Reproduced from ref.(*2*).

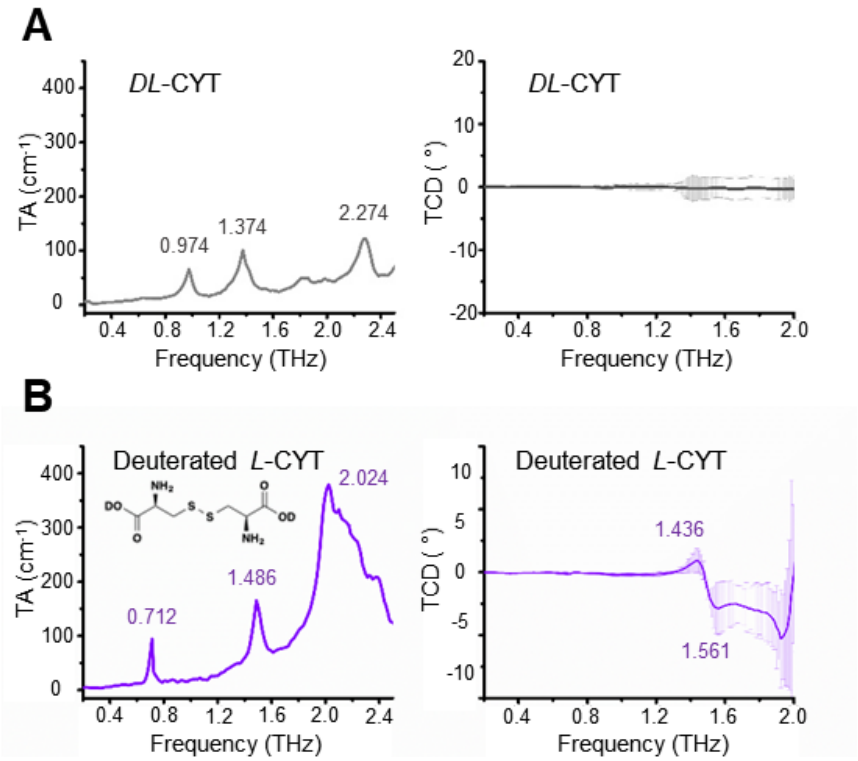

Figure 4-23 Averaged TA and TCD spectra for CYT crystals. (**A**) *DL*- CYT. (**B**) Deuterated *L*-CYT. Reproduced from ref.(*2*).

Chapter 5. Conclusion and Future Work

In this thesis, several new achievements have been described; kirigami polarization modulator for THz circular dichroism spectroscopy and observation of chiral phonon in biocrystals. In this Chapter 5, findings are summarized and the future work are discussed for each project.

5.1 Conclusions

Scientific and technological advances related to the medical diagnosis of disease and injuries, as well as monitoring of treatment have been enabled by the development of resonance-based spectroscopies. Notable examples are magnetic resonance imaging (MRI) and X-ray computed tomography (CT) scans, which allow the identification and quantification of inner tissues, organs and the nervous system. However, MRI and CT scans utilize the modulation of magnetic field with radio frequency waves and X-rays, respectively, which causes several constraints in practice such as the physical circumstance of the patients, expensive cost, bulkiness, and limited range of resonant energies of the tissues that can be probed.

In this regard, we always need fundamentally new resonance-based spectroscopic method that could overcome these issues and significantly advance the field of bioimaging. I propose to exploit excitations in the THz range frequency because they not only provide unique information about biomolecules, pharmaceuticals, and soft tissues but also because THz devices hold the potential to be scaled down to portable, hand-held sizes that can be implemented in cell phones.

Also, the weak energy of THz photons (~0.001eV) enables the probing of 'soft' oscillatory motions and phononic features in biomolecules without damage, since they are not energetic enough to remove electrons from an atom. The rapid development of ultrafast lasers (The Nobel Prize in Physics, 2018) contributed to the establishment of modern THz time-domain spectroscopy, which has started to be widely utilized in many applications. However, the beam intensity is still not strong enough to penetrate the human body. While conducting research on ultrafast lasers and THz optics during my PhD in materials engineering, I have realized that the discovery of opto-mechanical materials that can be used as powerful sources or other optical components in the THz frequency range can lead to novel non-invasive imaging techniques and initiate the new field of THz vibrational bioinformatics.

5.2 Future Work

The largest roadblock in making biomedical THz spectroscopy an everyday reality is the lack of efficient and compact terahertz emitters/detectors with broadband, gapless spectra that can be tailored for various pump photon energies. Various THz devices based on semiconductors, superconductors, graphene, optical crystals, and plasma irradiated by femtosecond laser pulses have been reported. Among them, semiconductor crystals such as ZnTe, GaP, GaAs, GaSe that employ non-linear optical rectification for THz wave emission are the most widely studied material systems. However, the THz signal from these sources is still too weak (below 0.1 mW at 1THz) for bioimaging applications, and there is the additional issue of the so-called Reststrahlen gap in the THz spectrum of these crystals that come from their strongly absorbing longitudinal optical phonon bands.

As suggested in Chapter 3, the recently developed ‘kirigami’ materials could overcome these issues by exploiting topological plasmonic metamaterials as a platform for THz emitters/detectors. Kirigami, the art of paper cutting, presents a powerful tool to create complex and tunable three-dimensional (3D) geometries from simple 2D cut patterns, which can be scaled across many orders of magnitude to yield macro- to nanoscale structures. The ability to design out-of-plane deformations and arbitrary 3D shapes at will, along with the robustness of the patterns under cyclic reconfiguration and the manufacturing simplicity promise untapped possibilities for the efficient modulation of THz optical beams in kirigami structures. In this regard, investigating kirigami metamaterials that exhibit artificial optical magnetism and sustain oscillating plasmonic currents can lead to new, reconfigurable, nonlinear optical materials with significantly low THz phonon absorption. Another astonishing property of kirigami metamaterials is their reconfigurability by mechanical force. Essentially, this implies that it is possible to tailor the electromagnetic resonances of the metamaterial emitters by strain to match any desired pump photon energy. Fine tunability of the angle between the beam and the kirigami surface by strain is another advantage. Furthermore, there is potential to dynamically modulate the properties of kirigami structures using piezoelectric actuators. I strongly believe that kirigami metamaterials irradiated by femtosecond laser pulses will result in huge optical resonance enhancement, thereby enabling previously inaccessible applications such as THz medical imaging of the human body; a timely example that demonstrates the power of this technique would be the real-time identification of phononic signatures from SARS-CoV-2 instead of using polymerase chain reaction tests that typically take a few days.

Chiral phonon modes in biocrystals will also be studied more thoroughly. This will exploit the connection between molecular symmetries and photon-phonon interaction. Actually, the relationship between the space group of biocrystals, the symmetry of the biomolecules that comprise them, and the handedness of phonon modes inside them is an important question that has emerged in the field of bioinformatics. The capability to differentiate between chiral phonon modes in biocrystals would provide a unique tool to assess biomolecular arrangements in a wide range of structures, and would have a direct impact on drug synthesis, biochemical quality control, protein folding, and disease diagnostics. Chiral phonon resolved THz spectroscopy would be a tool for in situ analysis of biochemical reactions in complex mixtures, which could also be used for identifying biomolecules on Mars.

Bibliography

1. W. J. Choi *et al.*, Terahertz circular dichroism spectroscopy of biomaterials enabled by kirigami polarization modulators. *Nat. Mater.* **18**, 820–826 (2019).
2. W. J. Choi *et al.*, Chiral Phonons in Biocrystals. *Res. Sq. Prepr. arXiv* (2021), doi:10.21203/rs.3.rs-248321/v1.
3. T. Hunt, Could consciousness come down to the way things vibrate? *EarthSky* (2018).
4. D. E. Smith, History of Mathematics (1958).
5. S. S. Rao, *Mechanical Vibrations (5th Edition)* (2010).
6. Gaffurius, (available at https://en.wikipedia.org/wiki/Pythagorean_hammers).
7. Lyres of Ur, (available at https://en.wikipedia.org/wiki/Lyres_of_Ur).
8. Resonance, (available at https://en.wikipedia.org/wiki/Resonance).
9. Natural Frequency, (available at https://en.wikipedia.org/wiki/Natural_frequency).
10. R. B. Barnes, L. G. Bonner, The Early History and the Methods of Infrared Spectroscopy. *Am. J. Phys.* **4**, 181–189 (1936).
11. M. Koç, E. Karabudak, History of spectroscopy and modern micromachined disposable Si ATR-IR spectroscopy. *Appl. Spectrosc. Rev.* **53**, 420–438 (2018).
12. J. L. Koenig, Application of Fourier Transform Infrared Spectroscopy to Chemcial Systems. *Ocean Coast. Manag.* **80**, 132 (2013).
13. Y. Peng *et al.*, Terahertz identification and quantification of neurotransmitter and neurotrophy mixture. *Biomed. Opt. Express*. **7**, 4472 (2016).

14. P. U. Jepsen, D. G. Cooke, M. Koch, Terahertz spectroscopy and imaging - Modern techniques and applications. *Laser Photonics Rev.* **5**, 124–166 (2011).

15. M. R. Patil, S. B. Ganorkar, A. S. Patil, A. A. Shirkhedkar, Terahertz Spectroscopy: Encoding the Discovery, Instrumentation, and Applications toward Pharmaceutical Prospectives. *Crit. Rev. Anal. Chem.* **0**, 1–13 (2020).

16. M. van Exter, C. Fattinger, D. Grischkowsky, Terahertz time-domain spectroscopy of water vapor. *Opt. Lett.* **14**, 1128 (1989).

17. J. He, T. Dong, B. Chi, Y. Zhang, Metasurfaces for Terahertz Wavefront Modulation: a Review. *J. Infrared, Millimeter, Terahertz Waves*. **41**, 607–631 (2020).

18. J. He *et al.*, Generation and evolution of the terahertz vortex beam. *Opt. Express*. **21**, 20230 (2013).

19. J. He, X. Wang, Y. Zhang, Abruptly autofocusing THz waves with meta-hologram. *Int. Conf. Infrared, Millimeter, Terahertz Waves, IRMMW-THz*. **2016-Novem**, 2787–2790 (2016).

20. J. Y. Guo *et al.*, Generation of Radial Polarized Lorentz Beam with Single Layer Metasurface. *Adv. Opt. Mater.* **6**, 1–6 (2018).

21. N. K. Grady *et al.*, Terahertz metamaterials for linear polarization conversion and anomalous refraction. *Science (80-.).* **340**, 1304–1307 (2013).

22. M. Walther, B. M. Fischer, P. U. Jepsen, Noncovalent intermolecular forces in polycrystalline and amorphous saccharides in the far infrared. *Chem. Phys.* **288**, 261–268 (2003).

23. D. K. Lee *et al.*, Highly sensitive and selective sugar detection by terahertz nano-antennas. *Sci. Rep.* **5**, 1–7 (2015).

24. H. B. Liu, Y. Chen, X. C. Zhang, Characterization of anhydrous and hydrated pharmaceutical materials with THz time-domain spectroscopy. *J. Pharm. Sci.* **96**, 927–934 (2007).

25. S. S. Dhillon *et al.*, The 2017 terahertz science and technology roadmap. *J. Phys. D. Appl. Phys.* **50** (2017), doi:10.1088/1361-6463/50/4/043001.

26. T. J. Yen *et al.*, Terahertz Magnetic Response from Artificial Materials. *Science (80-.).* **303**, 1494–1496 (2004).

27. S. Hunsche, M. Koch, I. Brener, M. C. Nuss, THz near-field imaging. *Opt. Commun.* **150**, 22–26 (1998).

28. W. L. Chan, J. Deibel, D. M. Mittleman, Imaging with terahertz radiation. *Reports Prog. Phys.* **70**, 1325–1379 (2007).

29. G. Acbas, K. A. Niessen, E. H. Snell, A. G. Markelz, Optical measurements of long-range protein vibrations. *Nat. Commun.* **5**, 1–7 (2014).

30. D. F. Plusquellic, K. Siegrist, E. J. Heilweil, O. Esenturk, Applications of terahertz spectroscopy in biosystems. *ChemPhysChem*. **8**, 2412–2431 (2007).

31. G. J. Wilmink, J. E. Grundt, Invited review article: Current state of research on biological effects of terahertz radiation. *J. Infrared, Millimeter, Terahertz Waves*. **32**, 1074–1122 (2011).

32. J. H. Choi, M. Cho, Terahertz Chiroptical Spectroscopy of an α-Helical Polypeptide: A Molecular Dynamics Simulation Study. *J. Phys. Chem. B.* **118**, 12837–12843 (2014).

33. M. D. King, W. D. Buchanan, T. M. Korter, Understanding the Terahertz Spectra of Crystalline Pharmaceuticals : Terahertz Spectroscopy and Solid-State Density Functional Theory Study of (S) - (+) -Ibuprofen and (RS) -Ibuprofen. *New York.* **100**, 1–14

(2011).

34. L. Cong, P. Pitchappa, N. Wang, R. Singh, Electrically Programmable Terahertz Diatomic Metamolecules for Chiral Optical Control. *Research*. **2019**, 1–11 (2019).

35. S. Zhang *et al.*, Photoinduced handedness switching in terahertz chiral metamolecules. *Nat. Commun.* **3**, 942–947 (2012).

36. S. S. Oh, O. Hess, Chiral metamaterials: enhancement and control of optical activity and circular dichroism. *Nano Converg.* **2**, 24 (2015).

37. J. Qui *et al.*, Introducing quasi-optical terahertz circular dichroism spectroscopy. *2017 11th Int. Conf. Antenna Theory Tech. ICATT 2017*, 26–29 (2017).

38. T. Kan *et al.*, Enantiomeric switching of chiral metamaterial for terahertz polarization modulation employing vertically deformable MEMS spirals. *Nat. Commun.* **6**, 1–7 (2015).

39. Circular dichroism, (available at https://en.wikipedia.org/wiki/Circular_dichroism).

40. Waveplate, (available at https://en.wikipedia.org/wiki/Waveplate).

41. Photoelastic Modulators, (available at https://www.hindsinstruments.com/products/photoelastic-modulators/).

42. Waveplates and Retarders, (available at https://www.edmundoptics.com/c/waveplates-retarders/664/).

43. L. Xu *et al.*, Kirigami Nanocomposites as Wide-Angle Diffraction Gratings. *ACS Nano*. **10**, 6156–6162 (2016).

44. M. K. Blees *et al.*, Graphene kirigami. *Nature*. **524**, 204–207 (2015).

45. A. Rafsanjani, K. Bertoldi, Buckling-induced kirigami. *Phys. Rev. Lett.*, 1–15 (2017).

46. Z. Liu *et al.*, Nano-kirigami with giant optical chirality: supplementary material. *Sci. Adv.*, 1–9 (2018).

47. S. J. P. Callens, A. A. Zadpoor, From flat sheets to curved geometries: Origami and kirigami approaches. *Mater. Today*. **21**, 241–264 (2018).

48. Y. Zhang *et al.*, A mechanically driven form of Kirigami as a route to 3D mesostructures in micro/nanomembranes. *Proc. Natl. Acad. Sci. U. S. A.* **112**, 11757–11764 (2015).

49. X. Liu *et al.*, Metamaterials on parylene thin film substrates: Design, fabrication, and characterization at terahertz frequency. *Appl. Phys. Lett.* **96**, 1–4 (2010).

50. K. Mislow, *Molecular Chirality, in Topics in Stereochemistry* (1999), vol. 22.

51. J. K. Gansel *et al.*, Gold Helix Photonic Metamaterial as Broadband Circular Polarizer. *Science (80-.).* **325**, 1513–1515 (2009).

52. Z. Wang *et al.*, Origami-Based Reconfigurable Metamaterials for Tunable Chirality. *Adv. Mater.* **29**, 1–7 (2017).

53. L. Jing *et al.*, Kirigami metamaterials for reconfigurable toroidal circular dichroism. *NPG Asia Mater.* **10**, 888–898 (2018).

54. T. C. Shyu *et al.*, A kirigami approach to engineering elasticity in nanocomposites through patterned defects. *Nat. Mater.* **14**, 785–789 (2015).

55. Q. Wu, M. Litz, X. C. Zhang, Broadband detection capability of ZnTe electro-optic field detectors. *Appl. Phys. Lett.* (1995), doi:10.1063/1.116356.

56. E. Collett, "Stokes Polarization Parameters." *SPIE Press* (2005), pp. 12–14.

57. E. Collett, "Jones Calculus" in Field Guide to Polarization. *SPIE Press* (2005), pp. 57–61.

58. G. E. Tranter, "Circular Dichroism Spectrometers" in Encyclopeida of Spectroscopy and Spectrometry. *Acad. Press* (2010), pp. 325–336.

59. J. Neu, D. J. Aschaffenburg, M. R. C. Williams, C. A. Schmuttenmaer, Optimization of terahertz metamaterials for near-field sensing of Chiral substances. *IEEE Trans. Terahertz*

Sci. Technol. **7**, 755–764 (2017).

60. S. Mohan, thesis (1999).

61. I. Bahl, *Lumped Elements for RF and Microwave Circuits* (2013), vol. 53.

62. V. Sharma, M. Crne, J. O. Park, M. Srinivasarao, Structural origin of circularly polarized iridescence in jeweled beetles. *Science (80-.).* **325**, 449–451 (2009).

63. G. Agez, C. Bayon, M. Mitov, Multiwavelength micromirrors in the cuticle of scarab beetle Chrysina gloriosa. *Acta Biomater.* (2017), doi:10.1016/j.actbio.2016.11.033.

64. I. Pupeza, R. Wilk, M. Koch, Highly accurate optical material parameter determination with THz time-domain spectroscopy. *Opt. Express* (2007), doi:10.1364/oe.15.004335.

65. V. Sharma, M. Crne, J. O. Park, M. Srinivasarao, Bouligand structures underlie circularly polarized iridescence of scarab beetles: A closer view. *Mater. Today Proc.* **1**, 161–171 (2014).

66. J. C. Weaver *et al.*, The stomatopod dactyl club: A formidable damage-tolerant biological hammer. *Science (80-.).* (2012), doi:10.1126/science.1218764.

67. H. Zhu *et al.*, Observation of chiral phonons. *Science (80-.).* **359**, 579–582 (2018).

68. X. Chen *et al.*, Entanglement of single-photons and chiral phonons in atomically thin WSe 2. *Nat. Phys.* **15**, 221–227 (2019).

69. L. Zhang, Q. Niu, Chiral Phonons at High-Symmetry Points in Monolayer Hexagonal Lattices. *Phys. Rev. Lett.* **115**, 1–5 (2015).

70. X. Yuan *et al.*, The discovery of dynamic chiral anomaly in a Weyl semimetal NbAs. *Nat. Commun.* **11**, 1–7 (2020).

71. J. Yeom *et al.*, Chiromagnetic nanoparticles and gels. *Science (80-.).* **359**, 309–314 (2018).

72. V. K. Valev, J. J. Baumberg, C. Sibilia, T. Verbiest, Chirality and chiroptical effects in plasmonic nanostructures: Fundamentals, recent progress, and outlook. *Adv. Mater.* **25**, 2517–2534 (2013).

73. D. C. Hooper *et al.*, Strong Rotational Anisotropies Affect Nonlinear Chiral Metamaterials. *Adv. Mater.* **29** (2017), doi:10.1002/adma.201605110.

74. S. J. Oh *et al.*, Nanoparticle-enabled terahertz imaging for cancer diagnosis. *Opt. Express*. **17**, 3469 (2009).

75. W. Ma *et al.*, Chiral Inorganic Nanostructures. *Chem. Rev.* **117**, 8041–8093 (2017).

76. Y. C. Shen, Terahertz pulsed spectroscopy and imaging for pharmaceutical applications: A review. *Int. J. Pharm.* **417**, 48–60 (2011).

77. J. A. Zeitler *et al.*, Terahertz pulsed spectroscopy and imaging in the pharmaceutical setting - a review. *J. Pharm. Pharmacol.* **59**, 209–223 (2007).

78. T. A. Keiderling, Protein and peptide secondary structure and conformational determination with vibrational circular dichroism. *Curr. Opin. Chem. Biol.* **6**, 682–688 (2002).

79. S. Woutersen *et al.*, Peptide conformational heterogeneity revealed from nonlinear vibrational spectroscopy and molecular-dynamics simulations. *J. Chem. Phys.* **117**, 6833–6840 (2002).

80. Y. Gao *et al.*, Chiral terahertz wave emission from the Weyl semimetal TaAs. *Nat. Commun.* **11** (2020), doi:10.1038/s41467-020-14463-1.

81. T. M. Korter *et al.*, Terahertz spectroscopy of solid serine and cysteine. *Chem. Phys. Lett.* **418**, 65–70 (2006).

82. P. U. Jepsen, S. J. Clark, Precise ab-initio prediction of terahertz vibrational modes in

crystalline systems. *Chem. Phys. Lett.* **442**, 275–280 (2007).

83. M. R. C. Williams, D. J. Aschaffenburg, B. K. Ofori-Okai, C. A. Schmuttenmaer, Intermolecular vibrations in hydrophobic amino acid crystals: Experiments and calculations. *J. Phys. Chem. B.* **117**, 10444–10461 (2013).

84. A. G. Markelz, A. Roitberg, E. J. Heilweil, Pulsed terahertz spectroscopy of DNA, bovine serum albumin and collagen between 0.1 and 2.0 THz. *Chem. Phys. Lett.* **320**, 42–48 (2000).

85. A. Markelz, S. Whitmire, J. Hillebrecht, R. Birge, THz time domain spectroscopy of biomolecular conformational modes. *Phys. Med. Biol.* **47**, 3797–3805 (2002).

86. M. González-Jiménez *et al.*, Observation of coherent delocalized phonon-like modes in DNA under physiological conditions. *Nat. Commun.* **7** (2016), doi:10.1038/ncomms11799.

87. R. Rungsawang, Y. Ueno, I. Tomita, K. Ajito, Angle-dependent terahertz time-domain spectroscopy of amino acid single crystals. *J. Phys. Chem. B.* **110**, 21259–21263 (2006).

88. R. Singh, D. K. George, J. B. Benedict, T. M. Korter, A. G. Markelz, Improved mode assignment for molecular crystals through anisotropic terahertz spectroscopy. *J. Phys. Chem. A.* **116**, 10359–10364 (2012).

89. S. Grimme, C. Bannwarth, P. Shushkov, A Robust and Accurate Tight-Binding Quantum Chemical Method for Structures, Vibrational Frequencies, and Noncovalent Interactions of Large Molecular Systems Parametrized for All spd-Block Elements (Z = 1-86). *J. Chem. Theory Comput.* **13**, 1989–2009 (2017).

90. F. Garet, M. Hofman, J. Meilhan, F. Simoens, J. L. Coutaz, Evidence of Mie scattering at terahertz frequencies in powder materials. *Appl. Phys. Lett.* **105** (2014),

doi:10.1063/1.4890732.

91. S. S. Dhillon *et al.*, The 2017 terahertz science and technology roadmap. *J. Phys. D. Appl. Phys.* **50** (2017), p. 043001.

92. F. H. Allen, The Cambridge Structural Database: A quarter of a million crystal structures and rising. *Acta Crystallogr. Sect. B Struct. Sci.* **58**, 380–388 (2002).

93. C. F. Macrae *et al.*, Mercury: Visualization and analysis of crystal structures. *J. Appl. Crystallogr.* **39**, 453–457 (2006).

94. R. T. Conley, IR—Theory and practice of infrared spectroscopy (Szymanski, Herman A.; Alpert, Nelson L.). *J. Chem. Educ.* **42**, A316 (1965).

95. C. Provenzano, P. Pagliusi, A. Mazzulla, G. Cipparrone, Method for artifact-free circular dichroism measurements based on polarization grating. *Opt. Lett.* **35**, 1822 (2010).

96. K. Claborn, E. Puklin-Faucher, M. Kurimoto, W. Kaminsky, B. Kahr, Circular Dichroism Imaging Microscopy: Application to Enantiomorphous Twinning in Biaxial Crystals of 1,8-Dihydroxyanthraquinone. *J. Am. Chem. Soc.* **125**, 14825–14831 (2003).

97. X. Liu *et al.*, Metamaterials on parylene thin film substrates: Design, fabrication, and characterization at terahertz frequency. *Appl. Phys. Lett.* **96**, 1–4 (2010).

98. O. P. Cherkasova, M. M. Nazarov, M. Konnikova, A. P. Shkurinov, THz Spectroscopy of Bound Water in Glucose: Direct Measurements from Crystalline to Dissolved State. *J. Infrared, Millimeter, Terahertz Waves*. **41**, 1057–1068 (2020).

99. A. Bandyopadhyay *et al.*, Effects of scattering on THz spectra of granular solids. *Int. J. Infrared Millimeter Waves*. **28**, 969–978 (2007).

100. J. Y. Kim *et al.*, Assembly of Gold Nanoparticles into Chiral Superstructures Driven by Circularly Polarized Light. *J. Am. Chem. Soc.* **141**, 11739–11744 (2019).

101. W. Jiang *et al.*, Emergence of complexity in hierarchically organized chiral particles. *Science (80-.).* **368**, 642–648 (2020).

102. E. Bertie, J. E. and Whalley, Optical Spectra of Orientationally Disordered Crystals. II. Infrared Spectrum of Ice Ih and Ice Ic from 360 to 50 cm−1. **1271** (1967).

103. J. E. Bertie, H. J. Labbé, E. Whalley, Far-infrared spectra of Ice II, V, and IX. *J. Chem. Phys.* **49**, 775–780 (1968).

104. B. W. Matthews, Racemic crystallography - Easy crystals and easy structures: What's not to like? *Protein Sci.* **18**, 1135–1138 (2009).

105. M. Yagasaki, S. I. Hashimoto, Synthesis and application of dipeptides; Current status and perspectives. *Appl. Microbiol. Biotechnol.* **81**, 13–22 (2008).

106. A. D. Burnett *et al.*, Effect of molecular size and particle shape on the terahertz absorption of a homologous series of tetraalkylammonium salts. *Anal. Chem.* **85**, 7926–7934 (2013).

107. S. W. Wukovitz, T. Yeates, Space-Groups Over Others. **2**, 1062–1067 (1995).

108. F. Zhang *et al.*, Application of THz Vibrational Spectroscopy to Molecular Characterization and the Theoretical Fundamentals: An Illustration Using Saccharide Molecules. *Chem. - An Asian J.* **12**, 324–331 (2017).

109. T. Giorgino, Computing and visualizing dynamic time warping alignments in R: The dtw package. *J. Stat. Softw.* **31**, 1–24 (2009).

110. P. Senin, Dynamic Time Warping Algorithm Review. *Science (80-.).* **2007**, 1–23 (2008).

111. T. V. Meert, W., Craenedonck, *Time seires distances: Dynamic time warping (DTW)* (2018).

112. https://towardsdatascience.com/violin-plots-explained-fb1d115e023d.

113. X. Yin, M. Schäferling, B. Metzger, H. Giessen, Interpreting chiral nanophotonic spectra:

The plasmonic Born-Kuhn model. *Nano Lett.* **13**, 6238–6243 (2013).

114. M. S. Davis, W. Zhu, J. K. Lee, H. J. Lezec, A. Agrawal, Microscopic origin of the chiroptical response of optical media. *Sci. Adv.* **5** (2019), doi:10.1126/sciadv.aav8262.

115. K. Levenberg, A method for the solution of certain non-linear problems in least squares. *Q. Appl. Math.* **2**, 164–168 (1944).

116. A. Mathematics, An Algorithm for Least-Squares Estimation of Nonlinear Parameters Author (s): Donald W . Marquardt Source : Journal of the Society for Industrial and Applied Mathematics , Vol . 11 , No . 2 Published by : Society for Industrial and Applied Mathematics S. **11**, 431–441 (2019).

117. J. Sala, E. Gurdia, M. Masia, The polarizable point dipoles method with electrostatic damping: Implementation on a model system. *J. Chem. Phys.* **133** (2010), doi:10.1063/1.3511713.

118. L. H. R. Dos Santos, A. Krawczuk, P. Macchi, Distributed atomic polarizabilities of amino acids and their hydrogen-bonded aggregates. *J. Phys. Chem. A.* **119**, 3285–3298 (2015).

119. T. D. Kühne *et al.*, CP2K: An electronic structure and molecular dynamics software package -Quickstep: Efficient and accurate electronic structure calculations. *J. Chem. Phys.* **152** (2020), doi:10.1063/5.0007045.

120. M. Brehm, M. Thomas, S. Gehrke, B. Kirchner, TRAVIS—A free analyzer for trajectories from molecular simulation. *J. Chem. Phys.* **152** (2020), doi:10.1063/5.0005078.

121. J. D. Rimer *et al.*, Crystal Growth Inhibitors for the Stones Through Molecular Design. *Science (80-.).* **330**, 337–341 (2010).

122. J. Neu, C. A. Schmuttenmaer, Terahertz Spectroscopy and Density Functional Theory

Investigation of the Dipeptide L-Carnosine. *J. Infrared, Millimeter, Terahertz Waves*. **41**, 1366–1377 (2020).

123. A. J. Fitzgerald *et al.*, An introduction to medical imaging with coherent terahertz frequency radiation. *Phys. Med. Biol.* **47** (2002), doi:10.1088/0031-9155/47/7/201.

124. M. Kawase *et al.*, Application of Terahertz absorption spectroscopy to evaluation of aging variation of medicine. *Anal. Sci.* **27**, 209–212 (2011).

125. R. Xiong *et al.*, Biopolymeric photonic structures: Design, fabrication, and emerging applications. *Chem. Soc. Rev.* **49**, 983–1031 (2020).